CNWRA 91-01Q

REPORT ON RESEARCH ACTIVITIES FOR THE QUARTER JANUARY 1 THROUGH MARCH 31, 1991

Prepared for

Nuclear Regulatory Commission
Contract NRC-02-88-005

Prepared by

Center for Nuclear Waste Regulatory Analyses
San Antonio, Texas

May 1991

REPORT ON RESEARCH ACTIVITIES FOR THE QUARTER JANUARY 1 THROUGH MARCH 31, 1991

Prepared for

Nuclear Regulatory Commission
Contract NRC-02-88-005

Edited by

Wesley C. Patrick

Center for Nuclear Waste Regulatory Analyses
San Antonio, Texas

May 1991

TABLE OF CONTENTS

TABLE OF CONTENTS (Cont'd)

TABLE OF CONTENTS (Cont'd)

TABLE OF CONTENTS (Cont'd)

LIST OF FIGURES

LIST OF FIGURES (Cont'd)

LIST OF FIGURES (Cont'd)

LIST OF TABLES

ACKNOWLEDGMENTS

This report was prepared to document work performed by the Center for Nuclear Waste Regulatory Analyses (CNWRA) for the U. S. Nuclear Regulatory Commission under Contract No. NRC-02-88-005. The research activities reported here were performed on behalf of the NRC Office of Nuclear Regulatory Research, Division of Engineering. The report is an independent product of the CNWRA and does not necessarily reflect the views or regulatory position of the NRC.

Each chapter of this report acknowledges those investigators who, although not specifically involved in writing the report, made significant contributions to the research projects. In addition, the authors gratefully acknowledge the technical support and technical reviews conducted by other members of the CNWRA and Institute staffs. Appreciation is particularly due Bonnie Garcia, Cathy Garcia, and Mary Ann Gruhlke, who prepared input to the individual chapters of the report, and to Pamela Smith, who prepared the final text of this document. We also acknowledge the able assistance of Curtis Gray, who provided graphical assistance, and Dr. Shirley Heller, who provided a full range of expert editorial services in the preparation of the final document.

1. EXECUTIVE SUMMARY

1.1. INTRODUCTION

This is one in a series of research quarterly reports that document and make available to the technical community work undertaken by the Center for Nuclear Waste Regulatory Analyses (CNWRA) as part of its contract with the U.S. Nuclear Regulatory Commission (NRC). Reports are prepared each calendar quarter and published as CNWRA documents. The fourth such report each year constitutes the annual progress report and is published as a NUREG/CR.

Each of the research projects discussed here is conducted in accordance with approved Research Project Plans, which were developed in response to research needs identified by the NRC and the CNWRA. These Plans are the vehicle for establishing the objectives, technical approach, justification, and funding for each of the studies. They also describe the interrelationships among the various projects which provide a sound basis for integrating research results. Because the Plans address primarily planning and management matters, they are not discussed in this project (with the exception of stating project objectives).

A project on Sorption Modeling for High-Level Waste (HLW) Performance Assessment (PA) was initiated since the last report, bringing the total to eight individual research project. Because several of the projects have only recently been initiated, they have relatively little work to report at this time. In such cases, this report provides basic information on the objectives of the new projects as well as early activities such as literature assessments. Other projects begun earlier have significant technical progress in laboratory, calculational, or field studies, or a combination of such investigations, to report.

This document provides, first, an Executive Summary that covers in capsule form the progress of each research project over the past quarter. The Executive Summary is followed by Chapters 2 through 9 representing each of the eight currently active research projects, respectively. Project objectives and a report of research activities and results (as appropriate) to date are given in each chapter.

1.2. UNSATURATED MASS TRANSPORT (GEOCHEMISTRY)

A major geologic feature potentially affecting the suitability of Yucca Mountain, Nevada, as a repository site for high-level nuclear wastes is the presence of thick, laterally extensive zones of zeolitic tuff. Because of their sorptive properties, zeolites could provide important geologic barriers to migration of radionuclides from the repository to the accessible environment. To support the NRC's HLW program, the Center is conducting experimental studies on the thermodynamic and ion exchange properties of zeolites under Task 3 of the Geochemistry Research Project. The objective of these studies is to generate data needed to evaluate the effectiveness of zeolitic tuffs as barriers to radionuclide migration.

Experiments have been proposed previously to evaluate phase equilibria between the zeolite minerals clinoptilolite and analcime and the aqueous solutions. The objective of the proposed experiments is to investigate techniques to resolve the problem of uncertainties in the standard-state thermodynamic properties of clinoptilolite. Because of the absence of dissolution/precipitation rate data for the zeolites, accurate prediction of the required duration to achieve equilibrium in the experiments is precluded. The first phase of the proposed experiments, therefore, involves determination of the rate of dissolution of the zeolite mineral analcime. This phase was initiated during this quarter. Details of the experiments and initial results are reported in Chapter 2.

In the modeling task of the Geochemistry Research Project, principles of thermodynamics, kinetics, and mass balance are applied to the interpretation of natural and experimental systems pertinent to Yucca Mountain. Computer codes of equilibrium aqueous speciation and reaction-path simulations of water-rock interactions constitute a primary research tool. Confidence in the validity of codes, data, and conceptual models can be generated by successful applications to a variety of systems. The Koongarra ore deposit at the Alligator Rivers natural analog site has been selected for selected geochemical modeling applications. Recently acquired analytical groundwater data from this site, background information on mineral paragenesis, and geochemical processes in the silicate zone at Koongarra to the Yucca Mountain repository environment make this a relevant study. Thermodynamic and reaction-path computations for the Koongarra site reveal that uncertainties in analytical measurements of the groundwater oxidation state, as well as in thermodynamic data for uranium silicate minerals have important effects on the validity of the model results. Also, open-system geochemical models appear to be required to adequately represent the genesis of the silicate zone mineralogy.

1.3. THERMOHYDROLOGY

Technical issues and uncertainties for the Yucca Mountain HLW repository site indicate a need for research on thermohydrological phenomena, i.e., phenomena associated with heat and fluid flow, to provide information pertinent to performance assessment and design criteria. The class of thermohydrological phenomena examined in this project includes phenomena driven by heat emanating from HLW emplaced in a geologic repository. Information derived principally from research is used to establish a knowledge base of thermohydrologic phenomena that will be utilized to assess models of processes used in performance assessments.

The Thermohydrology Research Project has progressed in three areas during the past quarter: experimentally, numerically and analytically. The final separate-effects experiment, Test 6, was completed during this quarter. Test 6 provided additional insight into significant thermohydrological phenomena. Of particular interest were the effect of the simulated fracture and the nature of the drying front near the heated boundary. As in Test 5, the fracture acted as a barrier to flow of liquid water under partially saturated conditions. The drying front means the heated boundary progressed more rapidly at the bottom boundary of the test chamber than at the top boundary.

Modifications and improvements in Test 6, as compared to Test 5, resulted in more substantive data but did not provide sufficient quantitative results for in-depth analysis. In particular, additional improvements to the gamma-ray densitometer methodology that were formulated during the execution of Test 6, but not implemented during that test in order to maintain continuity of measurement during the experiment, will be incorporated into future experiments.

The twenty-seven dimensionless pi terms in the set of dimensionless governing equations have been evaluated to assess their importance relative to the laboratory-scale, separate-effects experiment. As part of the initial assessment, the pi terms were evaluated to identify those that, merit further evaluation, at least during this preliminary assessment. The parameters comprising the pi terms have been assigned values representative of the physical characteristics of the laboratory-scale, separate-effects experiments. For the purposes of this assessment, the effect of the fracture has not been incorporated into the evaluation.

The numerical magnitudes of the pi terms were calculated using the assigned parameter values. Generally, a very large or very small pi term indicates that one or the other of the two effects in the ratio that forms the term is unimportant. Pi terms were selected for further examination based on physical reasoning and the observed results of the preliminary separate-effects tests, in addition to the numerical magnitude of the terms.

In each simulation, the input parameters, except for the perturbed variable, were assigned values from a nominal case. This case was taken to be representative of one of the laboratory separate-effects experiments. The influence of each pi term was investigated separately by increasing and decreasing each pi term relative to a selected nominal value, while holding all the other important pi terms constant. Five pi terms were selected for further analysis based upon this initial assessment. The effects of variations in the input values of the five pi terms were evaluated using the TOUGH code.

The results of the dimensional analysis presented in this report have been submitted to the ASME Symposium on Two-Phase Flow through Porous Media. The symposium is scheduled for December, 1991.

1.4. SEISMIC ROCK MECHANICS

A literature review of the state-of-the-art reveals that the seismic effects calculations performed to date on underground structures have not been supported by an adequate level of experimental and field investigations. The experimental support for most of the programs has focused on soils rather than on structurally complex rock formations. Computer programs are currently available to model dynamic events of underground structures in rock formations. However, these programs have not been validated with well-planned and rigorous experimental and field protocols. This Seismic Rock Mechanics Research Project is aimed at developing a better understanding of the key parameters affecting the repository under seismic loadings and

consequently validation of computer programs for use in seismic assessment of underground structures in tuff media.

Activities performed for the Seismic Rock Mechanics Project during this reporting period included data analysis for three pseudostatic rock-joint shear tests, testing of cylindrical specimens for tuff material characterization, and instrumented field studies at the Lucky Friday Mine.

Experimental results of pseudostatic rock-joint shear tests show that the normal deformability can be modeled reasonably well using both the Barton-Bandis and Continuously-Yielding joint closure models.

Preparation of direct shear-test specimens and cylindrical specimens for material characterization tests was completed. A total of 45 direct shear specimens was prepared. Tests were conducted on 113 uniaxial compression specimens, 44 triaxial compression specimens, and 120 Brazilian disk tension specimens. The average uniaxial compressive strength was found to be 164 MPa (23,764 psi). The mean triaxial compressive strength was 199 MPa (28,923 psi) for a confining pressure of 3.5 MPa (500 psi), 244 MPa (35,400 psi) for a confining pressure of 6.9 MPa (1,000 psi), and 270 MPa (39,100 psi) for a confining pressure of 10.3 MPa (1,500 psi). Average uniaxial tensile strength was determined to be 10.6 MPa (1,533 psi). Average values for Young's modulus and Poison's ratio of the Apache Leap tuff were 3.86×10^4 MPa (5.6×10^6 psi) and 0.2, respectively.

Installation of piezometers in the 20 degree inclined borehole at the 5700-level of the Lucky Friday Mine for measurement of water-pressure change near identified fault and ore veins was completed. Data collection is underway. Initial reading indicates that the water head at a measuring point in the borehole is about 264 m (866 feet). This measuring point is located at about 278 m (912 feet) from the collar of the borehole and 95 m (312 feet) below. The readings from the backup transfer tubing gauges give similar results as those from piezometers.

1.5. INTEGRATED WASTE PACKAGE EXPERIMENTS

The NRC regulation 10 CFR 60.113 requires the waste package to provide substantially complete containment of radionuclides for a period of 300 to 1000 years. This requirement necessitates the demonstration, through a combination of experimental data and modeling, the performance of a waste package system over long periods of time. NRC, in its role of licensor, must develop an understanding of the important parameters that affect long-term performance of waste package and the applicability and limitations of the test techniques used to obtain these parameters. The goal of the Integrated Waste Package Experiments (IWPE) Program is to enable the NRC and the Center to develop the technical capability and, where necessary, independent experimental data to provide appropriate, timely prelicensing guidance to DOE and to review DOE waste package design licensing submittals to the NRC. The IWPE program consists of both confirmatory research, which is used to evaluate the materials degradation data supplied by DOE and other NRC-sponsored research programs, and anticipatory (exploratory) research, which

investigates waste package performance parameters not examined hitherto. Following general approval of Revision 2 of the IWPE Project Plan, Revision 3 was submitted on December 20, 1990, to include in the plan changes required by NRC staff. This report follows the task classifications adopted in Revision 2 and 3 of the IWPE Project Plan, which are as follows: Task 1. Corrosion, Task 2. Stress Corrosion Cracking, Task 3. Materials Stability, Task 4. Microbiologically Influenced Corrosion, Task 5. Other Degradation Modes, and Task 6. General Reporting. The present report focuses on the accomplishments in Task 1, under the subtask of localized corrosion.

The critical review of the literature on localized corrosion of candidate alloys is being continued with emphasis on experimental techniques and the influence of environmental factors. The crevice corrosion repassivation technique was examined in detail as one of the most promising techniques from the point of view of long-term prediction.

During this reporting period, experimental work was concentrated on the effects of some environmental variables on the localized corrosion of alloy 825. The effects of bicarbonate, pH, and sulfate were investigated using the cyclic potentiodynamic polarization technique. The bicarbonate concentration was varied from 85 to 2000 ppm in solutions containing 1000 ppm chloride, 20 ppm sulfate, 10 ppm nitrate, and 2 ppm fluoride, in which the pH was about 8.2 at the start of the test and about 9.4 at the end of the test. It was found that bicarbonate does not affect the corrosion potential and the pitting potential, but decreases slightly the repassivation potential. As a consequence, the localized corrosion index (LCI) increases slightly, but the statistical significance of the increase still needs to be established. Further tests are in progress.

The decrease in pH from 8.1 to approximately 5.0 by bubbling CO_2 in a solution containing 85 ppm bicarbonate, 1000 ppm chloride, 20 ppm sulfate, 10 ppm nitrate, and 2 ppm fluoride has a significant impact in the localized corrosion behavior of alloy 825. LCI increases significantly whereas no pH effect was observed in solutions with a very low chloride content (few ppm). The main effect of pH is exercised on the repassivation potential while the pitting potential is slightly lowered by the pH decrease. It was also found that sulfate at high concentrations (20,000 ppm) has an inhibiting effect on the localized corrosion of alloy 825 in solutions containing 1000 ppm chloride. It is apparent that a molar concentration ratio SO_4^{2-}/Cl^- higher than 1.0 is required for inhibition.

Preliminary studies on the localized corrosion behavior of alloy C-22, the CNWRA's reference alloy, were conducted in solutions containing 10,000 ppm chloride. It was found that this alloy exhibited a superior resistance to localized corrosion than alloy 825. As was the case for alloy 825 at low chloride concentrations, very poor correlation was found between electrochemical parameters and visual observations of localized corrosion.

1.6. STOCHASTIC ANALYSIS OF FLOW AND TRANSPORT

A quantitative characterization of large-scale flow and radionuclide transport through the heterogeneous unsaturated fractured rock of Yucca Mountain will be necessary to evaluate compliance with the siting criteria and performance objectives associated with the proposed Yucca Mountain HLW repository (10 CFR 60.122 and 60.113). Realistic modeling of the complex, heterogeneous flow and transport processes at Yucca Mountain will require incorporating the effects of relatively small-scale as well as large-scale space-time variability in modeling unsaturated flow and radionuclide transport. Examples of geologic features that can have significant effects on flow and transport are faults and fractures, finer fissures, and stratification leading to anisotropic behavior.

The specific objectives of the project are to: perform a review of the literature and assess available models and data relevant to the subject site, select a global approach to model large-scale flow and transport in unsaturated fractured rock, develop submodels for incorporation into the global model, perform large-scale simulations, and participate in the validation of flow/transport models for the Yucca Mountain repository.

Work accomplished during this quarter is described in Section 6. The main accomplishment is the finalization of literature review, initial data assessment, model selection, and first stages of model development, to be published as a NUREG/CR under the title: "Approaches to Large-Scale Unsaturated Flow in Heterogeneous, Stratified, and Fractured Geologic Media." This report analyzes the requisites of field-scale flow models based on a broad review of field data, including the site-specific hydrogeologic setting of Yucca Mountain, observations of vadose zone contamination at other sites, and controlled field experiments. Local constitutive models and locally unsaturated hydraulic properties are reviewed and interpreted as well, with particular emphasis on their relations to structural characteristics of the medium. The report further reviews large-scale spatial variability of hydrogeologic properties from aquifer data, unsaturated soil data, and fracture network data collected in the literature. Various modeling strategies for mountain-scale flow simulations are assessed, including both direct high-resolution simulations and indirect coarse-scale simulations based on hydrodynamic auxiliary models (for instance dual porosity models). The roles of anisotropy, fracturing, and broad-band spatial variability, are emphasized.

1.7. GEOCHEMICAL ANALOGS

The Geochemical Analog Project is designed to provide knowledge of the state of the art in natural analog studies applied to contaminant transport and to conduct investigations of a specific site or sites. The project began in February 1990; Task 1 of the project, "Literature Review," has been completed; and Task 2, "Identification of Site and Development of Workplan," is presently underway. Objectives of Task 2 include gathering preliminary field data on candidate analog site, selecting a site or sites for investigation, defining research problems appropriate for the site or sites which are relevant to radionuclide transport in the Yucca Mountain environment, and developing a workplan to accomplish those investigations.

Work to date in Task 2 has included field research at the Peña Blanca, Mexico, uranium district (one of three potential analog sites identified during Task 1). Objectives were to assess similarities between Peña Blanca and Yucca Mountain environments and to evaluate potential geochemical analog research sites at Peña Blanca.

The Peña Blanca district appears to provide an excellent analog to geochemical processes which may occur in the proposed Yucca Mountain repository system. Analogous aspects of the district are the silicic, tuffaceous rock types; semi-arid climate; occurrence of the deposits in hydrologically unsaturated rocks; and presence of uranium mineralization. Specifically, the Nopal I deposit has been identified as a potential site for further work because the mineralization is accessible and well-exposed; the deposit has a relatively small scale and simple geometry; both primary uraninite and oxidized uranyl silicate alteration minerals occur in the ore, and information is available from previous research at the deposit. Processes governing the oxidation of Peña Blanca uraninite, the resulting dispersion of uranium from the sites of original mineralization, and the formation of secondary uranyl silicates are analogous to processes that may affect spent nuclear fuel and elemental migration at a high-level waste repository at Yucca Mountain.

1.8. PERFORMANCE ASSESSMENT RESEARCH

Progress this quarter has been primarily in Task 7 of the Performance Assessment (PA) Research Project, which has as its objective the evaluation and development of methodologies for the validation of computer models of flow and transport processes. Inasmuch as computer models will be used to assess the performance of the high-level nuclear waste repository, the development of model validation methods must be an integral part of overall performance assessment research. INTRAVAL is an international project which addresses the development of procedures to test the validity of mathematical models used to predict the fate and transport of radioactive substances in the geosphere. As such, INTRAVAL is an ideal setting in which to obtain experimental data to test models and an excellent forum in which to discuss the modeling results.

The Las Cruces Trench is an extremely well instrumented, unsaturated zone flow and solute transport field experiment which is suited for the purposes of Task 7. At present, only the preliminary phases of model structure development using the PORFLO-3, Version 1.2 (single phase version) to model both flow and transport are discussed. Subsequent reports will detail progress in calibrating the model and developing PA based measures of model validity.

1.9. SORPTION MODELING FOR HIGH-LEVEL WASTE PERFORMANCE ASSESSMENT

An evaluation of the effectiveness of geologic systems as barriers to radionuclide migration requires an understanding of the chemical and physical processes by which aqueous species are sorbed on geologic materials. These processes, which may include adsorption, ion exchange, and precipitation, are commonly represented collectively by empirical parameters,

such as sorption coefficient (K_d) or retardation factor (R_f), in transport calculations supporting performance assessments of geologic repositories. However, there is active debate on the usefulness of these empirical parameters in quantitatively describing aqueous-solute/rock interactions for PA calculations of radionuclide transport. Transport models that use these parameters, particularly those that assume constant K_d's or R_f's, do not explicitly take into account many potentially important geochemical phenomena that occur during transport in natural systems. These phenomena include aqueous complexation, precipitation/dissolution reactions, competitive sorption, changes in groundwater chemistry, and variability in substrate composition as well as changes in fluid saturations, temperature, and pressure. Questions have been raised regarding the adequacy of transport calculations using K_d or R_f in PA.

To support NRC's HLW program, the CNWRA is conducting research activities under the Sorption Modeling for HLW PA Research Project. The objectives of this project are: (1) to obtain a mechanistic understanding of the important radionuclide sorption processes and the physical and chemical parameters that affect sorption behavior in the Yucca Mt., Nevada, environment; (2) to investigate the applicability of coupled-hydrogeochemical models which use simple representations of sorption phenomena to Yucca Mt. performance assessment; and (3) to develop practical but scientifically defensible approaches to modeling sorption at Yucca Mt., and the requisite databases to support such models. The goal of the research project is to develop sufficient understanding of radionuclide transport issues so that timely prelicensing guidance can be provided to the DOE and a sound basis is available for evaluating the DOE license application.

The research project has been divided into three tasks for the purpose of achieving these objectives. Only one task is active at this time: Task 1 - Literature Review and Development of Approach. The literature review conducted during this quarter focused on two major subjects: (1) experimental and modeling studies on sorption of uranium on geologic media and (2) coupled reaction-transport models. Results of the literature review are discussed in Chapter 9.

Uranium was chosen as the initial focus of literature review on sorption studies because it is a good analog for understanding the sorption behavior of the other actinides and because it has an extensive and well-evaluated thermodynamic database for aqueous species. Based on the review of uranium sorption studies, a work plan for conducting experimental studies on uranium sorption on geologic media was developed and submitted to NRC for review and approval. This work plan is briefly discussed in Section 9.3.4.

The literature review of coupled reaction-transport models used a defined set of selection criteria to evaluate available hydrogeochemical or transport codes, with an emphasis on code flexibility, computational efficiency and accuracy, adequacy of the database, 'user-friendliness,' and adaptability for future applications. The CTM, FASTCHEM, TRANQL, CHEMTRN, and CHMTRNS hydrogeochemical models, and the NEFTRAN II and TRACR3D solute transport codes are discussed; and the advantages and limitations of each are considered using the criteria just outlined. The CTM code has been chosen for further investigation based on this

comparison. The code, developed at Pacific Northwest Laboratories (PNL) for the Low-Level Waste Management Division of the NRC, is similar in design to the proprietary FASTCHEM code, and uses an efficient two-step coupling approach with a modified version of the MINTEQA2 database. The code has both pre- and postprocessing capability for flexible input and output. Because the code has been adapted to the IBM PS/2 Model 70 personal computer system, computer costs are minimal.

2. UNSATURATED MASS TRANSPORT (GEOCHEMISTRY)

by Roberto T. Pabalan and William M. Murphy

Investigators: William M. Murphy (CNWRA), Roberto T. Pabalan (CNWRA), James Prikryl (CNWRA), and George F. Birchard (NRC)

2.1. EXPERIMENTAL STUDIES by Roberto T. Pabalan

2.1.1. Technical Objectives

A major geologic feature potentially affecting the suitability of Yucca Mountain, Nevada, as a repository site for high-level nuclear wastes is the presence of thick, laterally extensive zones of zeolitic tuff. Because of their sorptive properties, zeolites could provide important geologic barriers to migration of radionuclides from the repository to the accessible environment. To support the NRC's high-level waste program, the Center for Nuclear Waste Regulatory Analyses (CNWRA) is conducting experimental studies on the thermodynamic and ion exchange properties of zeolites under Task 3 of the Geochemistry Research Project. The objective of these studies is to generate data needed to evaluate the effectiveness of zeolitic tuffs as barriers to radionuclide migration.

Experiments have been proposed previously to evaluate phase equilibria between aqueous solutions and the zeolite minerals clinoptilolite and analcime (see Murphy, 1991). The objective of the proposed experiments is to investigate techniques to resolve the problem of uncertainties in the standard state thermodynamic properties of clinoptilolite. Because dissolution/precipitation rate data are absent for the zeolites, accurate prediction of the required duration to achieve equilibrium in the experiments is precluded. The first phase of the proposed experiments, therefore, involves determination of the rate of dissolution of the zeolite mineral analcime. This phase was initiated during this quarter. Details of the experiments and initial results are reported here.

2.1.2. Experimental Methods

2.1.2.1. Characterization and Preparation of Analcime Material

Analcime samples were obtained from Ward's Natural Science Establishment, Inc. These samples are from Mt. St. Hilaire, Quebec, where the analcime occurs in coarsely crystalline late magnatic stage pegmatites in nepheline syenites. The as-received samples, which consisted of analcime crystals about 1 to 6 cm in diameter and intergrown with accessory K-feldspar, hornblende, and muscovite, were broken into pieces less than 0.5 cm in diameter with a hammer. Essentially pure analcime crystals were separated by hand-picking, crushing and grinding in a mortar and pestle, and sieving into three size ranges using a Ro-Tap sieve shaker and 8-inch-diameter stainless steel sieves. The size ranges were: (1) 200-230 mesh (75-63 microns), (2) 230-325 mesh (63-45 microns), and (3) 325-450 mesh (45-32 microns).

Sieving was repeated several times to minimize retention of analcime grains of a particular size with grains in the larger size range.

X-ray diffraction (XRD) analysis of less than 450 mesh-size powder samples was done using a Siemens D-500 x-ray diffractometer and Siemens Kristalloflex 800 x-ray generator to verify that the mineral sample was analcime. Figure 2-1 shows the XRD pattern of the analcime sample. A comparison of the pattern with the Joint Committee on Powder Diffraction Standards (JCPDS) mineral powder diffraction file (#19-1180) confirms that the sample is analcime. No diffraction peaks for other minerals are observed.

All samples were cleaned ultrasonically several times in ultrapure (> 17 mega-ohm resistivity) water to remove fine surface particles. Published mineral dissolution studies indicate that the presence of such particles leads to an initial accelerated rate of release of mineral components, followed by a constant release rate of elements, which reflects the steady-state dissolution rate of the mineral under conditions far from equilibrium (Holdren and Berner, 1979; Brady and Walther, 1990). Figure 2-2 shows scanning electron (SEM) photomicrographs of analcime powder (230-325 mesh size fraction) before (Fig. 2-2a) and after (Fig. 2-2b) ultrasonic cleaning. The SEM photomicrographs indicate that ultrasonic cleaning removed most of the fine material from the analcime surfaces.

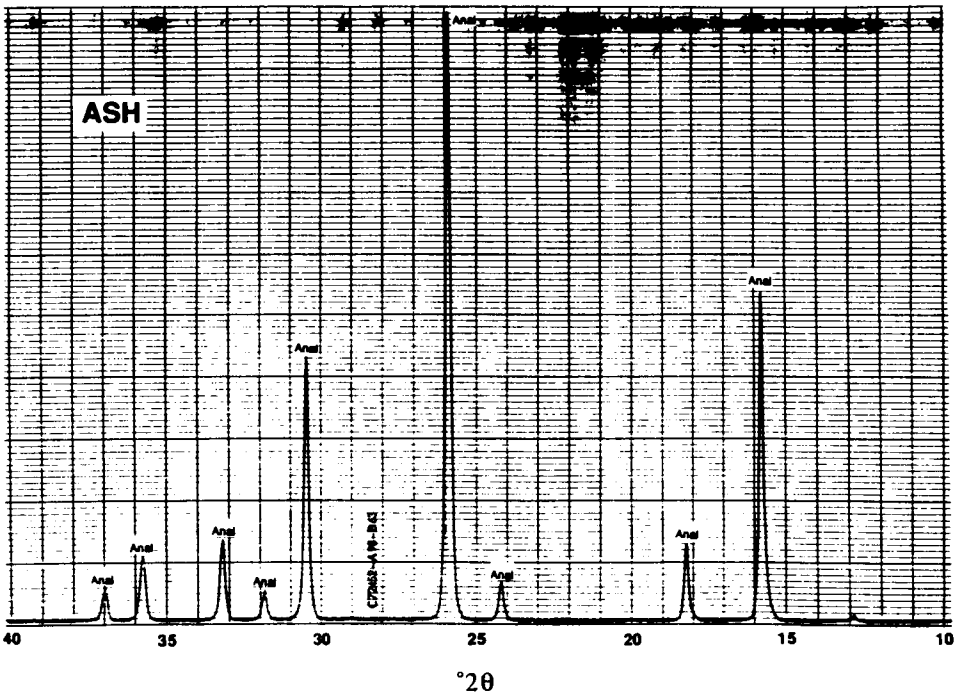

Figure 2-1. X-ray powder diffraction pattern of analcime sample from Mt. St. Hilaire, Quebec (Sample Name ASH)

Figure 2-2. Scanning electron photomicrographs of analcime powder (230-325 mesh size): (a) before and (b) after ultrasonic cleaning

The chemical composition of two analcime samples was determined by inductively coupled plasma emission spectrometry (ICP-ES) subsequent to lithium metaborate fusion and dissolution in an HCl/HNO_3 matrix. Analysis for Fe^{2+} was performed by titration. The water content of analcime was determined by measuring its weight before and after heating at 900°C for two hours. Results of the chemical analyses are given in Table 2-1. The stoichiometric formula of analcime (normalized to 96 oxygens per unit cell) is given by $Na_{16.47}K_{0.015}Mg_{0.052}Fe^{2+}_{0.005}Fe^{3+}_{0.018}Ti_{0.004}Si_{31.62}Al_{16.31}O_{96}\bullet 15.3H_2O$, based on the chemical analysis of Sample 1, and is given by $Na_{15.99}K_{0.038}Mg_{0.053}Fe^{2+}_{0.015}Fe^{3+}_{0.004}Ti_{0.004}Si_{31.88}Al_{16.11}O_{96}\bullet 15.5H_2O$ based on the results for Sample 2. The ideal formula for analcime is $Na_{16}Al_{16}Si_{32}O_{96}\bullet 16H_2O$ (Gottardi and Galli, 1985).

Surface areas for the ultrasonically cleaned 230-325 mesh size analcime powder were calculated from BET nitrogen adsorption measurements (Brunauer et al., 1938) using a Micromeritics Flowsorb 2300 surface area analyzer, and were 1800 ± 100 cm^2 g^{-1}.

Table 2-1. ANALCIME CHEMICAL ANALYSES

Component	Sample 1 (Wt%)	Sample 2 (Wt%)
SiO_2	54.36	54.11
Al_2O_3	23.79	23.20
TiO_2	0.01	0.01
Fe_2O_3	0.04	0.01
FeO	0.01	0.03
MnO	0.00	0.00
MgO	0.06	0.06
CaO	0.00	0.00
Na_2O	14.60	14.00
K_2O	0.02	0.05
P_2O_5	0.00	0.00
H_2O^*	7.89	7.89
TOTAL	100.78	99.36

*Average of 3 analyses (± 0.12)

2.1.2.2. Dissolution Kinetic Experiments

Dissolution kinetic experiments were conducted by reacting analcime powder in the 230-325 mesh size (63-45 microns) range with 0.10 M NaCl - 0.010 M $NaHCO_3$ solutions. These solutions were previously preequilibrated with atmospheric $CO_2(g)$ for several days, until constant pH values were achieved. The pH of the solutions prior to addition of analcime was 8.95 ± 0.10, and was expected to remain close to this value due to buffering by carbonate equilibria. The Na concentration and the pH of the solutions used in the experiments were planned to minimize nonstoichiometric dissolution of analcime, based on calculations conducted using the E3/6 geochemical code (see Murphy, 1991). The solid-mass/solution-volume ratio was varied by reacting 0.10, 0.50, and 1.0 gm of analcime with 400 ml of the aqueous solution in separate 500 ml polypropylene

bottles. The bottles were thermostatted at 25.0±0.1 °C and kept under agitation using a constant temperature water bath (Fisher Versabath 236).

The extent of reaction was followed by taking aqueous samples from each bottle after certain time intervals and analyzing the samples for SiO_2 and Al concentrations. At each sampling step, 20 ml aliquots were withdrawn from each bottle for SiO_2 analysis, and another 20 ml were taken for analysis for Al. These 20 ml aliquots were not replaced with new solutions; hence, corrections will be needed during data interpretation to account for changes in the solid-mass/solution-volume ratios.

All samples were passed through 0.20 micron filters to minimize the potential contribution of colloidal silica or alumina in the chemical analyses. SiO_2 and Al concentrations were determined using a Milton Roy 1201 spectrophotometer using the heteropoly blue and eriochrome cyanine R methods, respectively (Shull and Guthan, 1967; Fanning and Pilson, 1973). The use of glassware in the analysis of SiO_2 was avoided because silica concentrations in the aqueous solutions were low, and analytic results from previous test runs indicated silica contamination from various glassware. Periodically, the Na^+ concentration and the pH of the aqueous solution were analyzed using ion selective and pH electrodes, respectively. Values of Na^+ and pH remained close to initial values (± 0.003M Na^+ and ± 0.03 pH units).

2.1.3. Results

Initial results are given in Tables 2-2 and 2-3 for SiO_2 and Al analyses, respectively. Figure 2-3 is a plot of silica concentrations vs. time for each of the solid-mass/solution-volume ratios used in the experiments. These results indicate that for aqueous solutions reacting with 0.5 and 1.0 g analcime, silica concentration increases with time, and that saturation has not been reached even at 766 hrs. (32 days). The results for the solution reacting with 0.1 g analcime are variable, and are probably due to the low silica concentrations close to the detection limit of the spectrophotometric method used.

Figure 2-3 indicates that there is a short period of accelerated dissolution, which likely represents dissolution from high-energy reaction sites or fine particles (see Schott et al., 1989). Calculations of long-term dissolution rates after termination of the experiments will use data from the more advanced part of the curves after corrections are made for variable surface-area/solution-volume ratios.

Most Al analyses were below detection limit, suggesting potential errors in the analytical technique. Recent tests indicated that the pH between standards and samples must be stringently controlled to obtain accurate results for Al using the eriochrome cyanine R method. Subsequent analyses will use procedures modified to ensure that pH between standards and samples are identical.

Table 2-2. CONCENTRATIONS OF SiO_2 *vs.* TIME IN 0.1 M NaCl - 0.01 M $NaHCO_3$ SOLUTIONS REACTING WITH 0.1, 0.5, AND 1.0 g ANALCIME POWDER (230-325 mesh size). DETECTION LIMIT FOR SiO_2 IS 4.16 X 10^{-7} moles/kg.

Elapsed Time (hours)	Silica concentration (moles/kg SiO_2 X 10^6)		
	0.1 g analcime	0.5 g analcime	1.0 g analcime
0.0	BDL	BDL	BDL
5.9	BDL	BDL	BDL
26.6	BDL	1.42	1.76
71.8	BDL	2.13	3.90
120.3	BDL	2.89	5.45
173.1	BDL	3.84	6.50
213.9	1.90	3.84	7.02
262.6	1.71	4.70	8.63
334.6	1.23	6.12	9.91
766.6	2.66	10.1	16.4

These experiments are continuing, and interpretion of preliminary data are being conducted. Additional samples will be taken during the next quarter, and new experiments will be initiated based on the results of these experiments.

2.2. GEOCHEMICAL MODELING by William M. Murphy

2.2.1. Technical Objectives

The technical objective of the modeling task of the Geochemistry Research Project is to apply principles of thermodynamics, kinetics, and mass balance to the interpretation of natural and experimental systems pertinent to ambient and repository geochemical conditions at Yucca Mountain and to the prediction of the evolution of these systems.

Computer codes for equilibrium aqueous speciation and reaction-path simulations of water-rock interactions constitute a primary geochemical modeling tool. Confidence in the validity of models is generated by successful applications of the computer programs to a variety

Table 2-3. CONCENTRATIONS OF Al *vs.* TIME IN 0.1 M NaCl - 0.01 M $NaHCO_3$ SOLUTIONS REACTING WITH 0.1, 0.5, AND 1.0 g ANALCIME POWDER (230-325 mesh size). DETECTION LIMIT FOR Al IS 20 ppb.

Elapsed Time (hours)	Al concentration (ppb)		
	0.1 g analcime	0.5 g analcime	1.0 g analcime
0.0	BDL	BDL	BDL
5.9	BDL	BDL	BDL
26.6	BDL	BDL	BDL
71.8	BDL	BDL	BDL
120.3	BDL	BDL	71.5
173.1	BDL	BDL	71.0
213.9	BDL	BDL	90.8
262.6	BDL	BDL	68.8
334.6	BDL	BDL	101
766.6	BDL	125	220

of systems. A few large-scale natural geochemical systems which have been studied in detail as analogs of nuclear waste repositories offer the possibility to evaluate geochemical modeling concepts, codes, and data. Among these, the Koongarra Deposit at Alligator Rivers, Australia, is particularly significant because newly acquired analytical water chemistry data are available and because it offers geochemical environments analogous to the Yucca Mountain system. The objective of work reported here is to apply geochemical modeling tools (conceptual models and computer programs and data) to the Koongarra system. The analytical data from Koongarra, the modeling concepts, and the validity of geochemical data constituting parametric calibration of the models will be investigated and evaluated.

2.2.2. Thermodynamic and Reaction-Path Analysis of Groundwater at the Alligator Rivers Natural Analog Site

The Koongarra ore body in the Alligator Rivers uranium district is under investigation as an analog of geologic nuclear waste disposal systems by the international Alligator Rivers Analogue Project, with participation by the U.S. Nuclear Regulatory

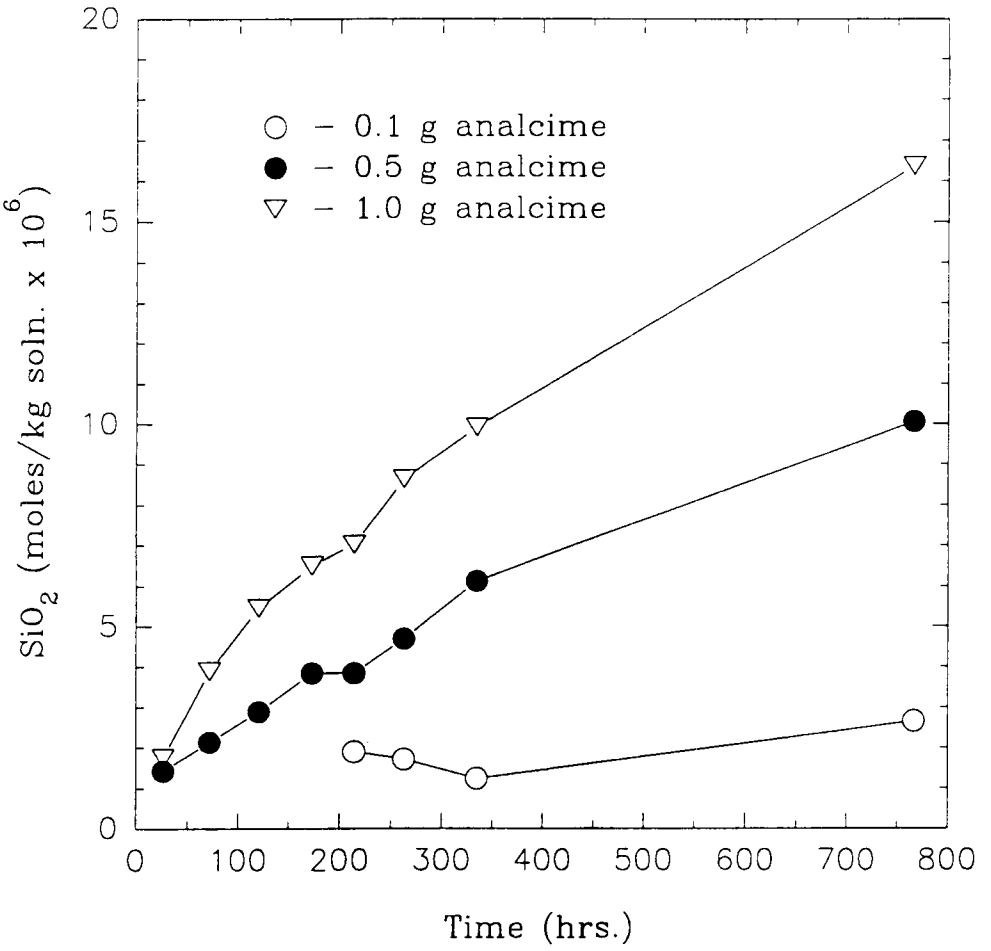

Figure 2-3. Concentration of silica vs. time in 0.1 M NaCl - 0.01 M $NaHCO_3$ solutions reacting with 0.1, 0.5, and 1.0 g of analcime powder (230-325 mesh size)

Commission (e.g., Duerden, 1990). A focus of recent research has been the chemical analysis of groundwater extracted from wells at the site. Based on these data, Sverjenski (1990) has performed thermodynamic and reaction-path analyses of mineral and groundwater chemistry to model the origin of the phosphate zone at Koongarra. In contrast to the phosphate zone, the geochemistry of the silicate zone at Koongarra is likely to be more relevant to processes in a Yucca Mountain repository environment. The geochemical evolution of the Koongarra deposit has been described by Snelling (1980). The secondary alteration history in the silicate zone involved chlorite growth, pitchblende (UO_{2+x}) oxidation and dissolution, uranium migration, and precipitation of oxidized uranium silicates including sklodowskite (magnesium uranyl silicate) and uranophane (calcium uranyl silicate). These processes are of interest in relation to the proposed Yucca Mountain repository, because in that oxidizing, silicic environment, spent fuel

(predominantly UO_2) is expected to oxidize, leading to mass transfer of uranium to uranyl silicate phases.

Two approaches have been adopted here in a thermodynamic and reaction-path analysis of groundwater at the Koongarra site. The first approach is to calculate equilibrium aqueous speciations for selected water samples and the saturation states of these waters with respect to mineral phases. Analysis of the correspondence between predicted saturation states and observed mineralogy enables evaluation of the water data, the water model, and the thermodynamic data. The second approach involves testing speculative reaction paths to simulate mass transfer processes associated with pitchblende oxidation and the generation of secondary uranyl silicates. Several modeling tests have been conducted, but none has provided results that completely represent the likely paragenesis of the Koongarra deposit. Results of one reaction-path model are discussed in this report to illustrate conclusions that have been obtained.

2.2.2.1. Equilibrium speciation of water samples from the PH49 well

The PH49 well intersects the zone of uranyl silicates in the Number 1 orebody at Koongarra (Snelling, 1980). Detailed (nearly 30 elemental species) chemical analyses of groundwater extracted in November 1988 and May 1989 from the 44 to 46 meter and 27 to 29 meter depth intervals of drillhole PH49, respectively, are reported in progress reports of the Alligator Rivers Project (Duerden, 1989; 1990). Equilibrium speciations at 25°C of these waters have been performed using the computer program EQ3 (version EQ3NR.3245R124) with its composite thermodynamic data base (version DATA0.COM.R7) (Wolery, 1983). The data and computations show that the waters are similar dilute solutions (ionic strength approximately $3x10^{-3}$) dominated by magnesium bicarbonate. At the measured pH of 7.01, the dissolved neutral CO_2 species contents are significant, resulting in equivalent CO_2 fugacities greater than 10^{-2} bar. These pressures are comparable to those of Yucca Mountain groundwaters, and are significantly in excess of the atmospheric CO_2 pressure. The aqueous silica contents exceed quartz solubility; however, they are about a factor of three lower than the silica contents of Yucca Mountain groundwaters. Calcium is the next most important cation, particularly on an equivalent basis. Sodium is significantly lower in PH49 water than in Yucca Mountain waters where it is the dominant cation. Chloride is the next most abundant anion in PH49 water. The measured uranium contents of PH49 water are high. A summary of data for these species in EQ3-modeled PH49 waters is given in Table 2-4.

The most significant difference between the analyses of the PH49 waters from the two depth intervals noted above is the measured oxidation state. The 27-29 m water is analyzed to be mildly reducing with an Eh of -0.08 volt, whereas the 44-46 m water is oxidizing with a Eh of 0.28 volt. The equilibrium distribution of redox sensitive aqueous species is strongly affected by this difference. For example, in the reducing solution dissolved uranium is calculated to exist almost entirely as neutral $U(OH)_4$. In the oxidizing solution, over 96 percent of the aqueous uranium is calculated to be complexed as uranyl carbonates.

Table 2-4. WATER CHEMISTRY FROM THE PH49 WELL AT THE KOONGARRA URANIUM DEPOSIT. CONCENTRATIONS (MOLAL) ARE CALCULATED BASED ON EQUILIBRIUM SPECIATIONS AT 25°C AND ADJUSTMENT OF BICARBONATE TO ACHIEVE CHARGE BALANCE.

Species/ Parameter	27-29 m May 1989	44-46 m November 1988	Simulation (Initial)
HCO_3^-	1.77×10^{-3}	2.38×10^{-3}	2.10×10^{-3}
Mg^{2+}	8.25×10^{-4}	9.67×10^{-4}	1.01×10^{-3}
$SiO_2(aq)$	3.02×10^{-4}	3.09×10^{-4}	3.26×10^{-4}
Ca^{2+}	7.55×10^{-5}	2.07×10^{-4}	1.27×10^{-4}
Cl^-	1.41×10^{-4}	5.64×10^{-5}	2.40×10^{-5}
Na^+	5.21×10^{-5}	5.64×10^{-5}	5.21×10^{-5}
Uranium (total)	4.48×10^{-7}	5.33×10^{-7}	1.55×10^{-7}
pH	7.01	7.01	7.83
Eh (volts)	-0.08	0.28	0.81
CO_2 fugacity (bars)	$10^{-1.97}$	$10^{-1.85}$	$10^{-1.72}$
Ionic strength	2.84×10^{-3}	3.64×10^{-3}	3.50×10^{-3}

The EQ3 computations indicate that the PH49 waters are saturated or supersaturated with numerous minerals, most of which fall in a few categories. The waters are approximately saturated with cristobalite, and supersaturated with the more stable silica polymorphs quartz and tridymite, a characteristic typical of low-temperature groundwaters. Supersaturations with respect to the ferrous iron compounds hematite, goethite, and magnetite are also typical of equilibrium calculations based on analytical groundwater data. In both solutions, witherite ($BaCO_3$) is approximately at saturation, and the solubility of thorianite (ThO_2) is exceeded. Thorianite supersaturation suggests control of thorium concentrations by more soluble phases such as monazite in which thorium occurs in solid solution. Thorum-bearing monazite has been detected in the Koongarra orebody (Edghill, 1990). The absence of analyses for aluminum precludes calculations of the saturation state with respect to common aluminosilicate minerals.

The oxidation states imposed on the simulated systems affect calculations of mineral saturation states. The more reducing water is calculated to be supersaturated with respect to the uranium oxides UO_2 (uraninite), $UO_{2.25}$, and $UO_{2.3333}$. The former is the quadravalent uranium oxide, and the latter compounds are mixed oxides with partial uranium oxidation. In contrast, the computations show that the oxidizing solution is supersaturated with respect to the uranyl silicate minerals haiweeite and soddyite. The validity of the reduced oxidation state measured for the 27-29 m sample is challenged by calculated supersaturations with respect to native copper and native selenium and numerous copper and selenium compounds including chalcocite (Cu_2S) and several transition metal selenides. These supersaturations are unrealistic. In the reducing solution, selenium and copper are calculated to occur primarily as HSe^- and Cu^+. In contrast, in the oxidizing solution selenium occurs as SeO_4^{2-} and copper as Cu^{2+} and as carbonate and hydroxide complexes of Cu^{2+}. With total selenium and copper contents comparable to the reducing solution, this difference in speciation results in no unrealistic supersaturations with respect to selenium and copper minerals for the oxidizing solution. An error in the measured Eh value for the 27-29 m water or an error in the general application of the measured Eh value to all redox reactions is indicated by these results.

2.2.2.2. Reaction-path modeling of the silicate zone at Koongarra

Geochemical reaction-path analyses require development of conceptual models for important processes controlling mineral and water chemistry. Thermodynamic and kinetic models of the ambient water-rock system at Yucca Mountain appear to give reasonable results when initial groundwater compositions in reaction-path models are based on likely recharge scenarios, and mineral reactants and products correspond to the observed primary and secondary solids (Murphy, 1991). Although good data exist for the compositions of present-day groundwaters at Koongarra, the origin of waters involved in generation of the silicate-zone mineral assemblage at Koongarra is speculative. Prior research at Alligator Rivers indicates that the uranyl silicate mineralization resulted from reaction of groundwaters with primary pitchblende in the chlorite schist host rocks of the deposit (e.g. Snelling, 1980). As an initial attempt to identify a likely conceptual model for this process, calculated reactions of a water based on the actual chemistry with minerals observed in the system can be judged for the accuracy of their representation. Of several scenarios for this process that have been tested, results of one are summarized in this section, which illustrate the basis for the general conclusions.

The initial water chemistry in the simulation is based on the analysis of water collected in November 1988 from the 28 to 30 m depth in the PH49 well at the Koongarra ore body. This water resembles closely those described above. Its oxidation state is intermediate between the two, but dominantly oxidizing at Eh 0.13 volt. Uranium is calculated to exist in the water as uranyl carbonate complexes. The equilibrium CO_2 fugacity is calculated to be $10^{-1.72}$ bar. The chemistry of the initial water has been simplified to facilitate complicated reaction-path computations by eliminating many minor species that are unlikely to play a critical role. Nevertheless, the modeled water contains fifteen elemental components in addition to oxygen and hydrogen. Aluminum is included among the components, allowing

calculation of secondary clay mineral precipitation. Oxygen (Eh) and carbon dioxide fugacities in the water are buffered (Table 2-4).

The modeled reaction path consists of the oxidative dissolution of uraninite and pyrite, together with dissolution of chlorite and apatite. The four reactants are assumed to dissolve at equal rates. Uraninite oxidation and dissolution are included in the model because this process is regarded as the likely source of uranium for observed uranyl silicate mineralization. Pyrite oxidation and dissolution are included to test the effects on solution pH. Chlorite and apatite dissolution are included to examine the effects of respective introduction of magnesium and phosphate to the system because predominant secondary phases contain these elements at Koongarra. Several minerals in the EQ6 database that seem unlikely to form in the Koongarra environment are suppressed so that the modeled solutions along the reaction path become supersaturated with respect to them. Excluded minerals include silica polymorphs more stable than cristobalite and the Mg-bearing carbonates dolomite and magnesite. Also, the uranyl silicate mineral soddyite is suppressed in an effort to test for the generation of more typical calcium, magnesium, or phosphorous bearing uranium minerals.

At the outset of the model reaction, the initial water is equilibrated with a stable mineral assemblage. All disallowed supersaturations are eliminated by precipitation of secondary phases. The solution is calculated to be in equilibrium with haiweeite, hematite, Mg-montmorillonite, and pyrolusite. Characteristics of the water chemistry following the initial equilibration are summarized in Table 2-4. As the dissolution reactions proceed, a dominant effect is the conversion of the magnesium-rich chlorite to Mg-montmorillonite. This reaction consumes silica, and the aqueous silica concentration decreases. Eventually the decrease in aqueous silica leads to replacement of Mg-montmorillonite by kaolinite, and then to the appearance of gibbsite, which together with kaolinite buffers the aqueous silica activity.

The addition of calcium to the solution from apatite and a small increase in pH due to silicate hydrolysis lead to calcite precipitation. Further increase in magnesium in solution leads to huntite ($CaMg_3(CO_3)_4$) precipitation. This is an unlikely phase, but together with calcite its production is analogous to the formation of magnesian calcite, which is observed at Koongarra (Snelling, 1980). Addition of phosphate to the solution by dissolution of apatite does not generate saturation with respect to uranyl phosphate minerals such as those observed at Koongarra. Instead, uraninite oxidation leads to the precipitation of the calcium uranyl silicate, haiweeite. This reaction also contributes to the depletion in the solution of silica.

In general this reaction-path calculation appears to provide a poor representation of geochemical events at Koongarra. Silica drops to unrealistically low values. Although growth of calcite is consistent with field observations, the carbonate phase huntite is unrealistic. The formation of a uranyl silicate by oxidation of uraninite is generally consistent with the Koongarra orebody, but the specific mineral haiweeite predicted in the model is not reported at Koongarra. This may be a consequence of inaccurate thermodynamic data for the uranyl silicates as well as other model deficiencies. Uranium phosphate minerals observed at Koongarra are also absent in the modeled system. Additional conditioning of the model will be

required to develop a good understanding of the evolution of the Koongarra system. In particular, open-system metasomatism could be included in the model to allow introduction of silica to the system. Field relations described by Snelling (1980) indicate that the generation of secondary uranium minerals was associated with growth of high-silica chlorite and general silicification. Controls on aqueous silica activities in the Koongarra silicate zone are uncertain in the absence of metastable silica-rich phases. An external source appears to be required. In addition, thermodynamic data for the magnesian montmorillonite and haiweeite should be evaluated. Their stability in the model precludes formation of the observed secondary chlorite and uranyl silicate assemblage. The occurrence of chlorite rather than clays in the ore deposit also suggests that elevated temperatures may have been important during the silicification process. Independent constraints on the temperature of formation should be investigated to refine the model.

2.2.3. Conclusions

Equilibrium aqueous speciations of groundwaters from the Koongarra site and reaction-path simulations of the geochemical evolution of the silicate zone at Koongarra aid interpretation of the analytical groundwater chemistry data and evaluation of the conceptual and thermodynamic models of the system. Reported reducing conditions for the PH49 well water at the 27-29 m depth appear to be incompatible with other chemical data and reasonable mineral saturation states, and are probably unrepresentative. A uranyl silicate mineral assemblage is compatible with the water chemistry, but the specific calculated phases do not represent the observed assemblage, suggesting a refinement of the thermodynamic data base for uranium minerals is required. The conceptual model for the evolution of groundwater and mineral chemistry corresponding to reaction of uraninite, pyrite, chlorite, and apatite with a typical silicate-zone groundwater requires refinement to be realistic. The aqueous silica concentration has been identified to have an important effect on the secondary mineral assemblage. Adequate representation of the alteration geochemistry at Koongarra may require a system open to species such as silica as well as the volatile species CO_2 and O_2.

2.3. References

Brady, P.V. and J. V. Walther. 1990. Kinetics of quartz dissolution at low temperatures. *Chemical Geology*. 82: 253-264.

Brunauer, S., P. H. Emmett, and E. Teller. 1938. Adsorption of gases in multimolecular layers. *J. Amer. Chem. Soc.* 60: 309-319.

Duerden, P. (editor) 1989. *Alligator Rivers Analogue Project Progress Report 1 June 1989 - 31 August 1989.* Menai, Australia: Australian Nuclear Science and Technology Organization.

Duerden, P. (editor) 1989. *Alligator Rivers Analogue Project Progress Report 1 March 1990 - 31 May 1990.* Menai, Australia: Australian Nuclear Science and Technology Organization.

Duerden, P. (editor) 1990. *Alligator Rivers Analogue Project Annual Report 1988-1989.* Menai, Australia: Australian Nuclear Science and Technology Organization. Menai, Australia.

Edghill, R. 1990. The distribution of uranium and thorium between phases in weathered core from Koongarra. *Alligator Rivers Analogue Project Annual Report 1988-1989.* Menai, Australia: Australian Nuclear Science and Technology Organization: 79-92.

Fanning, K. A. and M. E. Pilson. 1973. On the spectrophotometric determination of dissolved silica in natural waters. *Anal. Chem.* 45: 136.

Gottardi, G. and E. Galli. 1985. *Natural Zeolites.* New York: Springer-Verlag.

Holdren, G. R., Jr. and R. A. Berner. 1979. Mechanism of feldspar weathering. I. Experimental studies. *Geochim. Cosmochim. Acta.* 43: 1161-1171.

Murphy, W. M. 1991. Geochemical modeling. W. C. Patrick, ed. *Center for Nuclear Waste Regulatory Analyses Report (CNWRA) on Research Activities for Calendar Year 1990.* CNWRA 90-01A. San Antonio, Texas: CNWRA.

Schott, J., S. Brantley, D. Crerar, C. Guy, M. Borcsik, and C. Williame. 1989. Dissolution kinetics of strained calcite. *Geochim. Cosmochim. Acta*, 53: 383-398.

Shull, K. E. and G. R. Guthan. 1967. Rapid modified Eriochrome cyanine R method for determination of aluminum in water. *Jour. Amer. Water Works Assoc.* 59: 1456.

Snelling, A. A. 1980. A geochemical study of the Koongarra uranium deposit, Northern Territory Australia. Ph.D. thesis (unpublished). Sydney, Australia: University of Sydney.

Sverjenski, D. A. 1990. Chemical mass transfer calculations for the formation of the uranium phosphate zone at Koongarra. *Alligator Rivers Analogue Project Progress Report 1 March 1990 - 31 May 1990.* Duerden, P., (ed) Menai, Australia: Australian Nuclear Science and Technology Organization: 19-29.

Wolery, T. J. 1983. *EQ3NR A Computer Program for Geochemical Aqueous Speciation-Solubility Calculations: User's Guide and Documentation.* UCRL-53414. Livermore, California: Lawrence Livermore National Laboratory.

3. THERMOHYDROLOGY

by Ronald T. Green (CNWRA) and Franklin T. Dodge (SwRI)

Investigators: Ronald T. Green (CNWRA), Franklin T. Dodge (SwRI), Ronald H. Martin (CNWRA), and Steve J. Svedeman (SwRI)

3.1. INTRODUCTION

Technical issues and uncertainties for the proposed Yucca Mountain HLW repository site indicate a need for research on thermohydrological phenomena, i.e., phenomena associated with heat and fluid flow, to provide information relevant to performance assessment (PA) and design criteria. The class of thermohydrological phenomena examined in this project includes phenomena driven by heat emanating from HLW emplaced in a geologic repository. Information derived principally from research is used to establish a knowledge base of thermohydrologic phenomena which will be utilized to assess models of processes used in PAs. This report summarizes the progress of the Thermohydrology Research Project performed during the first quarter of 1991.

3.2. TECHNICAL OBJECTIVES

The specific objectives of the Thermohydrology Research Project are summarized as follows:

- Perform a critical assessment of the state-of-knowledge of thermohydrology in unsaturated fractured media, in the context of present HLW-NRC program activities. This assessment will require an in-depth review of existing literature and on-going programs. The assessment will focus on flow processes, heat transfer mechanisms, and the state-of-the-knowledge experimental methods in porous media.

- Perform a detailed dynamic similarity or similitude analysis on the complete set of governing equations relevant to unsaturated flow and determine the set of dimensionless parameters required to conduct appropriate laboratory simulations. In this analysis of modeling parameters, the range of parameter applicability and limitation on the magnitude of these parameters, as constrained by the principles of dynamic similarity, will be determined.

- Identify potential problems associated with the design and performance of laboratory simulations with scaled geometry, fluid, media, and other relevant properties subject to modeling distortion.

- Perform a series of separate effects experiments in order to identify and understand the role of each effect in the overall coupled processes involved in thermohydrologic phenomena.

- Design and perform comprehensive experiments whose results will continue to identify key dependent and independent parameters and their relationships to each other in the context of thermohydrologic issues.

- Develop the laboratory facilities, experimental methods, measurement techniques, and associated analytic skills to evaluate and validate other program results and to provide a high quality of technical assistance and research in support of NRC's licensing of a HLW repository.

- Examine and correlate laboratory results with field data to aid in the design of future field experiments.

The research project has been delineated into five tasks for the purpose of accomplishing these objectives. Three of these tasks are active at this time: Task 1, Assessment of the State-of-Knowledge of Thermohydrology in Unsaturated Media; Task 2, Design and Execution of Preliminary Separate Effects Experiments; and Task 3, Design of Unsaturated Zone Thermohydrological Experiments.

3.3. SEPARATE-EFFECTS EXPERIMENTS

A total of six separate-effects experiments have been conducted as part of Task 2 of the Thermohydrology Research Project. The sixth experiment was completed during this quarter and is described below.

3.3.1. Test 6

Test 6 was designed to measure thermally induced fluid movement in a porous partially saturated, fractured medium. The test was intended to repeat Test 5 with several modifications to the test apparatus that would allow a more controlled test.

Test 6 initiated in late October, 1990, was completed in late February, 1991. The boundary conditions for Test 6 were the same as Test 5 with the exception that the temperatures maintained in the heat exchangers during Test 6 were held constant and not reversed as in Test 5. The protocol in Test 6 was designed to be similar to Test 5 (see below) with the anticipation that improvements in laboratory procedure and instrumentation measurement would provide more quantitatively significant results.

3.3.1.1. Experimental Apparatus Setup

Several changes to the experimental apparatus used in Test 5 were implemented prior to starting Test 6. The width of the test chamber was increased from 1.9 cm to 5.3 cm to increase the "contrast" in the water-saturation readings taken with the gamma densitometer. The overall design of the test container was modified to reduce problems attributed to sealing and assembly difficulties. A schematic of the test container showing

dimensions and locations of instrumentation is given in Figure 3-1. As illustrated in the schematic, two tensiometers were installed in the media to measure matrix (suction) pressure. The dye injection ports were installed to within 0.3 cm of the front face. This arrangement minimized the amount of injected dye required before the dye was visible at the front face. Other adaptations to the test chamber included the installation of thicker insulation on the container (3.8-cm), installation of three thermistors on the back plexiglass face to monitor the effects of ambient temperature variations, and the inclusion of a 5.1-cm thick lead shield over the densitometer radiation source to collimate the gamma rays through a 0.6-cm diameter orifice.

A 50 percent - 50 percent by volume mixture of two different sizes of glass beads was used in Test 6. The two bead-size classes were factory sieved between 74-105 μm and 28-53 μm. The beads were manually mixed with enough water to provide an average saturation of 65 percent and then packed into the test container. A simulated fracture was placed mid-way between the two heat-exchanger (HE) plates by emplacing a thin layer of larger beads (sieved between 125-170 μm). The layer of beads consisted of 3 ml of beads spread over an area that was 5.3 cm x 20.3 cm with an average thickness of about 300 μm.

3.3.1.2. Experimental Protocol

Test 6 was started immediately after the glass beads were packed into the test container and the container was positioned vertically (so that the HE plates and simulated fracture were oriented vertically) on the test stand. The fluid circulating through both HE plates was initially set at 20°C, and the data acquisition system was started to record the instrument readings. After six days, the temperature of fluid circulating through the right HE plate was increased to 60°C. These boundary temperatures were maintained until day 105 when the temperature of the right HE plate was decreased to 20°C. The medium was then saturated, and the attenuation of the media at 100 percent saturation was recorded with the gamma-ray densitometer. The test was terminated after 120 days. The experimental protocol is summarized in Table 3-1.

3.3.1.3. Experimental Results

Dye tracing was used to monitor the movement of liquid water through the media. Dye was injected into the media five times (Table 3-1), and its movement was recorded by periodically photographing the test container. The dye showed water-movement patterns changed as the test continued. The dye was initially injected near the left HE held at 20°C (2.5 cm from the plate and 7.0 cm above the bottom of the container) had a very slow downward migration. Initially the dye diffused radially outward, then infiltrated downward about 0.6 cm over 6 days. Subsequent injections showed the dye moved slowly upwards. Later in the test, dye injected in the same position initially migrated toward the bottom of the container and then inward toward the simulated fracture. Because the dye continuously diffused, it could only be followed for a short time before it became too faint to clearly trace. Nevertheless, the dye movement illustrated that the flow pattern was more complicated than simple convection patterns created by surface-tension gradients, gravity, or heat-pipe effects.

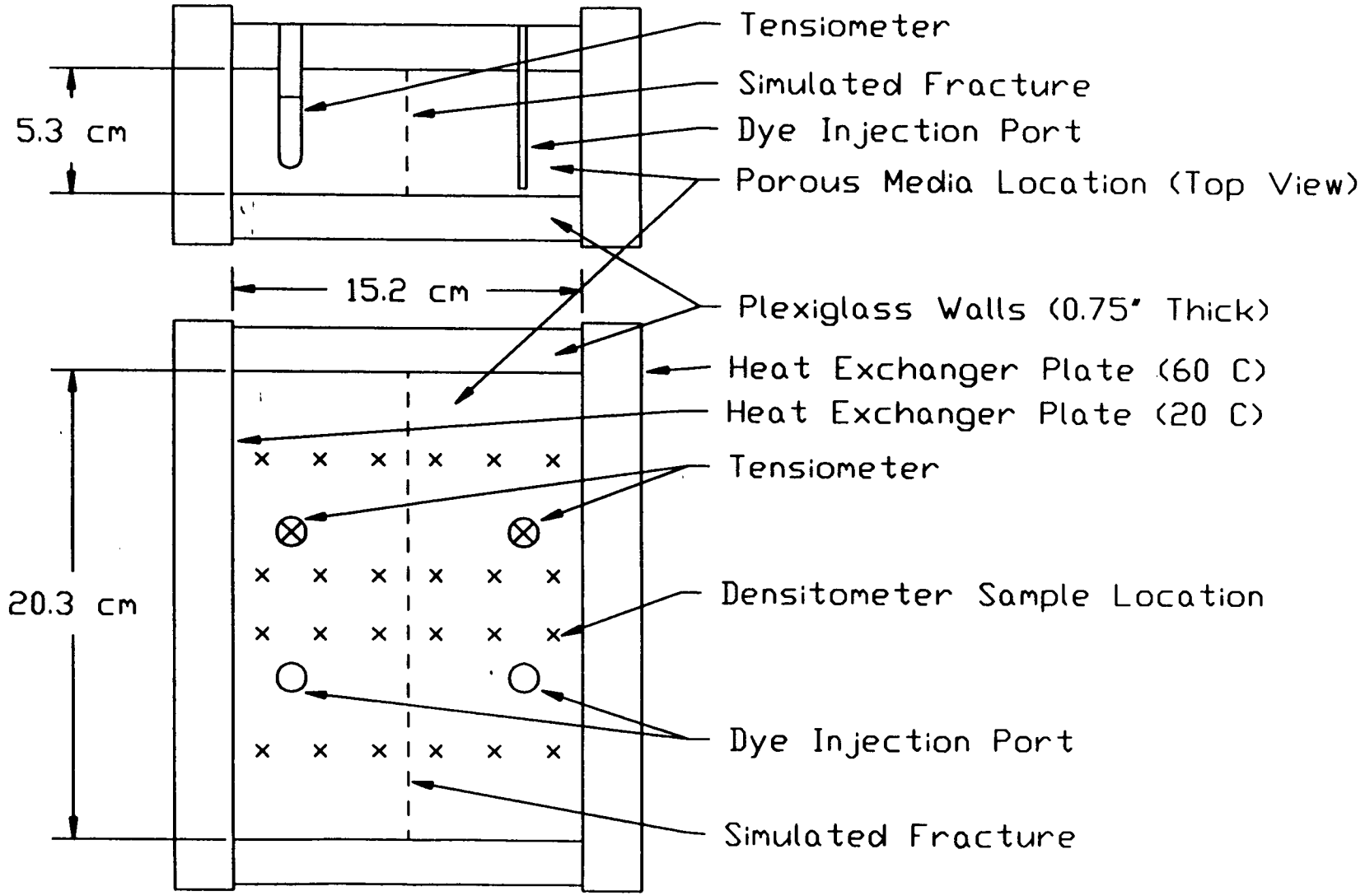

Figure 3-1. Test 6 container size and instrumentation positions

Table 3-1. PROTOCOL FOR SEPARATE EFFECTS TEST 6

Date	Time	Event During Test 6	Photo #	# Days
10/31/90	12:55 PM	Test started. Media at 65% saturation. Heat-exchanger plates at 20°C. Tensiometers not installed.	14	0
11/06/90	9:00 AM	Installed tensiometer pressure gauges. Set right heat exchanger at 60°C. Injected 0.1 cc dye in each dye injection port.	15	5.9
11/12/90	8:15 AM	DAS failed over weekend, restarted.	2	11.8
11/13/90	8:22 AM	Adjusted left-side HX temperature from 22 to 20°C.	5	12.8
11/14/90	8:10 AM	Injected 0.1 cc dye in each port.		13.8
11/27/90	8:50 AM	Injected 0.1 cc dye in each port.	18	48.1
12/03/90	8:50 AM	Refilled tensiometer 5 (it dried out). (DAS restarted from 12/2/90 failure.)	23	32.8
12/07/90	1:20 PM	DAS restarted (was off because sample period was less than scan time).		37.0
12/18/90	3:25 PM	Injected 0.1 cc dye in each port.	2.7	48.1
01/07/91	9:00 AM	Insulation on front of container was left off from 1/4/91. Refilled tensiometer 5.		67.8
01/08/91	8:15 AM	DAS restarted after failure.		68.8
01/08/91	10:40 AM	Injected 0.1 cc dye in each port.	2.12	
01/18/91	1:15 PM	DAS restarted after failure.	3.4	79.0

DAS = Data Acquisition System

Table 3-1. PROTOCOL FOR SEPARATE EFFECTS TEST 6 (cont'd)

Date	Time	Event During Test 6	Photo #	# Days
01/21/91	9:50 AM	Dye showed the simulated fracture effectively stopped dye movement from hot toward cool side.	3.6	81.8
01/28/91	12:00 PM	Switched to digital interface between DAS and Ludlum densitometer.		88.9
01/31/91	2:50 PM	DAS restarted. DAS off from 1/30/91 at 10:49 AM.	3.16	92.1
02/04/91	11:45 AM	Refilled tensiometer 5.		95.9
02/08/91	10:00 AM	DAS down (failure of IBM-PC).	3.17	99.5
02/11/91	4:00 PM	DAS repaired. PC hard-disk controller replaced.		103.1
02/13/91	4:00 PM	Set both heat-exchanger plates to 20°C.	3.18	105.2
02/14/91	9:00 AM	Densitometer standard #2 reading from 2/13/91 at 4:15 PM may be bad because aluminum block had been knocked off stand.	3.19	105.8
02/18/91	4:20 PM	Tensiometer 4 refilled.		110.1
02/22/91	9:25 AM	Started effort to extract water sample from media.	3.21	113.7
	5:04 PM	Started injecting water into bottom of container to saturate media.		
02/25/91	2:10 PM	Media saturated. 210 mL water added to container. Tensiometers read +0.15 psig.	3.24	
	2:41 PM	Restarted DAS to record 100% saturation readings.		117.1
03/01/91	8:15 AM	DAS turned off since enough 100% saturation readings had been taken.	3.25	120.6

DAS = Data Acquisition System

Dye injected near the right HE plate (heated to 60°C) indicated much faster water movements compared to dye injected near the left (cooler) HE. Initially this former dye moved quickly upward and migrated closer to the higher temperature HE plate. After the dye was next to the HE, it quickly descended (3.8 cm in 3 days) along the HE face. Upon reaching the bottom of the container, the dye moved slowly along the bottom of the container toward the fracture. The dye was not observed to cross the fracture.

The media in the lower corner of the test chamber nearest the right HE appeared to dry out as the test progressed. The drying front advanced most rapidly along the bottom edge of the test chamber. After 28 days, glass beads within about 0.6 cm of the right HE appeared to have dried out. This was evident because the beads became lighter in color as the moisture content in the beads dropped. The dry region next to the HE continued to grow slowly throughout the duration of the test with the dry region extending out considerably further near the bottom of the container than at the top. The dry region near the bottom of the container extended about 4.4 cm from the HE and about 1.3 cm at the container midpoint. The dry region at the top of the container did not increase in depth much beyond about 0.6-cm.

Dye appeared to become concentrated in the interface region between the wet and dry beads. This concentrated dye became immobile in the beads that appeared to dry out. Subsequent dye injections behaved in the same fashion with the exception that the dye moved downward along the interface between the wet and dry media and did not cross into the dry regions. The dye usually became too faint to see before reaching the simulated fracture with the exception of the last dye injection. In this case, the dye moved along the bottom of the container to the fracture. When it reached the fracture, it appeared to migrate upward along the fracture but did not cross it. However, it was not possible to discern whether water was crossing the fracture below the visible surface layer.

Throughout the test, water distribution in the media visibly changed, indicating that even with a relatively small test setup, the amount of time required to reach a steady-state conditions is significant.

3.4. DIMENSIONAL ANALYSIS

3.4.1. Background

The geologic medium at the proposed repository horizon for HLW emplacement is a variably saturated, highly fractured, welded tuff. The movement of water and vapor due to localized heating by the waste packages may have a significant influence on the performance of the repository. Unfortunately, the physics of this coupled thermohydrological flow is not as yet completely understood for the medium of low permeability in the matrix and high permeability in the fractures existing at the proposed repository site. For that reason, numerical experiments are integrated with laboratory experiments to investigate thermohydrological phenomena.

Understanding is limited of the coupled flow processes involved with the placement of heat-generating waste located in variably saturated fractured rock. Prior to the 1980's, prospective candidate sites for geologic HLW repositories were located exclusively in the saturated portion of the subsurface. Only in recent years, with the potential of a HLW repository being located in the vadose zone, has attention been focused on nonisothermal processes affecting flow and transport through unsaturated, fractured media. Although placement of HLW in the unsaturated zone is attractive because a perceived lack of significant mobile water available for transport of radionuclides may exist, the physics defining nonisothermal flow and transport in the unsaturated zone are significantly more complicated than those for the saturated zone.

Early evaluation of thermohydrological phenomena affecting flow and transport associated with HLW disposal in the unsaturated zone relied upon analogous studies of geothermal processes (Pruess et al., 1979), application of basic soil physics principles, and reconnaissance laboratory investigations (Evans, 1983). Subsequent to these pioneering efforts, more recent advances have been made in defining the governing physical principles, execution of laboratory- and field-scale experiments, and a new generation of computer models used to perform numerical simulations of thermohydrological processes. Significant progress has been accomplished using these technical approaches.

Areas of uncertainty still remain in understanding the thermohydrological phenomena associated with disposal of heat-generating waste in unsaturated fractured rock. By their nature, the processes controlling flow and transport for this setting are complex and coupled. Separating the individual contributing processes for purposes of investigation and evaluation is not simple and may provide misleading results, while evaluation of coupled processes is cumbersome and often times not feasible.

Evaluation of these flow and transport processes becomes even more difficult when the concept of scale is introduced. Observed laboratory- and field-scale data are used to help assess the capabilities of computer models to accurately simulate flow and transport under these conditions. However, observable and quantifiable data appropriate for this use are scarce and typically unavailable at sufficient spatial and temporal scales. Most data are from laboratory-scale test cases, although limited data at field scale are available, and are for time scales significantly shorter than the proposed design duration of a geologic repository. Adding to this dilemma are the difficulties that arise from the nonlinear nature of flow under partially saturated conditions and from the vast differences in scale and the hydraulic characteristics between the matrixes and fractures of the geologic media.

Dimensional analysis has been proposed in this project as a method to apply the available database and simulation models to the long-term, full-scale geologic repository. In particular, dimensional analysis has been used to determine nondimensional formulations of the governing equations for the physical processes associated with nonisothermal flow through unsaturated, fractured porous media. A set of nondimensional pi terms has been determined from these equations. The parameters contained in the pi terms were assigned values endemic

of the physical characteristics of a series of laboratory-scale separate effects experiments conducted at the CNWRA. Pi terms identified as being important were selected for further evaluation. These pi terms were numerically evaluated using a numerical code, TOUGH, (Pruess, 1987) to assess the sensitivity of the flow regime to changes in the values of the pi terms. The importance of the pi terms has been further assessed using this additional information.

The review of TOUGH used in these calculations was adapted from MCTUFF aversion, which had been modified by the NRC. Additional operational modifications were implemented into TOUGH to permit running on a VAX 8700 as SwRI.

3.4.2. Experimental Database

The database upon which the dimensional analysis was applied was taken from Tests 5 and 6 of the separate effects thermohydrological experiments. Although it was the intention of these laboratory-scale experiments to be analogous to a field-scale repository, inherent differences are encountered due to the temporal- and spacial-scale contrasts between the two systems.

The experimental apparatus used in the separate-effects experiments was a vertically oriented, two-dimensionally configured test chamber with constant temperature HEs located along the two vertical edges. The temperature at the HE on the right was held constant at 60°C and on the left at 20°C. The test chamber was filled with a partially saturated, indurated porous medium with a simulated vertically-oriented fracture located midway between the two HEs.

The physical characteristics of the test media were measured when possible and estimated using published data otherwise. The tests were monitored for temperature, suction pressure and moisture content using thermistors, tensiometers, and a gamma-ray densitometer, respectively. Additionally, liquid water flow was monitored by photographing the movement of injected dyes through the transparent side walls of the test chamber.

Nominal values for the physical characteristics of the separate effects experiments have been selected for use in the dimensional analysis. These values are listed in Table 3-2. For the purposes of this assessment, the effect of the fracture has not been incorporated into the evaluation.

3.4.3. Nondimensional Equations and Pi Terms

This dimensional analysis of the transient thermohydraulic response of a variably saturated, fractured porous medium is based both on the integral conservation equations in the TOUGH code (Pruess, 1987) modified to include liquid transport between the matrix and the fractures (Updegraff and Lee, 1990) and the separate-effects experiments described in this paper. The following assumptions are made: (1) the amount of gas dissolved in the liquid phase is small

Table 3-2. NOMINAL VALUES FOR BASE CASE

Symbol	Definition	Value	Units
C_{Pa}	Specific heat for air, constant pressure		J/kg-K
C_{Va}	Specific heat for air, constant volume		J/kg-K
C_W	Specific heat for water	4180	J/kg-K
C_s	Specific heat of rock	800	J/kg-K
d_o	Typical dimension of matrix width	1E-5	m
D_{va}	Diffusion coeff. for air-vapor mix	1E-4	m^2/s
g	Gravity vector	9.80665	m/sec^2
h_g	Enthalpy of air saturated water (40°C)	1.67E5	J/kg
h_w	Enthalpy of water (40°C)	1.67E5	J/kg
k_m	Matrix permeability	1.2E-14	m^2
L_H	Heater length	0.51	m
P_g	Gas pressure	1E5	N/m^2
t	Time	-	s
T	Temperature	293-333	K
T_o	Reference temperature	273	K
X_W	Mass fraction of liquid water in liquid	1	-
Y_W	Mass fraction of water vapor in gas		-
β_g	Thermal expansion coefficient of gas		
μ_g	Gas viscosity	2E-5	$N\text{-}sec/m^2$
μ_W	Water viscosity	7E-4	$N\text{-}sec/m^2$
κ	Rock-water thermal conductivity	1	J/m-s-K

Table 3-2. NOMINAL VALUES FOR BASE CASE (cont'd)

Symbol	Definition	Value	Units
ρ_g	Gas density	1	kg/m^3
ρ_s	Matrix density	2500	kg/m^3
ρ_w	Water density	1000	kg/m^3
σ	Surface tension of water	72.8	N/m
ϕ	Matrix porosity	0.35	-
dP_c/dS_w	Ratio	-2.91E4	N/m
$d\sigma/dT$	Ratio	-0.17	N/m-K

(so the liquid phase density is that of the liquid); (2) the mixture of air and liquid vapor in the gas phase is an ideal gas; (3) the matrix-fracture volume of interest can be treated by a dual porosity model; (4) thermal equilibrium is obtained instantaneously between the fluid and solid phases; (5) the liquid and gas are distributed continuously (e.g., any point in the liquid can be reached by any other point in the liquid by a path that lies completely in the liquid); and (6) no sources or sinks of liquid or gas exist within the volume of interest.

The integral water-mass-balance equation for the matrix is

$$\frac{d}{dt}\iiint M dV = \iint (\mathbf{F}_l + \mathbf{F}_g) \cdot \mathbf{n} dA - \iiint \rho_w X \Gamma_{mf} dV \qquad (3\text{-}1)$$

where the integral on the left represents the change in the mass of water M stored in the volume, the surface integral on the right represents the flux F of water (both liquid l and gas g phases) into the volume, and the volume integral on the right represents the transport of water between the matrix m and the fractures f. Here, ρ_w is the density of water, X is the mass fraction of liquid water in the liquid phase, and T_{mf} is a function that specifies the transport of water between the matrix and the fracture per unit volume. A similar integral equation can be written for the fractures.

The flux terms in Eqn. (3-1) are evaluated by Darcy's law, augmented by diffusion between the liquid vapor and air. To examine dimensional implications, the Boussinesq approximation is used to relate the gas density, pressure, and temperature:

$$\nabla P_g - \rho_g \mathbf{g} = \nabla P_{go} - (\rho_g \beta_g \Delta T)\mathbf{g} \tag{3-2}$$

where P_{go} is a small nonhydrostatic component that is neglected in the following. The thermal expansion coefficient of the gas is β_g and T is the temperature. From the fifth assumption above, the liquid pressure P_w is also hydrostatically distributed. But at any point where liquid is in contact with gas, the liquid pressure is also related to the gas pressure by the capillarity-induced "jump" in pressure P_{cap} across the liquid-gas interface:

$$P_w = P_g - P_{cap}. \tag{3-3}$$

Since, when the saturation is less than unity, liquid pressure is controlled by capillarity rather than by buoyancy, there can be no buoyancy-driven convection cells that are of the size of the matrix-fracture volume. Such cells can exist only on the scale of a pore completely filled with water. Circulation on the scale of the volume can occur, but it must be driven by pressure gradients or other phenomena.

Obviously, capillary pressure is an important part of the response of the fractured porous medium. Generally, P_{cap} is computed as a function of the local liquid saturation S by empirical correlations of the general form $P_{cap} = P_o f(s)$ where both P_o and the functional form f are determined experimentally. At locations where the liquid-gas interface area is not microscopic, capillary pressure depends directly on the liquid surface tension and the pore size, and the pressure is usually no more than one to two atmospheres (suction), which correspond to moderate saturation levels (i.e., $S > 0.7$). Since moderate saturation levels are of primary interest here, it is legitimate to assume that P_o depends directly on surface tension σ; that is, $P_o = P_c \sigma / d_o$ where P_c is a nondimensional function of S determined experimentally and d_o is a representative capillary dimension such as pore diameter. (For very low saturations, capillary suction pressures can be of the order of tens of atmospheres. The physical basis of these pressures is more likely to be adhesion of water molecules to the surface rather than surface tension.)

Altogether, the equation representing the conservation of water is:

$$\begin{aligned}
&\frac{d}{dt}\iiint \Phi\left[\rho_w XS + \rho_g Y(1-S)\right]dV = \\
&\quad -\iiint \gamma\sigma X\left(\frac{K_{RW}}{V_w}\right)\left[\left(\frac{P_c}{d_p}\right)_w - \left(\frac{P_c}{d_o}\right)_f\right]dV \\
&\quad +\iint X\left(\frac{kk_{RW}}{V_w}\right)\left[\frac{\sigma}{d_o}\left(\frac{dP_c}{dS}\right)\nabla S + \frac{P_c}{d_o}\left(\frac{d\sigma}{dT}\right)\nabla T\right. \\
&\qquad \left. -\frac{\sigma P_c}{d_o^2}\nabla d_o + (\rho_w + \rho_g)\mathbf{g}\right]\cdot \mathbf{n}dA \\
&+\iint Y\left(\frac{kk_{Rg}}{V_g}\right)\rho_g^2\beta_g\Delta T\mathbf{g}\cdot\mathbf{n}dA - \iint D_{va}\rho_g\nabla Y\cdot\mathbf{n}dA
\end{aligned} \tag{3-4}$$

Here, ϕ is the porosity of the matrix, Y is the mass fraction of water in the gas phase, k is the intrinsic permeability, k_{Rw} and k_{Rg} are the relative permeabilities for liquid and gas flow, V_w and V_g are the liquid and gas viscosities, and γ is an empirical coefficient.

Note that the capillary-induced pressure can vary from point to point by three different mechanisms: (1) the liquid saturation is different; (2) the temperature and therefore the surface tension is different; or (3) the bore size is different. Equation (4) is made nondimensional by introducing the initial temperature T_o and the length L_H of the embedded heater or heated boundary as characteristic parameters. The nondimensional form is:

$$\begin{aligned}
&\frac{d}{d\tau}\iiint\left\{\left(\frac{1}{Pr}\right)\phi XS + \bar{\rho}Y(1-S)\right\}d\bar{V} = -\iiint \gamma X k_{Rw}\left(\frac{L_H^2}{k}\right)Ca\,(1-\bar{P})\,d\bar{V} \\
&\quad +\iint X k_{Rw} Ca\left[\left(\frac{dP_c}{dS}\right)\bar{\nabla}S + Si\,\bar{\nabla}\theta - \frac{1}{D}\bar{\nabla}D + Bo\,(1-\bar{\rho})\,\mathbf{k}\right]\cdot\mathbf{n}d\bar{A} \\
&\quad +\iint (Y k_{Rg}\bar{\rho}\bar{v}Gr\theta)\,\mathbf{k}\cdot\mathbf{n}d\bar{A} - \iint\left(\frac{1}{Sc}\right)\bar{\nabla}Y\cdot\mathbf{n}d\bar{A}\ .
\end{aligned} \tag{3-5}$$

The nondimensional parameters, or "pi" terms, in Eqn. (3-5) are listed by category in Table 3-3, along with estimates of their numerical values. (Note that the matrix-fracture pressure interaction term, $\bar{P} = (P_c/d_o)_f/(P_c/d_o)_m$, is not an independent pi term and so is not included in the table; that is, it can be formed from other pi terms that are included in the table.)

Table 3-3. DEFINITION OF NONDIMENSIONAL TERMS

π	Symbol	Definition	Type	Value
1	D	d_o/L_H	Geometry	$<10^{-3}$
2	K	k/L_H^2	Geometry	$<10^{-9}$
3	θ	Porosity	Geometry	0 - 1
4		ρ_g/ρ_w	Property ratio	≈ 0.001
5		ρ_s/ρ_w	Property ratio	≈ 2.7
6		V_g/V_w	Property ratio	≈ 0.03
7		C_s/C_w	Property ratio	≈ 0.2
8		C_{Pa}/C_w	Property ratio	≈ 0.00021
9		C_{Va}/C_w	Property ratio	≈ 0.00017
10	U	u_{fg}/C_wT_o	Property ratio	≈ 1.74
11	H	h_{fg}/C_wT_p	Property ratio	≈ 1.96
12	k_{Rw}	Liquid relative permeability	Physical effect	10^{-7} to 1
13	k_{Rg}	Gas relative permeability	Physical effect	10^{-7} to 1
14	B_o	$\rho_w g L_H/\sigma d_o$	Physical effect	≈ 0.1
15	Ca	$\sigma k/d_o\rho_w V^2{}_w$	Physical effect	≈ 0.84
16	Pr	$\rho_w/\rho_s)(C_s\rho_w V_w/\kappa$	Physical effect	≈ 0.21
17	dP_c/dS	Pressure moisture relationship	Physical effect	≈ -20
18	Si	$P_cT_o/\bar{\sigma}(d\sigma/dT)$	Physical effect	≈ -10
19	Gr	$kL_Hg\beta_gT_o/v_g^2$	Physical effect	10^{-5} to 10^{-4}
20	γ	Transfer term	Physical effect	?

Table 3-3. DEFINITION OF NONDIMENSIONAL TERMS (Cont'd)

π	Symbol	Definition	Type	Value
21	*Sc*	D_{va}/V_g	Physical effect	≈ 5
22	*Q*	$qL_H^2/\rho_w v_w C_w T_o$	Physical effect	0 to $\approx$ 1
23	τ	$\kappa^{TM}/\rho_s C_s L_H^2$	Response (Time scale)	-
24	θ	$(T-T_o)/T_o$	Response (Temperature scale)	-
25	S	Liquid Saturation	Response	-
26	X	Mass fraction of water in liquid	Response	-
27	Y	Mass fraction of water in gas	Response	-

The equations expressing conservation of mass for the gas and conservatin of energy for the volume are developed similarly, but are not given here for the sake of brevity. The nondimensional parameters in the conservation of gas equation are the same as for the conservation of water equation. The nondimensional form of conservation of energy is:

$$\frac{d}{d\tau}\iiint\left[\frac{(1-\phi)\bar{C}_s\bar{P}_s}{Pr}\right]\theta d\bar{V} + \frac{d}{d\tau}\iiint\left[\frac{XS+\bar{\rho}Y(1-S)}{Pr}\right]\phi\theta d\bar{V} +$$
$$\frac{d}{d\tau}\iiint\left[\frac{(1-X)S+\bar{\rho}(1-Y)(1-S)}{Pr}\right]\bar{C}_v\phi\theta d\bar{V} + \frac{d}{d\tau}\iiint\left[\frac{\bar{\rho}Y(1-S)}{Pr}\right]\theta U d\bar{V} =$$
$$\iint\left\{Xk_{Rw}Ca\theta\left[\left(\frac{dP_c}{dS}\right)\bar{\nabla}S + Si\bar{\nabla}\theta - \frac{1}{D}\bar{\nabla}D + Bo(1-\bar{\rho})k\right]\right\}\cdot n d\bar{A} +$$
$$\iint Yk_{Rg}GrCa(\theta+H)\theta k\cdot n d\bar{A} - \iint\left(\frac{1}{Pr}\right)(\theta+H)\bar{\nabla}Y\cdot n d\bar{A} +$$
$$\iint(1-X)k_{Rg}Ca\bar{C}_p\theta\left[\left(\frac{dP_c}{dS}\right)\bar{\nabla}S + Si\bar{\nabla}\theta - \frac{1}{D}\bar{\nabla}D + Bo(1-\bar{\rho})k\right]\cdot n d\bar{A} +$$
$$\iint(1-Y)k_{Rg}\beta_g\bar{C}_p\theta^2 k\cdot \mathbf{n} d\bar{A} + \iint\left(\frac{\bar{C}_p\theta}{Sc}\right)\bar{\nabla}Y\cdot \mathbf{n} d\bar{A} + \iiint Q d\bar{V} \ . \qquad (3\text{-}6)$$

Altogether, the nondimensional equations involve 27 nondimensional parameters. Eleven of these parameters are ratios of various physical effects which largely govern how the matrix-

volume responds to changes in boundary conditions or heating rates. The objective of this study is to determine the relative importance of each of these parameters.

3.4.4. Selection Criteria for the Pi Terms

As part of the initial assessment, the 27 pi terms were evaluated to identify those terms that, at least during this preliminary assessment, merit further evaluation. The parameters that comprise the pi terms have been assigned values representative of the physical characteristics of the laboratory-scale, separate-effects, experiments. The numerical magnitude of the pi terms were calculated using the assigned parameter values. Generally, a very large or very small pi term indicates that one of the other of the two effects in the ratio that forms the term is unimportant. Pi terms were selected for further examination based on physical reasoning and the observed results of the preliminary separate effects tests, in addition to the numerical magnitude of the terms.

Using these criteria, the third and the tenth through the eighteenth pi terms were chosen. Investigation of the third pi term (porosity) was not felt to be needed, as it is already known to be an important parameter. Investigation of the tenth and eleventh pi terms (involving the latent heats of vaporization of the liquid) was also not conducted for this paper, since the separate-effects experiments did not explore these phenomena.

A total of five pi terms, therefore, were selected for additional evaluation. The physical meanings of these five pi terms are as follows: (1) π_{15} is the ratio of capillary forces to viscous forces; (2) π_{16} is a modified form of the Prandtl number, which is the ratio of viscous diffusion to thermal diffusion; (3) π_{17} is the ratio of the change of capillary pressure to the change in saturation; (4) π_{18} is the change in capillary pressure with temperature; and (5) π_{21} is the Schmidt number, which is the ratio of mass diffusion to viscous diffusion.

3.4.5. Evaluation of Pi Terms

The influence of each pi term was investigated separately by increasing and decreasing each pi term by 25 percent relative to its nominal value, while holding all the other important pi terms constant. The effect of variations in the input values of the five pi terms was evaluated using a numerical model called TOUGH (Pruess, 1987). TOUGH calculates the flow of air and water through nonisothermal fractured porous media. In each simulation, the input parameters, except for the perturbed variable, were assigned values from a nominal case. The nominal case was taken to be representative of one of the separate effects laboratory experiments.

One parameter in each of the five pi terms was varied by 25 percent to vary the value of the pi term. For example, $\pi_{15}=\sigma k/d_{opw}v_w^2$ was varied by changing the shape factor c that relates the intrinsic permeability k to the pore size d_o, i.e., $k=cd_o^2$. By changing c, π_{15} could be varied; and none of the other pi terms was altered. Unfortunately, not all of the pi

terms could be treated in such a straightforward manner because the TOUGH code is written in such a way that many of the parameters in the pi terms do not appear in the code. For that reason, π_{18}, for example, could not be varied simply by varying $d\sigma/Dt$, although if it could then π_{18} could have been varied without altering the value of any other pi term. Instead, a more complicated method was used. The empirical function used in our application of the code to relate the capillary pressure P_{cap} to the saturation S was:

$$P_{cap} = -P_o \left[\frac{1}{S^{\frac{1}{\lambda}}} - 1 \right]^{1-\lambda} \tag{3-7}$$

where P_o and λ are parameters to be specified. The baseline values used in the study were: S=0.8; P_o=1.344 E 6; and λ=0.759. By choosing other appropriate values for P_o and λ, P_{cap} can be varied while holding dP_{cap}/PS constant, or dP_{cap}/dS can be varied while holding constant, for a saturation 0.8; this allowed us to vary both of the capillary pressure terms π_{17} and π_{18} individually while holding all other pi terms constant. Of course, if the saturation level at a point changed significantly from its initial value of 0.8, many of the pi terms appropriate to that location deviated from their nominal values; but this procedure still allowed investigation of the influence of the pi terms separately.

Numerical simulations were performed using TOUGH to determine the magnitude of change caused by variation of each pi term while holding the input values of all other pi terms constant. The computed values for gas saturation at a point in the model near the fracture were plotted against time for each simulation. The selected point was near the imposed fracture so that gas saturation values at a location of thermohydrological interest would be observed.

The computed gas saturation values from the simulations for the five cases for each pi term are illustrated in Figures 3-2 through 3-6. Also illustrated in each figure for comparison is a plot of gas saturation against time for the nominal case.

3.4.6. Discussion of the Results of Dimensional Analysis

Evaluation of the sensitivity of the flow regime to changes in the values of the pi terms has yielded a range in results. Pi terms that result in significant changes in the flow regime identifies those parameters that require further evaluation when using results at one scale to imply behavior at another scale. Examination of the results reveals that the flow regime is relatively insensitive to variation in two of the pi terms, π_{15} (Figure 3-2) and π_{16} (Figure 3-3), moderately sensitive to one of the pi terms, π_{21} (Figure 3-6), and highly sensitive to the other two terms, π_{17} (Figure 3-4) and π_{18} (Figure 3-5). These results indicate that parameters that constitute π_{15} and π_{16} can be varied by moderate amounts (25 percent) without adversely affecting the flow field. Of importance to note is that although a 25-percent change in fluid density is significant, a 25-percent change in permeability is not. Changes in permeability values of several orders of magnitude over small distances are commonly encountered in field situations.

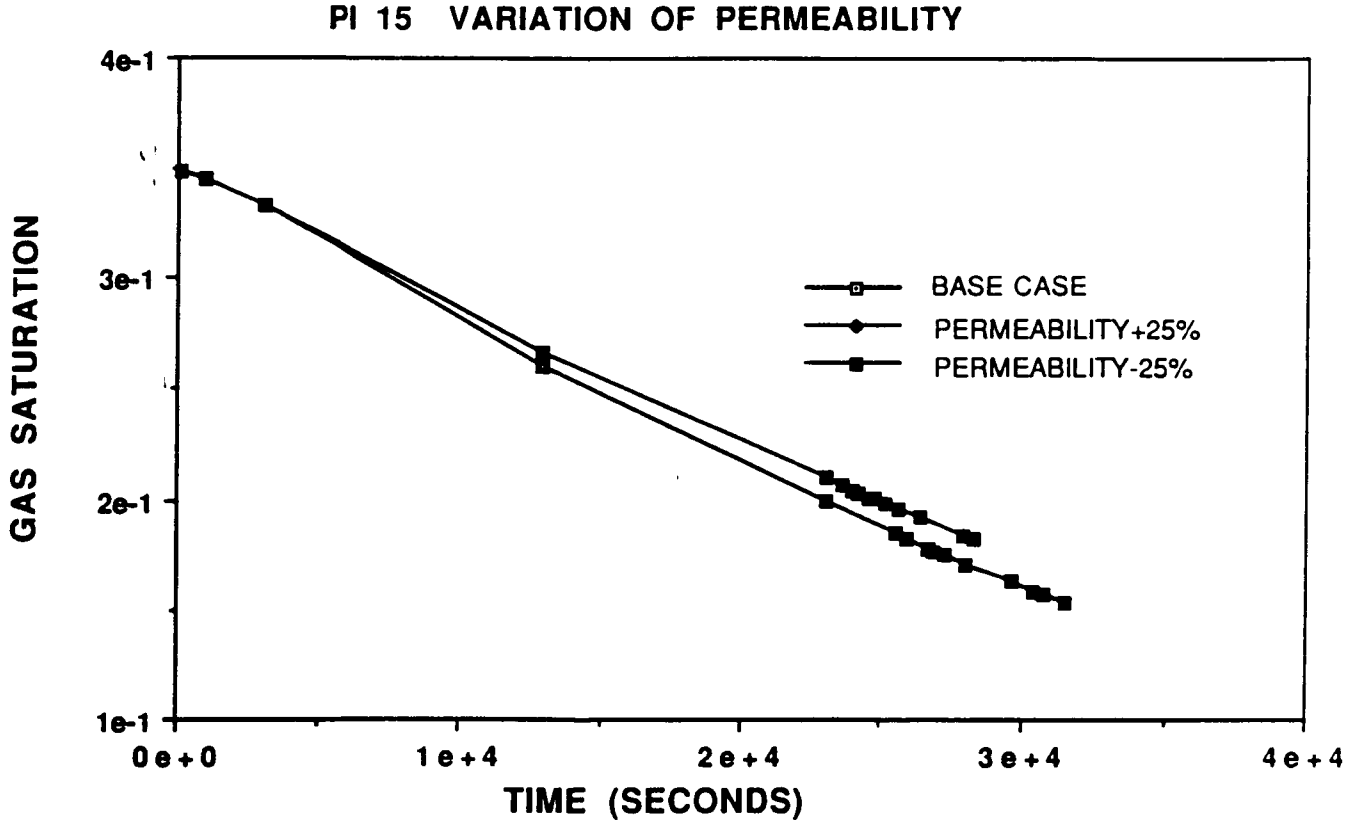

Figure 3-2. Plot of gas saturation numerically calculated vs time using the TOUGH code at a grid point near a simulated fracture. Pi term 15 was varied by changing the input value of permeability by 25 percent while keeping all other input values the same. Gas saturation for simulations with nominal input values is included for comparison.

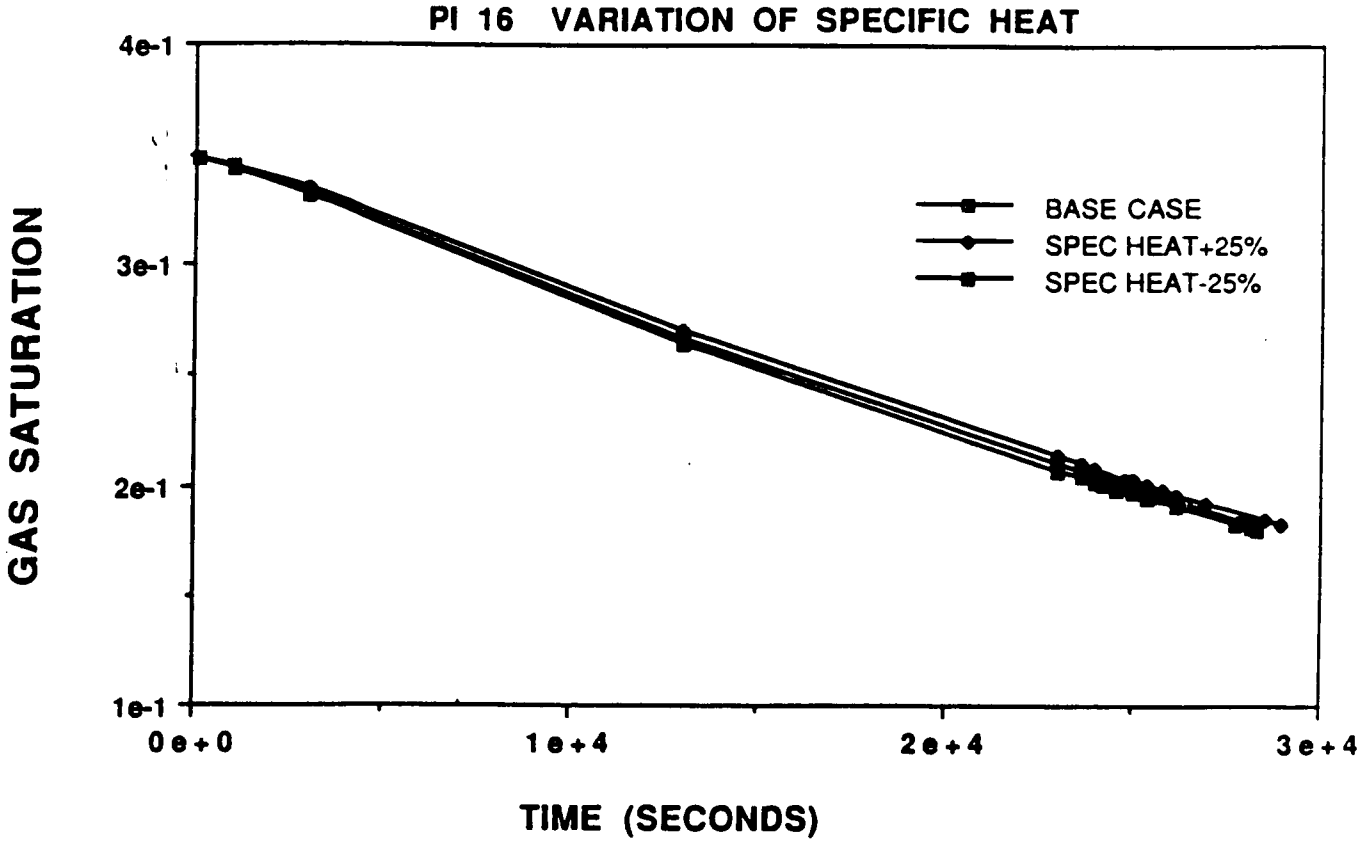

Figure 3-3. Plot of gas saturation numerically calculated vs time using the TOUGH code at a grid point near a simulated fracture. Pi term 16 was varied by changing the input value of specific heat by 15 percent while keeping all other input values the same. Gas saturation for simulations with nominal input values is included for comparison.

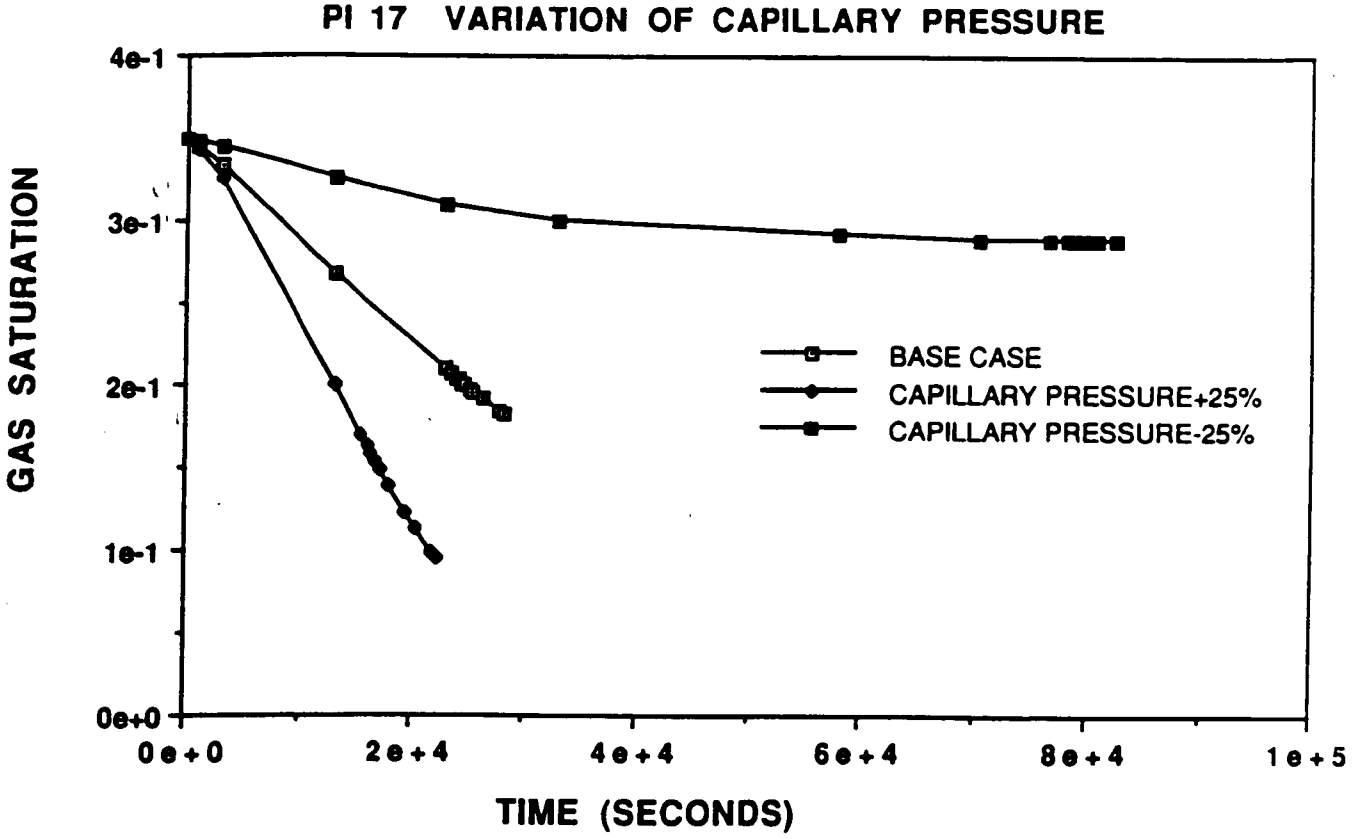

Figure 3-4. Plot of gas saturation numerically calculated vs time using the TOUGH code at a grid point near a simulated fracture. Pi term 17 was varied by changing the input value of capillary pressure by 25 percent while keeping all other input values the same. Gas saturation for simulations with nominal input values is included for comparison.

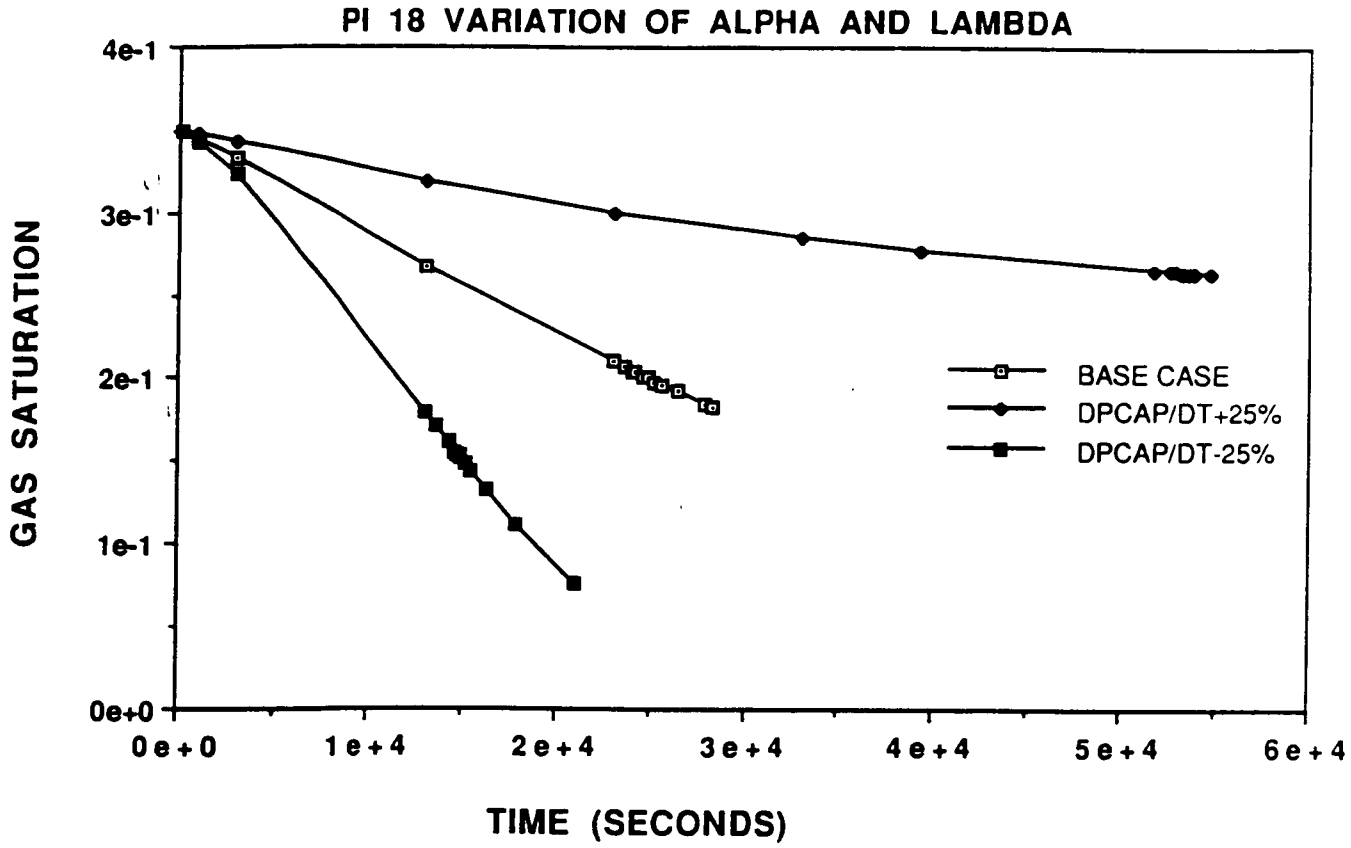

Figure 3-5. Plot of gas saturation numerically calculated vs time using the TOUGH code at a grid point near a simulated fracture. Pi term 18 was varied by changing the input value of the fracture hydraulic characteristics, alpha and lambda, by 25 percent while keeping all other input values the same. Gas saturation for simulations with nominal input values is included for comparison.

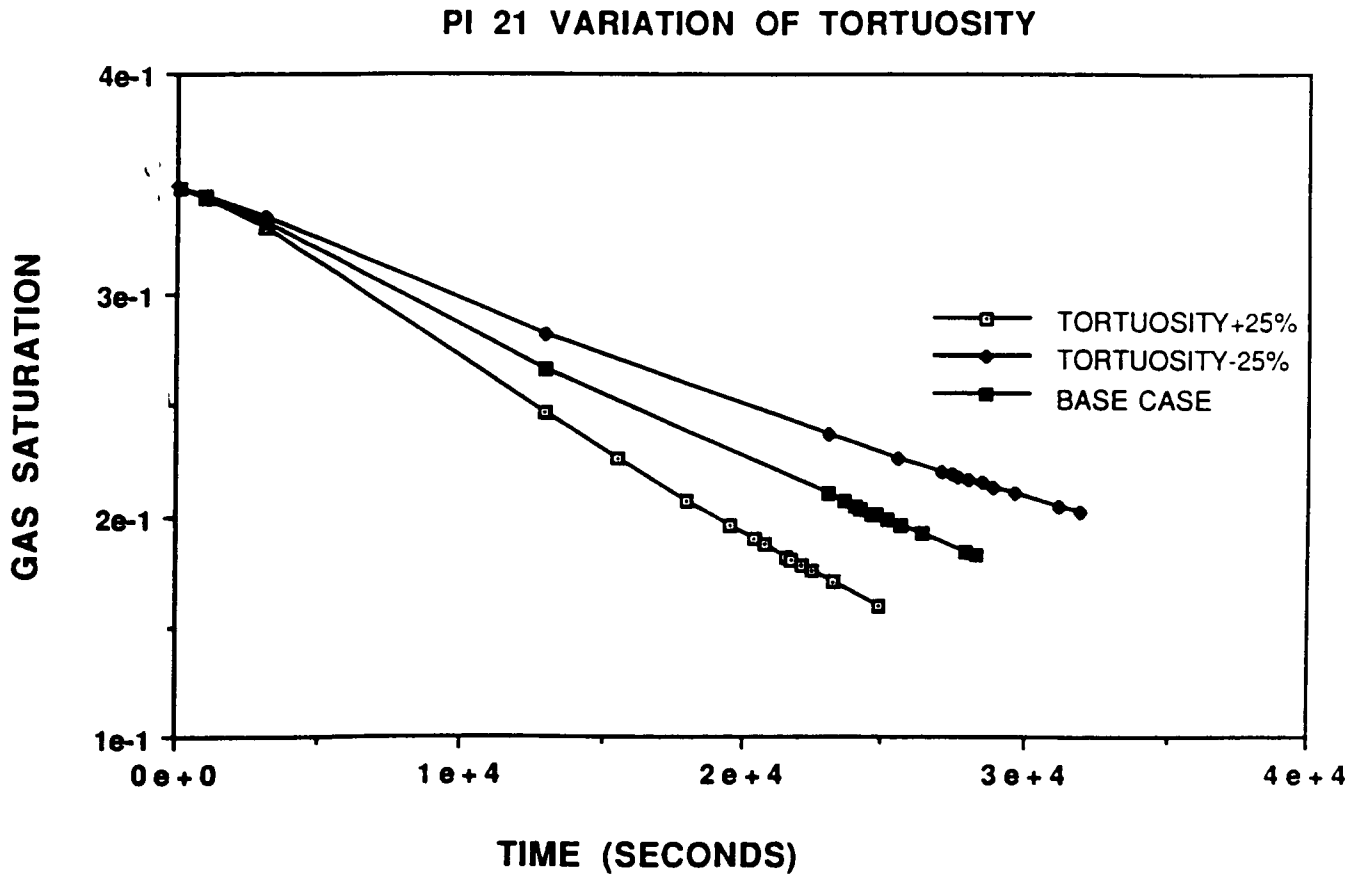

Figure 3-6. Plot of gas saturation numerically calculated versus time using the TOUGH code at a grid point near a simulated fracture. Pi term 21 was varied by changing the input value of tortuosity by 25 percent while keeping all other input values the same. Gas saturation for simulations with nominal input values is included for comparison.

Variation of the parameters in π_{17} and π_{18}, however, results in large changes to the flow regime. Both of these pi terms are associated with liquid surface tension and capillary pressure which, in turn, are related to moisture content and the unsaturated permeability. The results of these two analyses further illustrates the difficulties associated with the nonlinearity of flow through unsaturated, fractured porous media.

The results of the dimensional analysis presented in this report has been submitted to the ASME Symposium on Two-Phase Flow through Porous Media. The symposium is scheduled for December 1991.

3.5. REFERENCES

Evans, D. D. 1983. *Unsaturated Flow and Transport Through Fractured Rock - Related to High-Level Waste Repositories*. Final Report - Phase 1. NUREG/CR-3206. Washington, D.C.: NRC.

Pruess, K., R.C. Schroeder, P.A. Witherspoon, and J.M. Zerzan. 1979. *SHAFT 78-A Two-Phase Multidimensional Computer Program for Geothermal Reservoir Simulation*. Lawrence Berkeley Laboratory (LBL). LBL-8264. Berkeley, California: LBL.

Pruess, K. 1987. *TOUGH User's Guide*. NUREG/CR-4645. Berkeley, California: LBL.

Updegraff, C.D., C.E. Lee, and D.P. Gallegos. 1991. *DCM3D: A Dual-Continuum, Three-Dimensional, Ground-Water Flow Code for Unsaturated, Fractured, Porous Media*. NUREG/CR-5536. Washington, D. C.: NRC.

4. SEISMIC ROCK MECHANICS

by Simon M. Hsiung and Asadul H. Chowdhury

Investigators: Mikko P. Ahola (CNWRA), Asadul H. Chowdhury (CNWRA), Jaak J. Daemen (University of Nevada), Roger Hart (ITASCA), Simon H. Hsiung (CNWRA), and Daniel D. Kana (SwRI)

4.1. TECHNICAL OBJECTIVES

Six specific objectives have been identified for the Seismic Rock Mechanics Research Project. These are:

(1) Develop a good understanding of the information currently available about seismic effects on underground structures.

(2) Assess, by conceptual models and experimental studies, the capabilities and limitations of rock-joint models and computer codes currently in use.

(3) Demonstrate by laboratory model studies and instrumented field studies the degree of accuracy (validation) for the rock-joint models and computer codes used for seismic analysis in a tuff medium.

(4) Assess by instrumented field studies the significance of seismic pumping and to demonstrate the degree of validation for the rock-joint models and computer codes for simulation of seismic effects on groundwater hydrology.

(5) Identify and assess the key seismic-related parameters that are applicable to the Yucca Mountain site.

(6) Generate technical data for preparing licensing-related positions as they relate to the effect of seismic action on the underground repository in a tuff medium.

The objectives are addressed in the following eight tasks.

(1) Task 1 - Focused Literature Search

(2) Task 2 - Laboratory Characterization of Jointed Rock

(3) Task 3 - Assessment of Analytical Models/Computer Codes

(4) Task 4 - Rock Dynamics Laboratory and Field Studies and Code Validation

(5) Task 5 - Groundwater Hydrology Field Studies and Code Validation

(6) Task 6 - Yucca Mountain Scoping Analysis

(7) Task 7 - Technical Report

(8) Task 8 - Quarterly Research Report

The second, third, fourth, and fifth objectives were worked on during this reporting period. Specific work conducted included analysis of test data from three direct joint shear tests, and laboratory testing of welded tuff material, and instrumented field studies at the Lucky Friday Mine, Mullan, Idaho for (1) seismic effects on underground openings and (2) seismic effects on the geohydrologic regime.

4.2. LABORATORY INVESTIGATION OF ROCK-JOINT BEHAVIOR

4.2.1. Pseudostatic Rock-Joint Behavior Analysis

Three pseudostatic direct shear tests of Apache Leap tuff rock joint were conducted using the dynamic shear test apparatus developed by Kana et al. (1990). The tests consisted of repeated cycles of normal loading/unloading of the joint surface to determine the normal deformability. This was followed by a series of direct shear tests under various applied normal loadings to study the shear deformability of the joint surface. Data obtained from the tests were analyzed during this reporting period and preliminary results of the analysis are presented in the following sections. Data measuring devices such as load cells, vertical proximity eddy-current transducers, and linear variable differential transformers were calibrated according to the corresponding standards before the tests were conducted (for detail, please see the report prepared by Kana et al. 1990).

4.2.1.1. Normal Deformation Response of Joint

Five normal loading/unloading cycles were conducted on each sample to determine the normal stress versus normal deformation response. In calculating the applied normal stress, the individual loads applied by the three vertical actuators were summed, and the resultant load was divided by the surface area of the specimen to determine the average joint normal stress. No attempt was made to take account of any nonuniformity in the distribution of normal stress. Similarly, in determining the joint closure under applied normal loading and during joint shear, the average vertical compression (dilation) of the joint was calculated from three measurements of vertical displacement. These vertical measurements were taken directly across the rock joint, so that no correction had to be made for deformation of the intact specimen or the grout.

The response of the natural joint to a series of cyclical normal loadings is shown in Figure 4-1, in which the joint closure is plotted against the applied normal stress. Each of the cycles has been normalized to zero by subtracting the initial reading at the start of each load cycle. The third and fourth cycles are not shown for clarity. Due to

the large surface area of the sample and the capacity of the vertical actuators, it was only possible to obtain a maximum normal stress of 8 MPa (1,160 psi). According to the literature on experimental testing of rock joints, usually much higher normal stresses are applied to assure that the maximum asymptotic closure has been reached. It is observed from Figure 4-1 that complete closure is apparently not achieved; however, an asymptotic approach is suggested. An important aspect of the normal closure behavior is the hysteresis and large permanent set seen in the first cycle. Subsequent cycles show much less hysteresis and permanent set, with the normal stiffness (slope) increasing much more rapidly with increasing stress. By the fourth or fifth cycle, very little hysteresis remains, and the joint behaves more or less elastically. The normal stress versus closure response shown in Figure 4-1 is similar to that obtained by Bandis et al. (1983) for fresh to moderately weathered joint surfaces.

Figure 4-2 shows the results of the last loading cycle for the three experimental tests. Substantial differences for the relation between normal stress and closure among the three test results were observed. The maximum closure is the smallest for Test No. 1, about 0.05 mm (2×10^{-3} inches), and the largest is for Test No. 3, about 0.15 mm 6×10^{-3} inches). This observation indicates that the rock joint specimen for Test No. 1 is considerably stiffer than that for Test No. 3. No correlation was found between this observation and the basic intact rock material properties such as uniaxial compressive strengths and Young's moduli, which were determined by using the cores extracted from near the rock joints. The difference for the joint normal stiffnesses for the three tests may be related to the weathering conditions of the joints. The weathering condition of each individual rock joint specimen will be evaluated.

The results of the three experimental tests on joint normal loading were compared with the joint closure model proposed by Bandis et al. (1983), which is one of the empirical models under investigation. This closure model incorporates hyperbolic loading and unloading curves, relating the effective normal stress (σ_n) and joint closure (ΔV_j) as

$$\sigma_n = \frac{\Delta V_j}{a - b\Delta V_j} \tag{4-1}$$

where a and b are empirical constants. Figure 4-2 shows the results of fitting the hyperbolic relation given in Eqn. (4-1) to the normal loading curves for cycle 5 of the three tests. The results show that the Barton-Bandis model fits the data very well for normal stresses greater than approximately 2.0 MPa (290 psi). For lower normal stresses, however, the Barton-Bandis model appears to underestimate the joint closure. The values of the constants a and b for the three tests were determined to be:

Test No. 1: $a = 0.0199$ $b = 0.2605$
Test No. 2: $a = 0.03644$ $b = 0.3445$
Test No. 3: $a = 0.0960$ $b = 0.5313$

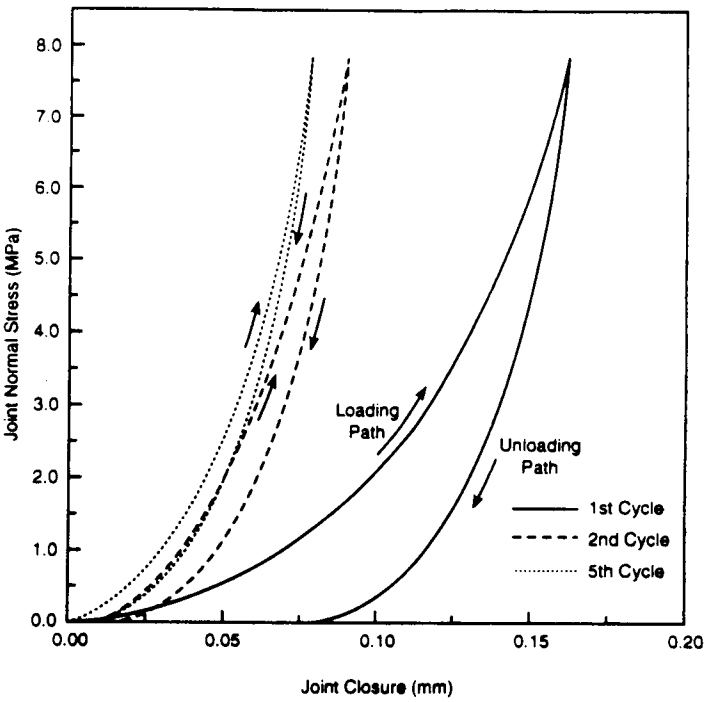

Figure 4-1. Normal stress vs. closure relationship for the welded tuff joint under repeated normal load cycles

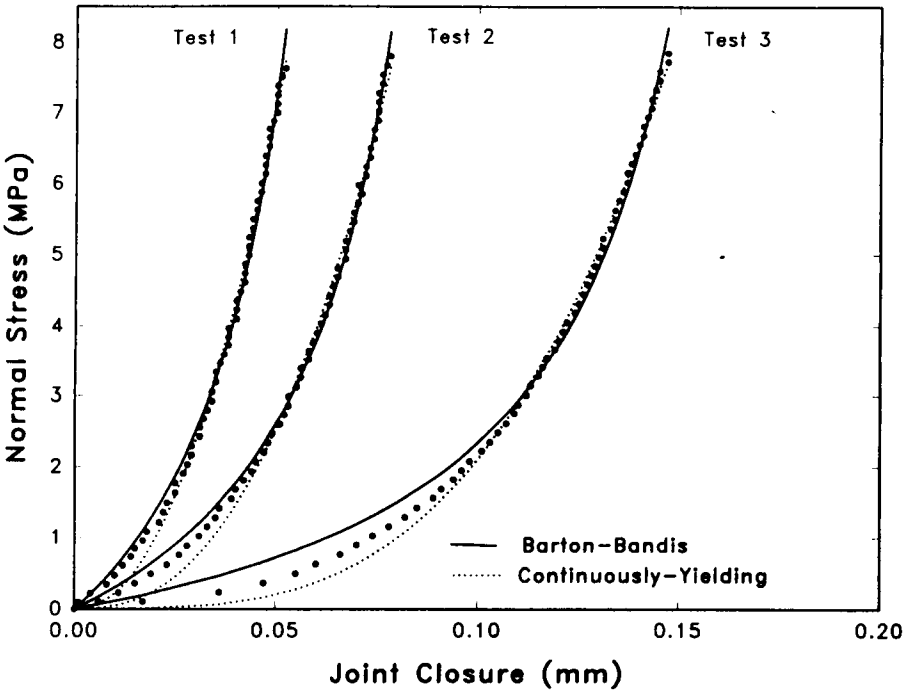

Figure 4-2. Comparison of the Barton-Bandis and continuously-yielding joint closure models with the experimental data obtained from normal load cycle 5

Bandis et al. (1983) also showed that the initial normal stiffness (K_{ni}) on the normal stress versus normal displacement curve is equal to the inverse of the constant a in Eqn. (4-1), and the maximum possible closure (V_m) is defined by the vertical asymptote a/b for the hyperbolic curves shown in Figure 4-2. Table 4-1 lists the initial normal stiffnesses and maximum closures for the fifth cycle predicted using the Barton-Bandis model and reached from the experimental test for all three tests.

Another model under consideration for simulating the normal deformability of rock joints is the continuous yielding model. This model is written in terms of a relation between the normal stiffness and normal stress as

$$K_n = a_n \sigma_n^{e_n} \tag{4-2}$$

where a_n, and e_n are constants. This formulation is different from the Barton-Bandis model, which can be fit directly to the normal stress (σ_n) versus normal closure (ΔV_j) data obtained from the experimental test to determine the constants in Eqn. (4-1). In order to determine the constants a_n and e_n from Eqn. (4-2) for the continuously yielding model, one would first have to calculate the normal stiffness from the slope between each pair of data points as plotted in Figure 4-2. Equation (4-2) could then be linearized by plotting log (K_n) versus log (σ_n), and the constants a_n and e_n determined by a linear regression. However, the results show considerable fluctuation in the normal stiffness when calculated between the individual data points. This can be observed from the discontinuous nature of the slopes between the data points plotted in Figure 4-2, and is most likely due to the roughness of the joint surface. Also, the data points in Figure 4-2 show that in some instances at the higher normal stresses, several increments in normal stress occur before any further incremental displacement takes place, requiring further approximations with regard to calculating stiffnesses between the data points. As a result, a different approach was taken. The normal stiffness in Eqn. (4-2) can be defined as

$$K_n = \frac{d\sigma_n}{du_n} \tag{4-3}$$

in which u_n is the same as ΔV_j in Eqn. (4-1) for the joint closure. Substituting this relation into Eqn. (4-2) for K_n and integrating, one obtains an equation for σ_n in terms of u_n as follows:

$$\sigma_n = \left[a_n(1-e_n)u_n\right]^{1/(1-e_n)} \tag{4-4}$$

where the constant of integration is zero if all the normal stress versus closure curves are adjusted to begin with zero. Equation (4-4) can now be fit to the normal stress versus closure

Table 4-1. PREDICTED AND CALCULATED INITIAL NORMAL STIFFNESSES AND MAXIMUM POSSIBLE CLOSURE

Test No.	Barton-Bandis		Calculated	
	Initial Normal Stiffness (MPa/mm)	Maximum Closure (mm)	Initial Normal Stiffness (MPa/mm)	Maximum Closure (mm)
1	50.3	0.076	95.0	0.052
2	27.4	0.106	17.5	0.078
3	10.4	0.181	6.2	0.147

data obtained from the experimental test. Equation (4-4) is also in a form that can be compared directly to the Barton-Bandis joint closure model. Figure 4-2 shows the results of fitting the relation for the continuously yielding model as given by Eqn. (4-4) to the normal loading curves for cycle 5 of the three tests. As with the Barton-Bandis model, the continuously yielding model fits the data very well for normal stresses greater than approximately 2.0 MPa (290 psi). However, for the lower normal loads, the continuously yielding model appears to somewhat overestimate the joint closure. The values of the empirical constants a_n and e_n for the last cycle of the three tests were determined to be:

Test No. 1: $a_n = 107.1$ $e_n = 0.5377$
Test No. 2: $a_n = 72.24$ $e_n = 0.598$
Test No. 3: $a_n = 42.04$ $e_n = 0.7033$

4.2.1.2. Shear Deformation Response of Joint

For the pseudostatic direct shear tests, the basic properties sought from the tests are the shear deformation characteristics, and the limiting shear strength as a function of normal stress. Important joint properties such as the dilatancy under shear deformation and the peak and residual strength characteristics are defined in terms of these components of a rock joint model.

Direct shear testing of the first three samples was designed so that the first shear cycle on the "fresh" joint was conducted under different applied normal stresses, namely 0.5 MPa (72.5 psi), 1.0 MPa (145 psi), and 2.0 MPa (290 psi). Subsequent shear cycles were conducted under successively higher normal stresses. The top box was sheared approximately 5.0 cm (2 inches) under controlled displacement, followed by shearing

in the reverse direction back to the original starting position. At that point, the next higher normal stress was applied, and the shear cycle was repeated. Figure 4-3 shows a plot of the shear stress versus shear displacement for the second test, in which the first cycle was initiated under an applied normal stress of 1.0 MPa (145 psi). For the first cycle, a peak shear stress of 1.44 Mpa (209 psi) is reached, followed by a residual shear stress of approximately 1.0 MPa (145 psi). Subsequent cycles show no peak behavior. Figure 4-3 shows that the pre-peak shear stiffness (slope) for the first cycle is somewhat higher than that for the second cycle under an applied loading of 2.0 MPa (290 psi). The average residual friction angle obtained from testing the first three welded tuff samples was calculated to be 40.5 degrees.

The continuously yielding model assumes a relation for the joint shear stiffness similar to that for the normal stiffness given in Eqn. (4-2). This relation can be written as

$$K_s = a_s \sigma_n^{e_s} \tag{4-5}$$

where a_s and e_s are again empirical constants. In this equation σ_n is the applied normal stress, and K_s is the shear stiffness prior to yielding of the joint. To be consistent, it was decided to take the slope of the shear stress versus shear displacement curves midway between the origin and the initiation of yielding, to determine the shear stiffness for each of the various applied normal stresses. The calculated shear stiffnesses versus applied normal stress for the residual shear curves were plotted on a log-log scale. Results from the first two tested samples showed a reasonably linear fit to Eqn. (4-5). Data from the third test, however, showed much higher shear stiffnesses prior to yielding for the same applied normal stresses. It needs to be determined whether the joint roughness is significantly different between the samples. In order to make this determination, joint roughness profiles were taken before and again after shear testing. One would also want to try to compare the results from the initial shear cycle for each of the samples and determine if there is a correlation with Eqn. (4-5). At this time, however, there are only three data points and further tests are needed to make any definite conclusions.

During the first two tests, the joint closure (dilation) was measured from the average of the three displacement probes mounted to the rock surface in the 5.0 cm (1.97 inches) gap between the top and bottom shear boxes. However, these vertical displacement probes had a total range of only 2.0 mm (0.08 inch). Due to the roughness of the joint surface, especially during the first shear cycle, these probes were not able to measure the complete normal displacement response of the joint due to direct shearing. For the third test, three additional probes of the same type but with a considerably larger displacement range were used. These probes had to be mounted to the outside of the steel shear boxes. It was observed that once the normal stress was applied, subsequent closure (dilation) measured by the larger probes as a result of direct shear cycling compared very well with the initial data obtained from the smaller displacement probes.

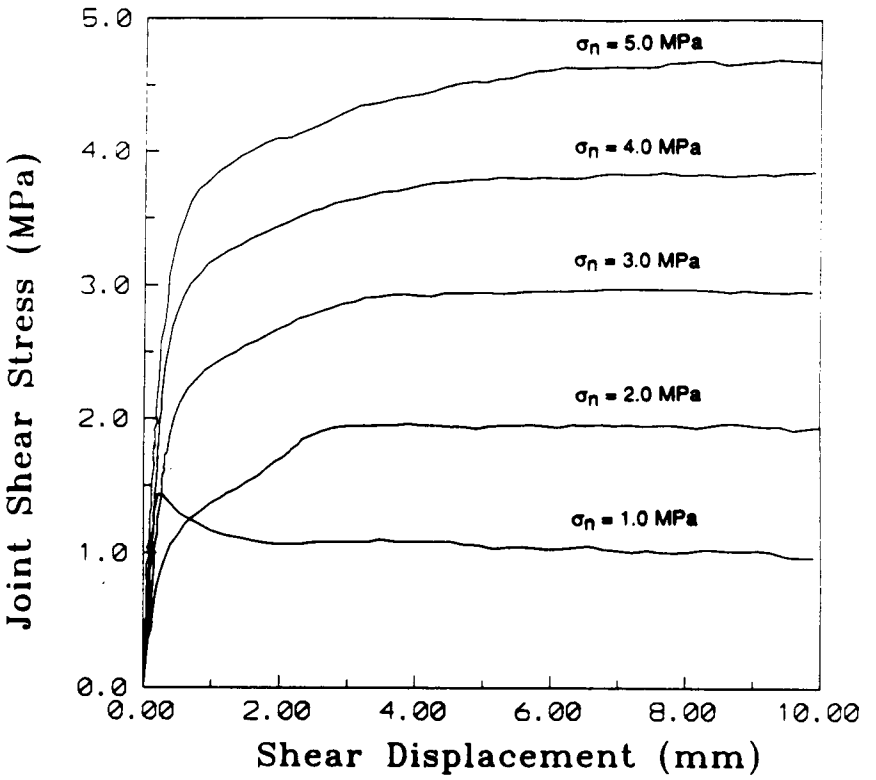

Figure 4-3. Shear stress vs. shear displacement relationship at various normal stress

Plots of the complete joint normal displacement versus shear displacement measured by the large vertical displacement probes are presented in Figure 4-4 for the third test. The first shear cycle on the fresh joint surface was conducted under a normal stress of 2 MPa (290 psi). For applied normal stresses of 2.0 MPa (290 psi) and 3.0 MPa (435 psi), the slopes of the joint normal deformation versus shear displacement plots are relatively steep, and dilation begins after only a small amount of shear displacement has taken place. For higher applied normal stresses of 4.0 MPa (580 psi) and 5.0 MPa (725 psi), the curves are much flatter and dilation does not occur until much larger shear displacements have taken place. The dilation versus shear displacement response shown in Figure 4-4 can be used to calculate an additional joint roughness parameter for the continuously yielding model. However, at this time, no further data reduction has been done.

4.2.1.3. Summary

Preliminary results obtained from the normal and direct shear test apparatus as part of the first phase of an extensive laboratory test program are presented. The normal stress versus closure response shows the large hysteresis and permanent set resulting from the first load cycle. Five normal loading/unloading cycles were determined sufficient to eliminate nearly all of the hysteresis, and reduce the joint response to more or less elastic

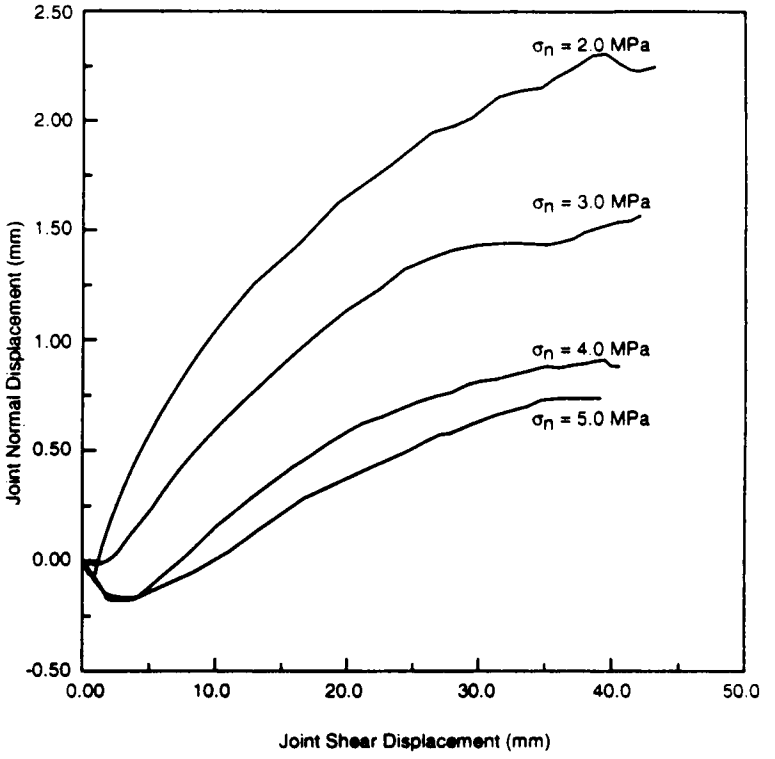

Figure 4-4. Joint normal displacement vs. shear displacement at various normal stress levels

behavior. Correlation of the experimental data with the Barton-Bandis closure model shows a slight underestimation of the joint closure at lower normal stresses, but good agreement at higher stresses. The continuously yielding joint closure model shows a slight overestimation of the joint closure at lower normal stress, but again good agreement at higher stresses. The shear stress versus shear displacement response varied somewhat between samples, apparently due to the joint roughness, making it difficult with the limited number of tests conducted to date to correlate results with the continuously yielding joint model. Further analysis of the variability of joint roughness between samples is necessary to determine how it affects the observed shear deformation response.

4.2.2. Specimen Preparation/Testing Activities

The types of tests to be performed for jointed rock characterization include (1) basic material properties tests, (2) jointed tuff interface characterization tests, (3) joint response for pseudostatic direct shear tests, (4) joint response for harmonic load tests, (5) joint response for ground shock load tests, and (6) joint response for earthquake load tests. The first three types of tests are aimed at determining basic tuff matrix and joint properties while the last three are performed for analyzing dynamic behavior of joints.

The activities of direct shear test specimen preparation and characterization of basic material properties, including uniaxial and triaxial compressive and tensile strengths, were completed. A total of 45 direct shear test specimens were prepared.

A total of 113 uniaxial specimens and 44 triaxial specimens have been tested in all. Among them, 55 uniaxial specimens and 19 triaxial specimens were tested during this reporting period. The test results are listed in Tables 4-2 and 4-3, respectively. For the test results obtained before this reporting period, the reader is referred to the annual research report of 1990 prepared by the CNWRA (1991).

Statistical analysis gives a mean uniaxial compressive strength of 23,413 psi (with a standard deviation of 3,780 psi) and a mean triaxial compressive strength of 28,923 psi (with a standard deviation of 3,864 psi) with 500 psi confining pressure, 35,400 psi (with a standard deviation of 3,001 psi) with 1,000 psi confining pressure, and 39,100 psi (with a standard deviation of 2,643 psi) with 1,500 psi confining pressure. Average values for Young's modulus and Poisson's ratio of the Apache Leap tuff are 5.6×10^6 psi (with a standard deviation of 0.5×10^6 psi) and 0.2 (with a standard deviation of 0.0287), respectively.

A total of 120 Brazilian disk tension specimens have been tested to determine tensile strength of the Apache Leap tuff, 50 of which were tested during this reporting period. The mean uniaxial tensile strength is 1,485 psi with a standard deviation of 321 psi. The results of the 50 tests conducted during this reporting period are given in Table 4-4.

4.3. SITE INVESTIGATION -- PORE WATER-PRESSURE MEASUREMENT

Site investigation at the Lucky Friday Mine is intended to monitor (1) the responses of excavations and their supports to repeated seismic events and (2) the change in water pressure in faults or other structures in the rock mass as a result of seismic loading. This site investigation program is aimed at generating a reliable data set of a particular site for evaluating analytical methods for simulation of the effects of seismic activities. The data collection for the responses of excavations and their supports subject to repeated mine seismic events is in progress. The results will be presented in future quarterly reports. The following discussion focuses on pore water pressure measurement.

To study the changes in water pressure in faults and other structural features in the rock mass as a result of seismic loading, these fault structures should be in close proximity to the seismicity and must be fully saturated with water. Therefore, the zones in which the fractures are sampled must be below the present workings which provide a draw-down to the surrounding groundwater. The faults must be pierced and packed off, with pressure measurements taken in the packed-off regions. One site at the 5700-level station, which is about 152 m (500 feet) below the two mechanical response instrumentation sites, was found suitable for the purpose of monitoring transient pore water pressure change along several fault structures.

Table 4-2. UNIAXIAL COMPRESSIVE STRENGTH, YOUNG'S MODULUS, AND POISSON'S RATIO OF APACHE LEAP TUFF

Specimen No.	Failure Stress (psi)	Young's Modulus E (psi x 10^6)	Poisson's Ratio ν
SRM9.2.3-U-1	23,100	5.2	0.20
SRM9.2.3-U-2	24,300	5.1	--
SRM9.3.4-U-1	16,400	6.4	--
SRM9.4.5-U-1	25,400	5.6	0.22
SRM9.4.5-U-2	22,800	4.9	0.28
SRM10.2.2-1-U-1	21,300	5.7	0.20
SRM10-2.2-3-U-4	25,000	5.5	0.17
SRM10.3.4-U-1	21,300	6.1	0.18
SRM11.1.1-U-1	16,600	4.5	0.21
SRM11.1.1-U-2	21,000	5.2	0.17
SRM11.1.2-U-1	24,000	5.4	0.19
SRM11.2.3-U-1	19,200	4.7	0.23
SRM11.2.3-U-2	25,400	5.2	0.17
SRM11.2.3-U-3	23,600	6.3	0.19
SRM11.3.4-U-1	25,200	5.7	0.19
SRM11.3.4-U-2	21,700	5.1	0.17
SRM12.1.1-1-U-1	24,900	5.2	0.18
SRM12.1.1-2-U-1	24,700	5.1	0.17
SRM12.1.1-2-U-2	22,600	5.1	0.17
SRM12.3.3-U-1	24,700	6.2	0.20
SRM12.3.3-U-2	21,900	5.3	0.24
SRM12.3.3-U-3	25,000	5.7	0.20
SRM13.1.2-U-1	24,300	5.6	0.17
SRM13.2.3-U-2	27,900	5.1	0.20

Table 4-2. UNIAXIAL COMPRESSIVE STRENGTH, YOUNG'S MODULUS, AND POISSON'S RATIO OF APACHE LEAP TUFF (Cont'd)

Specimen No.	Failure Stress (psi)	Young's Modulus E (psi x 10^6)	Poisson's Ratio ν
SRM13.3.4-U-3	27,100	5.3	0.18
SRM13.4.5-U-1	26,000	6.1	0.20
SRM13.4.5-U-2	25,400	5.7	0.17
SRM13.4.6-1-U-1	20,000	4.8	0.25
SRM15.2.5-U-1	25,100	5.4	0.18
SRM15.4.6-U-1	27,700	5.9	0.17
SRM15.4.6-U-2	24,000	6.6	0.19
SRM15.5.7-U-1	23,900	5.6	0.18
SRM15.5.7-U-2	26,400	5.4	0.20
SRM15.5.7-U-3	22,600	5.9	0.19
SRM16.3.3-U-1	26,400	5.7	0.17
SRM16.3.3-U-2	24,500	6.7	0.23
SRM17.3.4-U-1	20,600	5.3	0.20
SRM17.3.4-U-2	23,500	6.1	0.20
SRM19.1.1-U-1	24,630	5.3	0.18
SRM19.1.1-U-2	25,800	4.5	0.18
SRM20.1.1-U-1	29,100	5.1	0.22
SRM20.1.1-U-2	26,950	5.6	0.17
SRM20.2.2-U-1	26,400	4.8	0.19
SRM20.3.3-U-1	24,150	5.2	0.17
SRM20.3.3-U-2	24,800	5.2	0.17
SRM20.3.3-U-3	25,100	5.1	0.19
SRM20.4.5-U-1	21,640	4.9	0.20

Table 4-3. TRIAXIAL COMPRESSIVE STRENGTH FOR APACHE LEAP TUFF

Specimen No.	Confining Pressure (psi)	Failure Stress (psi)	Density (pcf)
SRM11.2.3-T-1	1,000	36,500	151
SRM12.1.1-1-T-1	500	31,200	154
SRM12.1.1-2-T-1	1,500	36,000	152
SRM12.3.3-T-1	500	28,500	151
SRM12.3.3-T-2	1,500	37,500	151
SRM13.1.2-T-1	500	17,000	151
SRM13.1.2-T-2	1,000	38,400	152
SRM13.4.5-T-1	1,500	41,200	151
SRM13.4.6-1-T-1	500	30,500	151
SRM15.2.3-T-1	500	30,400	151
SRM15.3.5-T-1	1,500	42,500	151
SRM15.4.6-T-1	1,500	35,900	150
SRM15.4.6-T-2	500	34,000	151
SRM15.5.7-T-1	500	33,300	151
SRM15.5.7-T-2	500	28,200	150
SRM16.2.2-T-1	1,500	34,500	151
SRM17.3.4-T-1	500	26,400	151
SRM19.1.1-T-1	500	26,400	150
SRM19.1.1-T-2	1,500	38,000	151

Table 4-4. RESULTS OF BRAZILIAN DISK TENSION TESTS OF APACHE LEAP TUFF

Specimen No.	Failure Stress (psi)	Specimen No.	Failure Stress (psi)
SRM11.1.1-B-1	2,200	SRM17.1.2-B-1	1,370
SRM11.1.1-B-2	1,260	SRM17.1.2-B-2	1,600
SRM11.1.2-B-1	1,410	SRM17.3.4-B-1	1,950
SRM11.1.2-B-2	1,560	SRM19.1.1-B-1	1,560
SRM11.2.3-B-1	1,700	SRM19.1.1-B-2	1,320
SRM11.2.3-B-2	1,310	SRM19.1.1-B-3	1,300
SRM11.3.4-B-1	2,140	SRM20.1.1-B-1	1,960
SRM11.3.4-B-2	1,500	SRM20.1.1-B-2	1,600
SRM12.1.1-1-B-1	1,490	SRM20.1.1-B-3	1,140
SRM12.1.1-1-B-2	1,740	SRM20.2.2-B-1	1,960
SRM12.1.1-2-B-1	1,530	SRM20.2.2-B-2	1,680
SRM12.3.3-B-1	1,590	SRM20.3.3-B-1	1,420
SRM12.3.3-B-2	1,300	SRM20.4.5-B-1	1,480
SRM13.1.2-B-1	1,320	SRM22.2.2-B-1	1,500
SRM13.1.2-B-2	1,480	SRM22.2.2-B-2	1,230
SRM13.4.5-B-1	1,374	SRM22.3.3-B-1	1,410
SRM13.4.5-B-2	1,465	SRM22.3.3-B-2	1,630
SRM15.3.5-B-1	1,594	SRM22.4.4-B-1	1,680
SRM15.3.5-B-1	1,400	SRM23.1.2-B-2	1,710
SRM15.4.6-B-1	1,730	SRM25.1.1-B-1	1,720
SRM15.4.6-B-2	1,270	SRM26.2.2-B-1	1,450
SRM15.5.7-B-1	1,440	SRM26.2.2-B-2	1,760
SRM15.5.7-B-2	1,890	SRM26.2.3-B-2	1,300
SRM16.3.3-B-1	1,130	SRM29.3.5-B-2	1,233

An NQ size hole (7.6 cm in diameter) was drilled at approximately 20° downward in a southerly direction from the 5700-level station. The hole was directed toward an intersection with the main and footwall split fault structures, as well as with the South Control fault. The total length of the drilling was 360 m (1,180 feet). A borehole survey conducted after the drilling was completed indicates a deviation of the drilled borehole from the projected location. The bottom of the borehole is about 8.95 m (29 feet) above and 34 m (111 feet) to the right (looking at the bottom of the borehole from the collar) of the projected location. These structures were intersected within about 310 m (1,017 feet) of drilling.

Core logging indicated that much of the borehole has few water-bearing fault structures. The first 183 m (600 feet) of drilling is not suitable for instrumentation due to the lack of faulting. Five fault and mineral vein structures were identified between 183 m (600 feet) and 360 m (1,180 feet) of the borehole as having potential for pore water pressure monitoring. These structures are located about 207 m (680 feet), 242 m (795 feet), 269 m (883 feet), 288 m (945 feet), and 307 m (1,006 feet) from the borehole collar.

Four of the five structures were selected for pore water pressure monitoring. The fracture structure at 269 m (883 feet) is relatively minor compared to the other structures and was excluded from instrumentation. The selected fault and vein structures were packed off using inflatable straddle packers. The straddle packers were placed in the relatively competent and intact rock zones so that they could be seated firmly against the borehole wall. The inflation pressure for the packers is set to be 2.76 MPa (400 psi) to account for hydrostatic water, expansion pressure for the packers to expand to the borehole size, and the pressure required to hold the packers in place. Figure 4-5 shows the locations of the packers and the zones where hydrologic water pressures are to be measured. Also shown in the figure are the selected structural features.

Initial piezometer measurement of water pressure at zone 1 is 2.59 MPa (375 psi), 2.48 MPa (360 psi) for zone 2, 2.14 MPa (310 psi) for zone 3, and 0.58 MPa (84.5 psi) for zone 4. The relatively low pressure in zone 4 is because of malfunctioning of the packer set. A 2.59 MPa (375 psi) water pressure is equivalent to 264 m (866 feet) of water head. Transfer tubing gage reading at the 5700-level is 1.66 MPa (240 psi) for both zones 1 and 2, and 1.38 MPa (200 psi) for zone 3. Taking into account the appropriate static water head, hydrologic water pressure at each specific packed-off zone can be calculated from the transfer tubing gage readings. The calculated water pressure for zone 1 is 2.63 MPa (382 psi), 2.59 MPa (376 psi) for zone 2, and 2.17 MPa (315 psi) for zone 3. The calculated water pressures are fairly close to the respective piezometer measurements. The data collection for pore water-pressure charge subject to repeated mine seismic events is in progress. The results will be presented in future quarterly reports.

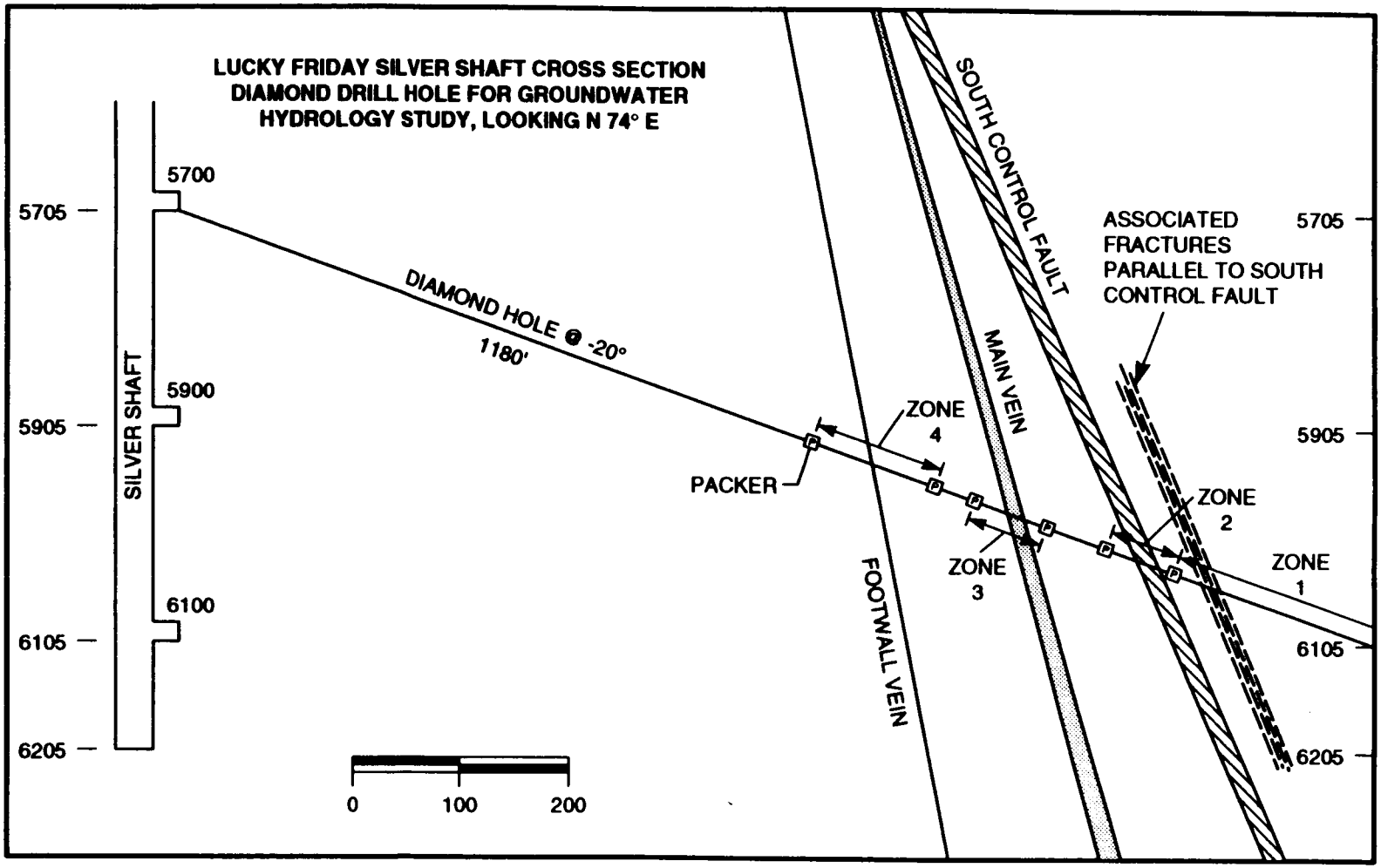

Figure 4-5. Lucky Friday silver shaft cross section of the drill hole showing zones packed off for water pressure monitoring (view looking N74°E)

4.4. REFERENCES

Bandis, S. C., A. C. Lumsden, and N. R. Barton. 1983. Fundamentals of Rock Joint Deformation. *Int. J. Rock Mech. Min. Sci. & Geomech. Abstr.* Pergamon Press 20: 249-268.

CNWRA. 1991. *Report on Research Activities for Calendar Year 1990.* CNWRA 90-01A. Center for Nuclear Waste Regulatory Analyses (CNWRA): 4-1 to 4-97. CNWRA, San Antonio, Texas.

Kana, D. D., D. C. Scheidt, B. H. G. Brady, A. H. Chowdhury, S. M. Hsiung, and B. W. Vanzant. 1990. *Development of a Rock Joint Dynamic Shear Test Apparatus.* CNWRA 90-005, Jan. 1990, Center for Nuclear Waste Regulatory Analyses (CNWRA): 1-27. CNWRA, San Antonio, Texas.

5. INTEGRATED WASTE PACKAGE EXPERIMENTS

by Gustavo Cragnolino and Narasi Sridhar

Investigators: Narasi Sridhar (CNWRA), Gustavo Cragnolino (CNWRA), and Walter Machowski (SwRI)

5.1. TECHNICAL OBJECTIVES

The overall technical objectives of the Integrated Waste Package Experiments (IWPE) Project are to:

(1) Develop a good understanding of the information currently available on metal corrosion and on other metal degradation processes.

(2) Assess the current status of Yucca Mountain Project (YMP) Waste-Package Programs.

(3) Conduct waste-package experiments to scope and study the key parameters affecting long-term material performance.

(4) Assess experimentally YMP selected waste-package materials and designs and provide independent evaluation for reasonable assurance of long-term performance.

(5) Facilitate a continuous technical integration support to NRC and the CNWRA in the area of waste package performance.

The objectives of the IWPE are planned to be accomplished under the following tasks, which are consistent with Revision 3 of the program plan:

(1) Task 1 - Corrosion, including Localized, Uniform, and Internal Corrosion

(2) Task 2 - Stress Corrosion Cracking

(3) Task 3 - Materials Stability

(4) Task 4 - Microbiologically Influenced Corrosion

(5) Task 5 - Other Degradation Modes

(6) Task 6 - Periodic Reporting

The current report focuses on work performed for Task 1. Literature reviews were performed in Tasks 2, 3, and 4. Test plans for Tasks 2 and 3 were approved, and experimental

programs will be initiated during the next reporting period. Studies on hydrogen absorption and embrittlement, conducted under Task 5, were completed at The Ohio State University and will be the subject of a topical report to be issued in the next reporting period.

5.2. TASK 1 - CORROSION OF CONTAINER MATERIALS

Activities and salient results in three subtasks within Task 1 are described in this section. These subtasks are:

- Task 1.1.1 - Review of Experimental Results from Other Programs Related to Localized Corrosion
- Task 1.1.3a - Pitting Variability Studies
- Task 1.1.3b - Full Factorial Tests

5.2.1. Review of Experimental Results Related to Localized Corrosion

During this reporting period, a critical review of the experimental results obtained by other laboratories involved in the study of HLW container materials continued. Additionally, literature outside this area but pertinent to localized corrosion of Fe-Ni-Cr-Mo and Cu-base alloys was reviewed with emphasis on test techniques and the effect of environmental factors on localized corrosion.

One technique of particular interest for long-term prediction is the crevice corrosion repassivation technique. This concept, an extension of the pitting repassivation/protection potential to crevice corrosion, was advanced by Tsujikawa and co-workers (Tsujikawa, 1982; Okayama, 1987a; Okayama, 1987b; Tamaki, 1990; Tsujikawa, 1990). Crevices were formed by bolting nuts made of the sample materials together with a gasket under preset torques. This electrochemical technique is essentially pseudo-potentiostatic and involves initiating crevice corrosion at a relatively high anodic potential for varying lengths of time followed by a stepwise decrease in potential until a potential is reached at which the current density decreases below 5μA. This potential is called the crevice corrosion repassivation potential. In some materials, the investigators used 50 μA as the threshold current. The experiments showed that the repassivation potential is relatively insensitive to the extent of prior crevice corrosion growth and is relatively constant with respect to the measurement time. These characteristics are important for assessing the performance of waste package container materials, since the crevice repassivation potential can be used as a bounding parameter.

A related approach is that of measuring the depassivation pH (Okayama, 1987b). In this case, no crevices are formed; but the samples are exposed to solutions that simulate the solutions inside a crevice. The mechanistic models of crevice corrosion predict that the solutions inside crevices in stainless steels will be higher in chloride content (as high as 6M), as required to attain electroneutrality, and lower in pH, as dictated by hydrolysis equilibria. Under these

increasingly severe conditions, the stainless steel will lose its passivity; and crevice corrosion will initiate. Hence, one method of assessing the resistance of a given alloy to crevice corrosion is to measure the pH of a concentrated chloride solution in which the alloy no longer exhibits passivity. The lower the pH of this solution, called the depassivation pH (pH_d), the more resistant the alloy is to crevice corrosion. Measurement of the depassivation pH under a variety of chloride concentrations and temperatures also can yield a parameter for use in mechanistic models of crevice corrosion enabling extrapolation of short-term laboratory data to long-term behavior. Okayama et al. have measured the pH_d for a wide variety of alloys, including alloy 825, at various chloride concentrations ranging from 0.3 to 20 percent (wt.) and at temperatures ranging from 20 to 80°C. The interesting conclusions include the relative independence of the pH_d on both the chloride content and temperature for a wide variety of alloys. These measurements need to be verified by further experiments. The effects of other anionic species, particularly nitrate and sulfate, on pH_d also need to be examined.

5.2.2. Further Experiments on Alloy 825

In a recent publication (Cragnolino, 1991), the results of investigations on the effect of environmental factors on localized corrosion of alloy 825 were discussed. In all these experiments, the bicarbonate concentration was maintained at a constant value of 85 ppm, whereas, the anions, chloride (6 and 1000 ppm), sulfate (20 and 1000 ppm), nitrate (10 and 1000 ppm), and fluoride (2 and 200 ppm), were varied. The pH was allowed to assume its natural value, which was typically about 8.2 at room temperature at the start of the test and about 9.4 at room temperature at the end of the test. In other studies (Beavers, 1990), bicarbonate has been reported to have no effect on the electrochemical parameters (pitting and repassivation potentials) related to localized corrosion, while pH has been reported to have a negative effect on the repassivation potential, E_{rp}. However, in the investigation of Beavers et al. (Beavers, 1990), the pH was adjusted using sulfuric acid, so the pH and bicarbonate concentration (as well as sulfate concentration) were not independent. Additional experiments, therefore, were undertaken at the CNWRA to explore the effects of bicarbonate and pH separately. It was also of interest to examine the effect of sulfate, since the previous experiments at the CNWRA, which were limited to 1000 ppm, concluded that sulfate did not have a significant effect on localized corrosion in contrast to literature findings for austenitic stainless steels (Smialowska, 1986).

5.2.2.1. Effect of Bicarbonate

The effect of bicarbonate concentration ranging from 85 to 2000 ppm was studied by adding various concentrations of $NaHCO_3$ to solutions containing 1000-ppm chloride, 20-ppm sulfate, 10-ppm nitrate, and 2-ppm fluoride. The solutions were allowed to attain their natural pH which, at room temperature, was about 8.3. At this pH, bicarbonate is the predominant dissolved carbonate species. The solution was deaerated with argon at 1 atm pressure. Due to exsolution of CO_2 during the test, the room temperature pH increased to 10.1. Post-test analysis of solutions, using the ASTM D513-88, Practice A procedure, indicates a small decrease in bicarbonate from the initial value. The results are shown in Table 5-1. The

localized corrosion index (LCI) was previously introduced to quantify the extent of localized corrosion by combining the electrochemical parameters and a visual rating (Cragnolino, 1991). It can be seen that bicarbonate does not have any effect on corrosion potential or pitting potential. However, the repassivation potential seems to be affected slightly. In previous studies, a standard deviation of 68 mV has been observed for repassivation potentials in this environment (Cragnolino, 1991). Hence, the statistical significance of the bicarbonate effect on repassivation potential is open to question. The addition of 2000 ppm bicarbonate results in a more positive repassivation potential, again indicating that the bicarbonate effect may not be really significant. Further tests are in progress.

5.2.2.2. Effect of pH

As mentioned before, the pH in these solutions is related to the bicarbonate concentration and the fugacity of CO_2 by the following equations (Stumm, 1981):

$$CO_2(g) + H_2O = H_2CO_3^*; \quad pK_{25C} = 1.5 \tag{5-1}$$

$$H_2CO_3^* = HCO_3^- + H^+; \quad pK_{25C} = 6.35 \tag{5-2}$$

Here, $H_2CO_3^*$ is used to indicate the combined concentration of H_2CO_3 and dissolved CO_2 in accordance with the notation used by Stumm and Morgan (Stumm, 1981).

Based on the above values of equilibrium constants, the calculated pH for a bicarbonate concentration of 85 ppm (1.39×10^{-3} M) and a fugacity of CO_2 gas of about 1 atm is 5.0. This was chosen as the lowest pH for the present study. The highest pH studied for this concentration of bicarbonate was a pH of 8.5 attained in equilibrium with atmospheric carbon dioxide fugacity, which is typically about 3×10^{-4} atm. The results of these tests are shown in Table 5-2 for alloy 825.

Table 5-2 shows that lowering the pH resulted in an increase in the localized corrosion index at the 1000-ppm chloride concentration. It can also be seen that the pitting potential, E_p, is only slightly lowered; but the repassivation potential, E_{rp}, is lowered considerably to the point where even a mildly oxidizing environment can sustain localized corrosion. However, it is difficult to judge from the sparse data whether lowering the pH resulted in lowering the chloride concentration at which localized corrosion begins to manifest itself in this test. The above results are somewhat at odds with literature (Smialowska, 1986) where pH within a range of about 3 to 9 has not been shown to affect localized corrosion parameters. It is possible that the discrepancy is due to the relatively low chloride concentration used in the present study. On the other hand, it is in agreement with the results of Beavers et al. (Beavers, 1990), who also found pH to lower E_{rp} and not affect E_p.

Table 5-1. THE EFFECT OF BICARBONATE ON LOCALIZED CORROSION OF ALLOY 825 IN CYCLIC POLARIZATION TESTS. SOLUTIONS: 1000 ppm CHLORIDE, 20 ppm SULFATE, 10 ppm NITRATE, AND 2 ppm FLUORIDE—ALL AS SODIUM SALTS. TEST TEMPERATURE: 95°C.

HCO_3 (ppm)	pH		E_{corr} (mV_{SCE})	E_p (mV_{SCE})	E_{rp} (mV_{SCE})	LCI = (E_p-E_{rp}) x Visual Rating
	Initial	Final				
85	8.1	9.4	-555	626	82	2176
1000	8.3	10.2	-512	657	-167	3296
2000	8.3	10.1	-537	660	-29	2756

Table 5-2. EFFECT OF pH (AT ROOM TEMPERATURE) ON LOCALIZED CORROSION OF ALLOY 825. SOLUTION: 1000 ppm CHLORIDE, 20 ppm SULFATE, 10 ppm NITRATE, 2 ppm FLUORIDE, 85 ppm BICARBONATE. TEMPERATURE = 95°C.

Chloride (ppm)	pH		E_{corr} (mV_{SCE})	E_p (mV_{SCE})	E_{rp} (mV_{SCE})	LCI = (E_p-E_{rp}) x Visual Index
	Initial	Final				
1000	8.1	9.4	-555	626	82	2176
1000	4.9	5.3	-507	586	-315	3604
6	8.4	9.5	-447	782	758	0
3.6	5.3	5.3	-472	926	878	0

5.2.2.3. *Effect of Sulfate*

In the factorial experiments reported before (Cragnolino, 1991) on alloy 825, sulfate did not appear to be a significant factor in localized corrosion. This is at variance with the well known inhibitive effect of sulfate. For example, Uhlig and Leckie (Leckie, 1966) determined that the addition of SO_4^{2-} above about 0.05M increased the E_p of a 18Cr-8Ni stainless steel in a 0.1M Cl^- solution. Rosenfeld and Maksimchuk (Rosenfeld, 1967) used a galvanostatic test and determined that, in a neutral solution, pit initiation on a 18Cr-8Ni stainless steel was prevented by a SO_4^{2-}/Cl^- molar ratio of 7. This ratio decreased with a decrease in pH. Brookes and Graham (Brookes, 1989) examined many ferritic stainless steels (low in Ni) and found that the inhibition due to sulfate in terms of an increase in E_p followed the relationship:

$$\text{Log } (Cl^-) = A \text{ Log } (SO_4^{2-}) + B \qquad (5\text{-}3)$$

where A and B are dependent on the alloy composition. For a Fe-18.5Cr-0.02Ni alloy, they found that A = 0.1 and B = -1.1. All these investigators attribute the inhibitive effect of sulfate to competitive adsorption with chloride and displacement of chloride by sulfate in the passive film. Kain (Kain, 1990) performed immersion crevice corrosion tests and found that sulfate inhibited crevice corrosion initiation but accelerated propagation. Because of the above findings, it was of interest to extend the previous experiments to higher sulfate concentrations. A 1000 ppm chloride solution was chosen, and sulfate concentrations ranging from 20 to 20,000 ppm (SO_4^{2-}/Cl^- (molar): 0.0074 - 7.4) were examined. The results are shown in Figures 5-1 and 5-2. As indicated in Figure 5-1, the polarization curve shows a considerable reduction in the hysteresis when 20,000 ppm sulfate is present in the solution. The test sample also show a considerable reduction in pits and crevice corrosion. The effect of sulfate is summarized in terms of the localized corrosion index (LCI) in Figure 5-2. The findings agree approximately with those of Rosenfeld (Rosenfeld, 1967).

5.2.3. Localized Corrosion Tests on Alloy C-22

Alloy C-22 has been chosen as the reference material for some of the corrosion studies at the Center. This is a Ni-base alloy with a nominal composition in weight percent of 22 percent Cr, 5 percent Fe, 13 percent Mo, and 3 percent W. Since this alloy possesses a high resistance to localized corrosion, it was examined by the same test methods as those used for alloy 825. The results are shown in Table 5-3.

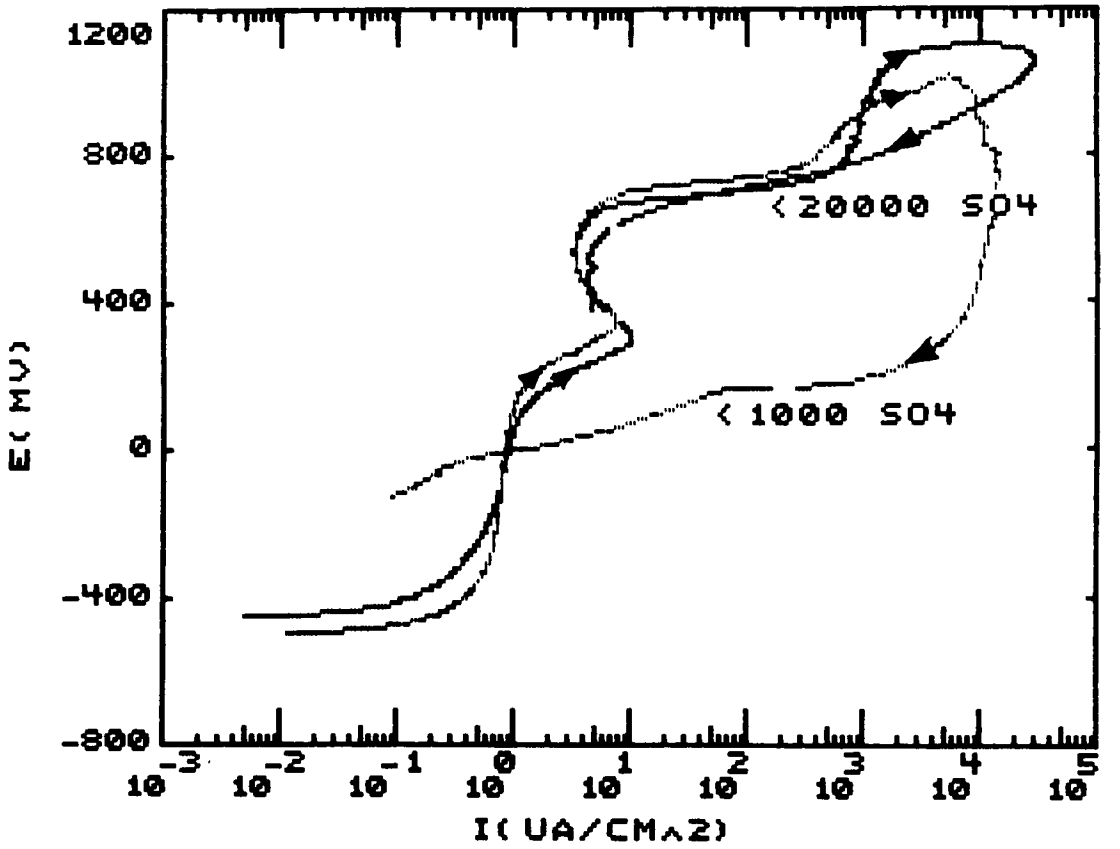

Figure 5-1. Effect of Sulfate on the Cyclic Polarization Behavior of Alloy 825. Solution: 1000 ppm Cl^-, 10 ppm NO_3^-, 2 ppm F^-, 95°C. Scan Rate = 0.167 mV/sec.

Two points are worthy of note in Table 5-3:

(1) Alloy C-22 is more resistant than alloy 825 to localized corrosion because no localized corrosion was observed on alloy C-22 in these tests (Visual Rating = 0), even at a chloride concentration of 10,000 ppm, whereas alloy 825 showed deep pits and crevice corrosion (Visual Rating = 4). This comes as no surprise because of its higher alloy content (higher Mo and W).

(2) The correlation between visual observation of localized corrosion and hysteresis in the polarization curve, as given by E_p - E_{rp}, is poor for alloy C-22, as was observed for alloy 825 at low chloride concentrations.

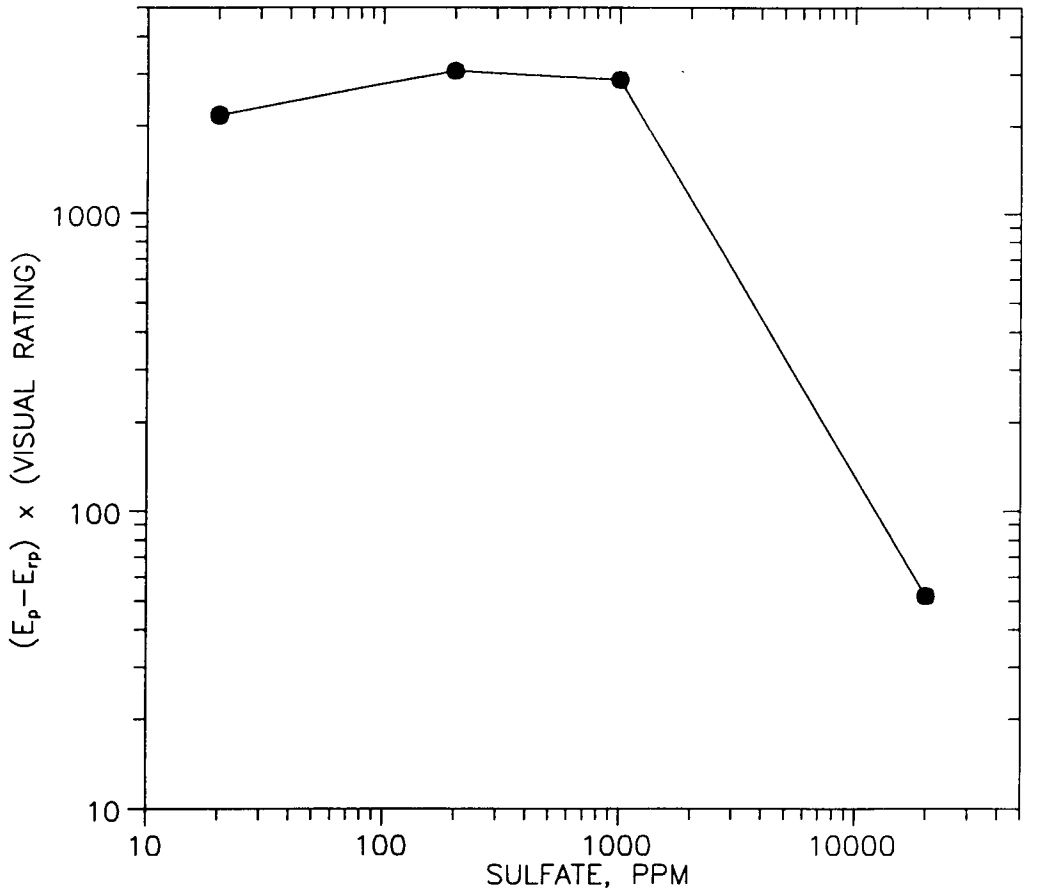

Figure 5-2. Effect of Sulfate on Localized Corrosion of Alloy 825 in a 1000 ppm Cl Solution at 95°C.

5.3. SUMMARY

(1) Literature review of localized corrosion was continued with examination of literature outside the high-level waste area. One of the localized corrosion test techniques of interest for long-term prediction is the crevice corrosion repassivation potential measurement.

(2) The effects of bicarbonate, pH, and sulfate on localized corrosion of alloy 825 were investigated using the cyclic polarization test technique. Bicarbonate increased the localized corrosion index slightly, but the statistical significance of this increase still needs to be established. Decreasing the pH from 8.3 to 5.0 in a 85 ppm bicarbonate solution containing 1000 ppm chloride increased the LCI considerably. Sulfate at concentrations of 20,000 ppm had a significant inhibitive effect on localized corrosion.

Table 5-3. RESULTS OF CYCLIC POLARIZATION TESTS ON ALLOY C-22 (HEAT NO. 2277-8-3175) AND ALLOY 825 (HEAT NO. HH4371FC). SOLUTION: 10 ppm NITRATE, 2 ppm FLUORIDE. TEMPERATURE: 95°C.

Environment	Alloy 825				Alloy C-22			
	E_{corr}	E_p	E_{rp}	LCI*	E_{corr}	E_p	E_{rp}	LCI
10,000 ppm Cl^- + 20 ppm SO_4^{2-}	-479	418	-343	3044	-547	618	406	0
10,000 ppm Cl^- + 1000 ppm SO_4^{2-}	-	-	-	-	-534	619	363	0

* LCI = (E_p - E_{rp}) x Visual Rating

(3) Alloy C-22, the CNWRA's reference alloy, exhibited a superior resistance to localized corrosion than alloy 825. The correlation between electrochemical parameters and visual observations of localized corrosion in alloy C-22 was found to be poor.

5.4. REFERENCES

Beavers, J. A. and C. L. Durr. 1990. *Container corrosion in high-level nuclear waste repositories*, First Semi-annual Report, Year 3. NRC FIN D1692. February 1990. Washington, D.C.: NRC.

Brookes, H. C. and F. J. Graham. 1989. Influence of the electrolyte and alloy composition on the pitting behavior of stainless steel alloys. *Corrosion* 45(4): 287-293.

Cragnolino, G. A. and N. Sridhar. 1991. Localized corrosion of a candidate container material for high-level nuclear waste disposal. Paper No. 35, *Corrosion/91*. Houston, Texas: NACE.

Kain, R. M. 1990. Crevice corrosion resistance of stainless steels in waters containing chloride and sulfate ions. *Corrosion in Natural Waters*. C. H. Baloun (ed.). ASTM STP 1086, Philadelphia, Pennsylvania: American Society for Testing and Materials: 37-53.

Leckie, H. P. and H. H. Uhlig. 1966. Environmental factors affecting the critical potential for pitting in 18-8 stainless steel. *J. Electrochem. Soc.* 113: 1262-1267.

Okayama, S., Y. Uesugi, S. Tsujikawa. 1987a. The effect of alloying elements on the repassivation potential for crevice corrosion of stainless steels in 3% NaCl solution. *Corrosion Engineering* 36: 157-168.

Okayama, S., S. Tsujikawa, K. Kikuchi. 1987b. Effects of alloying elements on stainless-steel depassivation pH. *Corrosion Engineering* 36: 631-638.

Rosenfeld, I. L. and I. S. Danilov. 1967. Electrochemical aspects of pitting corrosion. *Corrosion Sci.* 7: 129-142.

Smialowska, Z. 1986. *Pitting Corrosion of Metals*. Houston, Texas: NACE.

Stumm, W. and J. J. Morgan. 1981. *Aquatic Chemistry*. 2nd Ed. New York, NY: John Wiley & Sons.

Tamaki, K., S. Tsujikawa, Y. Hisamatsu. 1990. Development of a new test method for chloride stress corrosion cracking of stainless steels in dilute NaCl solutions. *Advances in Localized Corrosion*. H. Isaacs et al. (eds.). Houston, Texas, NACE: 207-214.

Tsujikawa, S. 1991. Repassivation method to predict long-term integrity of low alloy titanium for nuclear waste package. *Scientific Basis for Nuclear Waste Management XIV*. Vol. 212. Pittsburgh, Pennsylvania: Materials Research Society: 261-268.

Tsujikawa, S. and Y. Hisamatsu. 1984. Repassivation potential as a crevice corrosion characteristic for austenitic and ferritic stainless steels. *Proceedings of the Third Soviet-Japanese Seminar on Corrosion and Protection of Metals*. Ya. M. Kolotyrkin (ed.). Moscow: Nauka Publishers: 119-131.

6. STOCHASTIC ANALYSIS OF UNSATURATED FLOW AND TRANSPORT

by Rachid Ababou

Investigator: Rachid Ababou (CNWRA)

6.1. TECHNICAL OBJECTIVES

A quantitative characterization of large-scale flow and radionuclide transport through the heterogeneous unsaturated, fractured rock of Yucca Mountain will be necessary to evaluate compliance with the siting criteria and performance objectives associated with the proposed Yucca Mountain HLW repository (10 CFR 60.112 and 60.113). The pertinent technical issues concerning radionuclide migration at Yucca Mountain will need to be understood so as to demonstrate that the hydrogeologic conditions at the repository site strongly inhibit radionuclide transport to the accessible environment and meet performance criteria. Realistic modeling of the complex, heterogeneous flow and transport processes at Yucca Mountain will require incorporating the effects of relatively small-scale space-time variability in modeling large-scale unsaturated flow and radionuclide transport.

The specific objectives of the Project on "Stochastic Analysis of Large-Scale Flow and Transport Through Unsaturated, Fractured Rock" are as follows:

- Perform a review of the literature, assess available models and data relevant to the subject site, and select a global approach to model large-scale flow and transport in unsaturated, fractured rock;
- Develop hydrodynamic submodels for incorporation into the global model; and
- Perform large-scale simulations and participate in the validation of flow/transport models for Yucca Mountain.

The project is divided in three tasks to accomplish the objectives.

(1) Task 1 - Review, Analysis, and Initial Development of Modeling Approach

(2) Task 2 - Stochastic Submodel Development and Implementation

(3) Task 3 - Large-Scale Flow/Transport Simulation and Data Analysis

6.2. RESEARCH ACCOMPLISHMENTS

Task 1 has been essentially completed during the reporting period. The results are reported in a Major Milestone Report on "Approaches to Large-Scale Unsaturated Flow in Heterogeneous, Stratified, and Fractured Geologic Media" (Ababou, 1991a). The report was

submitted to NRC in draft form on April 1, 1991, and is being reformatted and edited for publication as NUREG/CR Report (due May 31, 1991). This report presents a review and assessment of the literature on available field data and modeling strategies, as well as preliminary developments towards a global modeling approach for Yucca Mountain. Although it contains a selective rather than an exhaustive review, many topics have been covered, and hundreds of references have been screened. In view of the reviewed field data and modeling methods, the conclusions of the report are essentially as follows.

Field-scale observations at several unsaturated contamination sites indicate evidence of both horizontal fluid pathways along geologic strata and preferential (vertical) fluid pathways along fissures or fractures. The Yucca Mountain site exhibits both features, i.e., near-horizontal stratification and near-vertical fracturing (in addition to nonvertical fracturing). There is also clear evidence of nonuniformity as well as anisotropy of the in-situ fracture network (variable density, preferred orientations) and of rock matrix properties (core permeabilities and porosities). Because the hydraulic properties of unsaturated geologic media are pressure-dependent, the response of the natural system at Yucca Mountain may be highly sensitive to the choice of hydraulic parameters and to their assumed spatial distribution.

However, precise quantitative data characterizing the hydrodynamic behavior of unsaturated rock over broad ranges of moisture content are scant. This lack of data can be partially compensated by auxiliary models relating the bulk constitutive relations of unsaturated fractured rocks (such as unsaturated conductivity curve) to more accessible parameters such as porosity, void structure, and fracture density, all of which are spatially variable. Tractable representations of three-dimensional heterogeneous porous matrix and fracture networks can be obtained by stochastic models based on probability and random-field theory. Such models require small sets of statistical parameters inferred from, or constrained by, information collected at analogous sites. Furthermore, site-specific features can be represented by introducing conditional probabilities using methods developed in the geostatistical literature (Delhomme, 1979).

Simulation of large-scale heterogeneous flow systems can be approached by: (1) direct simulation based on microscale flow equations with explicit heterogeneity, (2) indirect simulation of heterogeneous flow processes based on auxiliary hydrodynamic models and effective constitutive laws, and (3) various combinations of the above methods. Currently available "equivalent medium" models (as reviewed in Ababou, 1991a) do not have the capability to capture the dominant geologic features present at Yucca Mountain. These features include dipping stratification, fracturing along preferred directions, and other structural properties. When all major spatial features are considered in combination, they form inherently three-dimensional broad-band patterns of variability. Direct simulation of detailed unsaturated flow processes through both matrix and fractures may be possible, but has only been implemented for simplified fracture network geometry and uniform isotropic matrix, rather than fully three-dimensional anisotropic fractured media as occurs in-situ. The preferred approach to mountain-scale simulation of variably saturated flow may be a compromise between direct high-resolution simulation and indirect simulation based on refined equivalent media models. A hybrid approach

would be less computationally demanding, yet it would capture important fine-scale to coarse-scale phenomena both directly (explicitly) and indirectly (implicitly). For extensive references on both field evidence and models, the reader is referred to the just mentioned report (Ababou, 1991a).

In addition, preliminary work has started on the design of efficient flow solvers for vector supercomputer applications (Cray-2), and the development of auxiliary statistical models of unsaturated conductivity curves in heterogeneous formations. Some results were presented by R. Ababou at the Fifth Workshop on Unsaturated Flow and Transport in Fractured Rock, Tucson, January 1991. A more complete account of these ongoing activities will be given in future progress reports.

6.3. REFERENCES

Ababou, R. 1991a. *Approaches to Large Scale Unsaturated Flow in Heterogeneous, Stratified, and Fractured Geologic Media.* CNWRA 91-002. April, 1991. San Antonio, Texas: CNWRA.

Ababou, R. 1991b. Modeling heterogeneous unsaturated flow systems. *Proceedings of the Fifth Workshop on Flow and Transport Through Unsaturated Fractured Rock Related to High-Level Radioactive Waste Disposal.* January 7-10, 1991. Tucson, Arizona. (to be published as NUREG Report by the US. Nuclear Regulatory Commission).

Delhomme, J. P. 1979. Spatial variability and uncertainty in groundwater flow parameters: a geostatistical approach. *Water Resour. Res.* 15 (2): 269-280.

7. GEOCHEMICAL NATURAL ANALOGS

by English Pearcy, William Murphy, and Ronald Green

Investigators: English Pearcy (CNWRA), William Murphy (CNWRA), and Ronald Green (CNWRA)

7.1. Technical Objectives

The Geochemical Analog Project is designed to provide knowledge of the state of the art in natural analog studies applied to contaminant transport. Task 1 of the project, "Literature Review," was completed with the submission of the report entitled "Geochemical Natural Analog Literature Review" (Pearcy and Murphy, 1990; CNWRA 90-008). Task 2 (Identification of Site and Development of Workplan) began late in 1990 and is underway at present. Objectives of Task 2 include gathering preliminary field data on candidate analog sites, selecting a site or sites for investigation, defining research problems appropriate for the site or sites which are relevant to radionuclide transport in the Yucca Mountain environment, and developing a workplan to accomplish those investigations.

Among the results from Task 1 was the identification of several sites as potential locations for natural analog research (Pearcy and Murphy, 1990). These sites are: Peña Blanca, Mexico; McDermitt, Nevada-Oregon; and Akrotiri, Greece. During this quarter, field research was conducted at the Peña Blanca site. Objectives were to assess similarities between the Peña Blanca and Yucca Mountain environments and to evaluate potential geochemical analog research projects at Peña Blanca.

7.2. Research Results During the First Quarter of 1991

The Peña Blanca, Mexico, uranium district is in northern Mexico about 50 km north of Chihuahua City and is part of the Chihuahua City uranium province. Many of the uranium deposits in the district have been the subject of exploratory drilling programs and/or development by underground or open pit mining over a period of 20 years (Goodell, 1981); however, there has been no mining activity at Peña Blanca since 1983, except in the extreme northwest of the area where an exploration adit was completed in 1987 (J. Altamirano, personal communication). Combined, the Peña Blanca deposits include more than 2000 metric tons of U_3O_8 and constitute a major Mexican uranium resource.

7.2.1. Regional Structural Relations

Peña Blanca is part of the northern Mexico basin and range system and lies near the boundary between a stable craton to the west and a more mobile belt to the east (Goodell, 1985). The regional structural province is bounded to the east by the Trans-Pecos Range and to the west by the Sierra Madre Occidental (George-Aniel et al., 1985). The Sierra Peña Blanca is a west-dipping horst block with a superimposed set of parallel northwest-striking normal (extensional) faults.

7.2.2. Stratigraphy

The Peña Blanca stratigraphic sequence consists of Cretaceous limestones and mudstones on which a series of Tertiary silicic volcanics has been deposited. Host rocks for most of the uranium deposits are the Escuadra and Nopal Formations, which are composed of variably welded tuffs with air-fall, ignimbrite, vitrophyre, lahar, and water-worked units. The preserved total thickness of the volcanic units varies over the Sierra Peña Blanca area from 106 to 538 m, and rock ages range from 44 Ma to 35 Ma (Goodell, 1981).

7.2.3. Mineralogy and Geochemistry

The Peña Blanca tuffs are generally devitrified rhyolitic ignimbrites consisting largely of devitrified glass with quartz, sanidine, and minor biotite phenocrysts. Uranium in the ores was likely derived from the alteration of volcanic glass in the host tuffs. It is possible that the uranium was introduced from outside the district, but such long-distance mobility is not required given the relatively high background uranium concentrations typically present in silicic volcanic rocks (about 2 - 10 ppm). Uranium deposits at Peña Blanca are associated with hydrothermal alteration at faults, fractures, and breccias. There is also evidence of a district-wide alteration event which produced bleached zones along fractures; this alteration is present even kilometers away from known uranium mineralization. The present uranium mineralization is predominantly uranyl silicates (mostly uranophane, $Ca(UO_2)_2Si_2O_7 \cdot 6H_2O$; however, small quantities of uraninite (UO_{2+x}) does occur at one deposit (Nopal I). The uraninite occurs as irregularly shaped masses of fine-grained crystals, and is best described as pitchblende. It appears that pitchblende was the original form of the uranium mineralization and that it has been oxidized to the uranium silicates.

7.2.4. Hydrogeology of Sierra Peña Blanca

The distribution of uranium indicates that mineralizing hydrothermal fluids circulated primarily in faults and fractures, with brecciated zones and small fissures controlling detailed ore distribution. Matrix flow may have been important locally; some samples show pervasive penetration of mineralizing fluids through the matrix of the tuffs (e.g., sample PUE1-ECP-2 from the Puerto I mine in which feldspar phenocrysts are replaced by weeksite, $K_2(UO_2)_2Si_6O_{15}\bullet 4H_2O$).

All of the Peña Blanca uranium deposits are located above the water table in the unsaturated zone. At present, uranium is being remobilized by oxidizing meteoric groundwaters, which episodically penetrate the deposits through fractures in the unsaturated tuffs. The climate in the Peña Blanca area is arid, with annual precipitation of about 24 cm and average annual temperature of 19° C.

7.2.4.1. Surface-Water Hydrology

Surface water in the Sierra Peña Blanca area is restricted to intermittent streams, and springs that are typically located in stream beds and playa lakes. Intermittent streams are ubiquitous in the region and are usually associated with erosional depressions. None of the streams is perennial, and all appear to have water only after significant rain events. Several perennial springs occur where the groundwater surface intersects the base of a stream bed. The general trend of the streams is east-west toward the basins located east and west of Sierra Peña Blanca and perpendicular to the strike of Sierra Peña Blanca.

A drainage-basin divide is located along strike on Sierra Peña Blanca. Surface water on the western third of Sierra Peña Blanca flows to the west, toward an enclosed basin with a playa lake, Laguna el Diablo. Surface water flowing from the eastern two-thirds of Sierra Peña Blanca (near the Nopal I deposit) flows east toward a playa lake, Laguna el Cuevro, also located in an enclosed basin.

7.2.4.2. Groundwater Hydrology

The groundwater hydrological system has been tentatively interpreted to be a two-aquifer system, based upon available data. The upper unit is a water-table aquifer of low permeability. The base of the upper aquifer is not known, and it is possible that the upper unit is perched if it is not continuously extensive and if its base is situated on an impermeable horizon. The surface of the upper unit is controlled by the topography of the region. In general, the upper aquifer is only present where there is sufficient topographic relief. For example, the upper aquifer can be found in the Sierra Peña Blanca but is absent in the basin containing Laguna el Quervo. The extent of the upper unit to the east of Sierra Peña Blanca, where the basin elevations are higher (e.g., greater than 1500 m msl) is not known.

The areal extent of the upper unit appears to be limited. Related to this, the amount of recharge to the upper aquifer is also limited by the available recharge area. This unit is interpreted to be of low permeability with limited recharge because only isolated groundwater discharge appears at the surface (e.g., springs, seeps) even though the potentiometric surface is inferred to be close to the ground surface at a multitude of locations including many dry stream beds. The limited areal extent and recharge of the upper aquifer, in conjunction with its low permeability, define this unit as an aquifer (or aquiclude) with limited capability of providing a significant quantity of water.

The only use of the upper aquifer has been the installation of catchments along stream beds for use as stock ponds. No operational wells were observed in the upper aquifer, thus supporting the premise that the upper unit is incapable of sustaining a well due to its low permeability and/or limited extent.

Limited information is available on the lower aquifer. A total of four water wells at three locations in the eastern portion of Sierra Peña Blanca provide information

on this water-bearing unit. Well logs have not been available. The western-most three wells (installed for mining-related purposes) are not currently used, but are reported to have been capable of providing significant amounts of water (J. Altamirano, personal communication). The fourth well is located in the basin just east of the Sierra Peña Blanca. The well in the basin is equipped with a piston pump. This well is currently supplying water for a reservoir and associated stock ponds on a ranch. The shallow sediments in the basin to the east of Sierra Peña Blanca are composed largely of clays. The ranch well is assumed to be installed in a stratigraphic unit below the clay unit. The nature of the unit in which this well is completed has not been identified and could be either consolidated or unconsolidated media. The media in which the other three wells are located are not known.

The depths to water in the wells in the lower aquifer are not accurately known but have been estimated. The depths to water in the wells at the Margaritas mining camp (with surface elevations of about 1420 m msl) are reported to be in excess of 100 m (J. Altamirano, personal communication). This was roughly verified by sounding the well with a dropped pebble which required approximately six seconds to reach the water. A pebble dropped in the well located along the stream bed (with a surface elevation of about 1340 m msl) to the east of Nopal I required eight seconds, thus suggesting that the depth to water in this well is also in excess of 100 m. The depth to water in the ranch well (with a surface elevation of about 1260 m msl) was reported by a ranch worker to be about 60-70 m. The elevation of groundwater in these wells appears to be approximately 1200-1300 m msl, and could be lower but probably not significantly higher. The elevation of the lower aquifer would therefore be about 200-300 m below the 0-meter level at Nopal I.

The elevation of the potentiometric surface of the upper aquifer in the area proximal to these wells has been estimated to be about 1250-1450 m msl, or about 50-200 m above the elevation of the lower aquifer, thus supporting the hypothesis that there are two distinct hydrogeologic units.

7.2.4.3. Hydrogeologically Undefined Areas

Additional regions within the study area have hydrogeology that is not well understood. One such extensive region includes the western extents of the upper and the lower aquifer. Important information that is lacking includes the direction of groundwater in the basin containing Laguna el Diablo. Groundwater in the upper aquifer in the western portion of the Sierra Peña Blanca appears to flow to the west toward the Laguna el Diablo basin. It is assumed that an upper aquifer also exists in the minor range to the west containing Cerro el Cerote, and that groundwater flows essentially to the east and west in response to the topographically-influenced potentiometric surface. However, the hydraulic relationship among these different units and the associated directions of groundwater flow are not known.

The groundwater elevation in the basin containing Laguna el Diablo is lower than the upper aquifer groundwater elevations in the western portion of the Sierra Peña Blanca but higher than the lower aquifer groundwater elevations at the eastern edge of Sierra

Peña Blanca. It is not apparent whether groundwater in the basin west of Sierra Peña Blanca is hydrogeologically connected to the upper or the lower aquifer.

Wells proximal to Laguna el Diablo have groundwater at elevations similar to the surface-water elevations in the lakes, 1530-1550 m msl (I. Reyes, personal communication). The basin sediments and the formations in which these basin wells are located are not known. Consequently, it is not known if the aquifer in this region is under water table or confined conditions. If the basin sediments are mostly clays as in the basin containing Laguna el Cuervo, then Laguna el Diablo may not be hydraulically connected with the aquifer. Under this condition, the aquifer would be confined. However, if the playa lake and the aquifer are hydraulically connected, then the aquifer would be under water table conditions. It would appear to be more probable, but not necessary, that the basin aquifer would be under water table conditions and not confined conditions if it were an extension of the upper aquifer at Sierra Peña Blanca.

An additional area of uncertainty is the hydrogeologic relationship between the aquifer in the basin to the west of the minor range containing Cerro el Cerote and the basins to the west and the east of Sierra Peña Blanca. The elevation of groundwater in this western basin is reported to be approximately 1500 m msl (I. Reyes, personal communication). The elevation of groundwater in this basin is therefore lower than the elevation of surface water in Laguna el Diablo (1550 m msl) but higher than the elevation of groundwater measured in the wells at the eastern limit of Sierra Peña Blanca (1200-1300 m msl). The hydraulic relationship between groundwater in this western basin and either of the basins to the east and west of Sierra Peña Blanca is not known.

7.2.5. Potential Analog Site

Among the several uranium deposits in the Peña Blanca district, the Nopal I deposit was identified during field reconnaissance as the most promising site for a geochemical analog study relevant to a high-level waste repository at Yucca Mountain. The Nopal I deposit consists of a near vertical breccia pipe some 40 m in diameter which extends across the boundary of the Nopal and Coloradas formations (both units are silicic tuffs and are separated by a basal vitrophyre), and is known to cover a vertical interval of at least 100 m. The breccia pipe contains high-grade uranium mineralization in the form of pitchblende and uranyl silicates. The pitchblende appears to be the original uranium mineral; the uranyl silicates appear to have formed as a result of oxidation of the pitchblende.

Exposure of the ore body at Nopal I is unusually good. The mineralization is exposed on broad benches at the 0 and +10 m levels, which together provide surface access to a horizontal section across the entire width of the deposit. A shaft down the breccia pipe exists, as well as a series of adits; the adits at the 0 and -100 m levels are at least partially accessible. The lowest level of the deposit is significantly above the local watertable (perhaps 100 to 200 m above, as indicated by water levels in the nearest wells, see Section 7.2.4.2).

The Nopal I deposit has also been the focus of earlier research (e.g., Cardenas-Flores, 1985; George-Aniel, et al., 1985; Goodell, 1981; Ildefonse, et al., 1990a and b; Leroy, et al., 1987). This information provides considerable background on the mineralogy and alteration at Nopal I. Such background would be a useful supplement to information developed in the context of any analog work at the site. The excellent exposure, the relatively small scale and apparently simple geometry, the location of the ores in the unsaturated zone of a silicic tuff sequence, and the occurrence of apparently primary pitchblende and secondary oxidized uranyl silicate minerals make the Nopal I deposit a promising site for geochemical analog studies pertinent to the Yucca Mountain geologic setting.

7.3. Conclusions

The Peña Blanca district appears to provide an excellent analog to the proposed Yucca Mountain repository system. Analogous aspects of the district are the silicic, tuffaceous rock types; semi-arid climate; unsaturated hydrologic regime; and uranium mineralization. Specifically, the Nopal I deposit has been identified as a potential site for further work because the mineralization is accessible and well-exposed; the deposit has a relatively small scale and simple geometry; both primary pitchblende and oxidized uranyl silicate alteration minerals occur in the ore, and information is available from previous research at the deposit. A variety of present and past processes at Nopal I are analogous to those that could affect radionuclide migration at Yucca Mountain. Processes governing the oxidation of Peña Blanca uraninite, the resulting dispersion of uranium from the sites of original mineralization, and the formation of secondary uranyl silicates are analogous to processes that may affect spent nuclear fuel and elemental migration at the repository.

7.4. References

Cardenas-Flores, D. 1985. Volcanic stratigraphy and U-Mo mineralization of the Sierra de Peña Blanca District, Chihuahua, Mexico. *Uranium Deposits in Volcanic Rocks*. International Atomic Energy Agency (IAEA), Proceedings of a technical committee meeting, El Paso, TX April 1984. IAEA-TC-490. Austria: IAEA 125-136.

George-Aniel, B. G., J. Leroy, and B. Poty. 1985. Uranium deposits of the Sierra Peña Blanca. *Uranium Deposits in Volcanic Rocks*. IAEA, Proceedings of a technical committee meeting, El Paso, TX April 1984. IAEA-TC-490. Austria: IAEA 175-186.

Goodell, P. C. 1981. Geology of the Peña Blanca uranium deposits, Chihuahua, Mexico. *Uranium in Volcanic and Volcaniclastic Rocks- AAPG Studies in Geology No. 13.* P. C. Goodell and A. C. Waters eds. El Paso, TX: American Association of Petroleum Geologists: 275-291.

Goodell, P. C. 1985. Chihuahua City uranium province, Chihuahua, Mexico. *Uranium Deposits in Volcanic Rocks.* IAEA, Proceedings of a technical committee meeting, El Paso, TX April 1984. IAEA-TC-490. Austria: IAEA 97-124.

Ildefonse, P., P. Agrinier, and J.-P. Muller. 1990a. Crystal chemistry and isotope geochemistry of alteration associated with the uranium Nopal 1 deposit, Chihuahua, Mexico. *Geochemistry of the Earth's Surface and of Mineral Formation.* Aix en Provence, France: 371-372.

Ildefonse, P., J.-P. Muller, B. Clozel, and G. Calas. 1990b. Study of two alteration systems as natural analogues for radionuclide release and migration. *Engineering Geology* 29:413-439.

Leroy, J. L., B. Aniel, and B. Poty. 1987. The Sierra Peña Blanca (Mexico) and the Meseta Los Frailes (Bolivia); the uranium concentration mechanisms in volcanic environment during hydrothermal processes. B. Poty and M. Pagel, eds. *International Colloquium on Concentration mechanisms of uranium in geological environments, Oct. 2-5, 1985.* Nancy, France: 211-234.

Pearcy, E. C. and W. M. Murphy. 1990. Geochemical Natural Analogs Literature Review. Center for Nuclear Waste Regulatory Analyses (CNWRA), San Antonio, Texas. 90-008 (draft).

8. PERFORMANCE ASSESSMENT RESEARCH

by Budhi Sagar and Gordon Wittmeyer

PHASE 2 INTRAVAL PROJECT : LAS CRUCES TRENCH SOLUTE TRANSPORT MODELING STUDY, PLOT 2, EXPERIMENT A

Investigators: Budhi Sagar (CNWRA) and Gordon Wittmeyer (CNWRA)

8.1. TASK OBJECTIVES

The objective of this task is to use the PORFLO-3, Version 1.2 (single-phase version) computer code to simulate the flow of water and transport of tracers (bromide and tritium) at the Las Cruces Trench site in New Mexico. This work falls under task 7 (Methodology for Validation of Models) of the Performance Assessment (PA) Research project plan. The Las Cruces Trench experiment is identified as Test Case 10 for Phase 2 of the INTRAVAL project. This section describes the conceptual model development, model structure parameterization and calibration and validation strategies to be pursued.

8.2. TECHNICAL OBJECTIVES

Specific technical objectives of this task are as follows:

(1) To develop conceptual and mathematical models of the unsaturated flow and transport processes observed during the Plot 2a Experiment performed at the Las Cruces Trench. Development of the conceptual model includes determining the relevant physical processes and the appropriate set of partial differential equations which describe these processes, locating model boundaries and describing the physical conditions at the boundaries, and determining the initial values of pressure and solute concentration in the area to be modeled.

(2) To develop a suite of auxiliary computer codes to assist in the construction of input data sets for PORFLO-3. In particular, these codes are required to facilitate mapping the location of neutron probes, tensiometer and suction lysimeter measurement points, and the location of zones in which soil hydraulic properties were measured to the block-centered finite difference mesh assembled for PORFLO-3.

(3) To calibrate the model both for flow of water and transport of tracers by adjusting boundary and initial conditions, soil hydraulic property zones and associated property values, and sorptive and dispersive properties assigned to the model.

(4) To use the model calibrated on the Plot 2a experiment data to predict the movement of tritium, bromide, boron, chromium, pentafluorobenzoic acid, and 2,6-difluorobenzoic acid applied with the water during the Plot 2b experiment.

(5) To use the maximum amount of available soil-hydraulic property data in defining the structure of the model's material zones instead of defining the material zones by layers or by a single homogeneous unit. Subsequent reduction of the number of model material zones will allow determination of the degree of resolution in the model's structure needed to adequately model the movement of the solute. Moreover, the detailed description of the material properties should result in a sufficiently detailed velocity field to obviate the need to use large values of dispersivity in the advection-dispersion equation.

8.3. DESCRIPTION OF EXPERIMENT AND OBSERVED DATA

8.3.1. Experimental Setting

The experimental trench is located northeast of Las Cruces, New Mexico, on the New Mexico State University College Ranch near the north end of the Doña Ana Mountains. The climate at the experiment site is semi-arid. Class A pan evaporation is 239 cm per year, while average annual precipitation is only 23 cm, over half of which falls during the summer monsoon season. As shown in Figure 8-1, the trench is 26.4 meters long, 4.8 meters wide, and 6 meters deep. Plot 2, located adjacent to the north face of the trench, is irrigated by an array of 80 drip lines aligned parallel to the trench face and covering a surface strip 12 meters long and 1.2 meters wide. During the Plot 2a experiment, water was applied to the strip at a rate of 0.43 cm/day for 75.5 days. Tritium and bromide were applied to the strip during the first 11.5 days at concentrations of 0.1mCi/l and 0.8g/l, respectively. Water content was monitored by neutron probes through the network of access tubes shown in Figure 8-1; matric potential was monitored by tensiometers installed in the face of the trench, and solute samples were obtained using suction lysimeters installed in the trench face. Locations of soil samples for which the hydraulic properties were measured are shown in Figure 8.2.

8.3.2. Observed Data

Data used in the modeling exercise came from the Las Cruces Trench Database, which is accessible by FTP at HELEN.NMSU.EDU (128.123.3.7) with username SOILS and password LASCRUCES. A description of each file in the database is given in the files 1_README.TXT and 2_README.TXT. Soil-hydraulic properties consist of measured and estimated parameters for the van Genuchten model. These data are listed by soil sample in the file VGPARM.DAT. The x, y, and z coordinates of each soil sample are contained in the file SAMPLOC.DAT. The measured water-content data from the Plot 2a

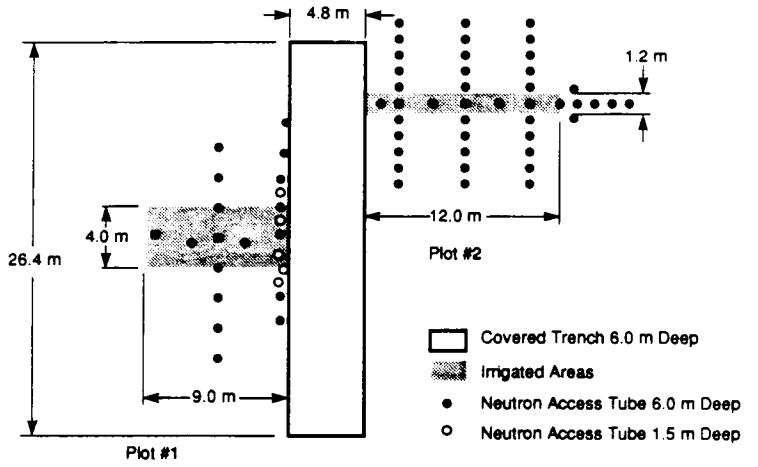

Figure 8-1. Plan view of Las Cruces Trench Site

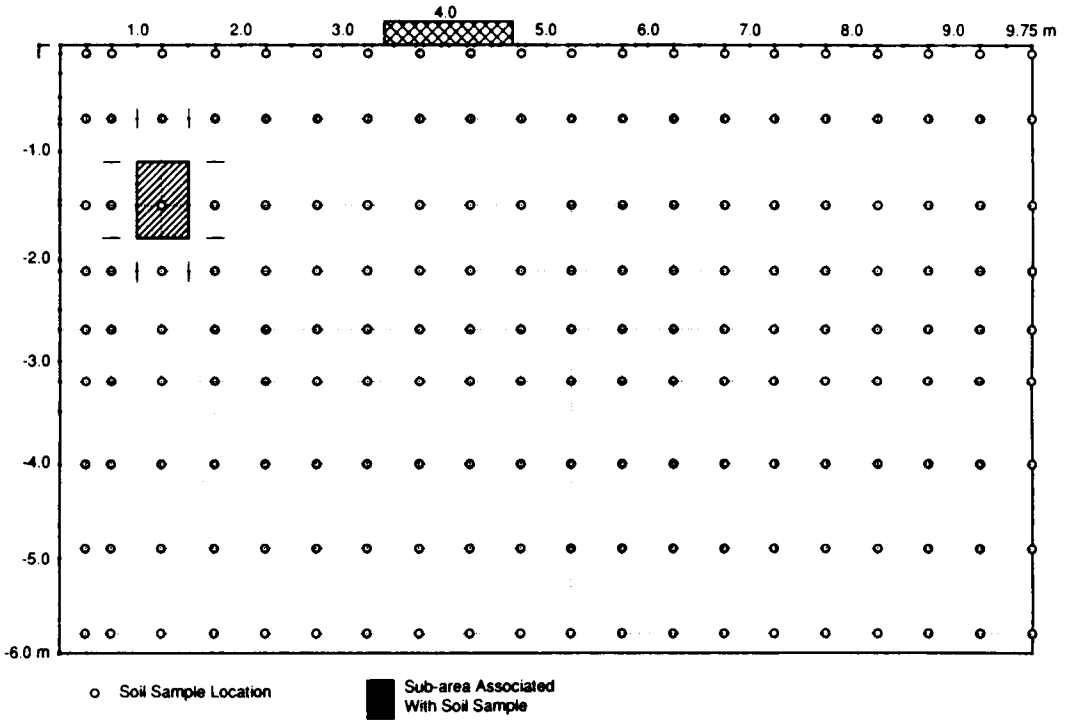

Figure 8-2. Soil-sample locations and model material zones

experiment are listed by day, neutron-probe access-tube number, and the z coordinate of the neutron probe in the file THETA2.DAT. The x and y coordinates of each neutron access tube are listed in the file TUBELOC2.DAT. Measured relative concentrations for bromide and tritium are listed by day and solution sampler number in the files BR2.DAT and TRIT2.DAT, respectively. The x, y, and z coordinates of each suction lysimeter are listed in the file SOLLOC2.DAT.

8.4. CONCEPTUAL MODEL DESCRIPTION

Experiment 2a employs a thin strip for application of water and solute. This can be thought of as a line source from which both the water and the solute migrate. Assume that in a cartesian coordinate system, the y-coordinate direction coincides with the line source. Considering the layout of the experiment, it is then a fair assumption that the migration of the fluid and tracer will be mostly in the x-z plane. Furthermore, soil-property variations in the y-direction are not measured. Therefore, as a first approximation, it was decided that a 2-D model of flow and transport in the x-z plane was adequate. A three-dimensional simulation may be undertaken later to study the effect of this assumption. In the x and z directions, the model domain extends from the northwest corner of the trench 975 cm to the east and from the ground surface down 579 centimeters. The finite difference mesh was designed so that computational nodes were coincident with both tensiometer and suction lysimeter locations.

There were 594 soil samples collected for which the van Genuchten parameters were estimated or measured. Of these 594 samples, 180 lie within the model area and have complete records of the van Genuchten parameters-- α, n, θ_s, and θ_r --and the saturated hydraulic conductivity, K_s. To use this property data fully, it was assumed that the model domain was made up of 180 material zones. The boundaries of each one of these material zones in the finite difference mesh were determined by drawing right bisectors through the lines joining the measurement points. In this manner, rectangular zones are obtained, one of which is shown in Figure 8-2. The van Genuchten parameters as well as mass transport properties were assumed to be uniform at all nodes within each material zone. No data on mass transport properties such as dispersivities were available. Consistent with the grid dimensions, a longitudinal dispersivity of 1 cm and transverse dispersivity of 0.1 cm was assumed. The coefficient of molecular diffusion was assumed to be 10^{-3} cm^2/sec.

Initial pressure heads were determined from the neutron-probe measurements of water content made in the neutron-probe access tubes which lie in a vertical plane 2 meters north of the trench face. The same procedure described above for defining material zones was used to define quadrilateral zones centered on each water-content measurement location within which the initial water content was defined to be constant. Both the soil-hydraulic-property material zone and initial water-content material zone in which each node in the computational grid resides was determined and the appropriate initial water content and van Genuchten parameters were then assigned to that node. The initial matric potential, ψ_m, was computed from the van Genuchten model relating water content, θ, and ψ_m. In many cases

the water content measured with the neutron probe was less than the estimated residual water content, θ_r. Inasmuch as the residual water-content values from the soil samples was defined to be the water content of the soil after reaching equilibrium in a pressure chamber fitted with a 15-bar porous pressure-plate (15,300 cm H_2O), if $\theta < \theta_r$, then ψ_m=-15300 cm H_2O. Moreover, it was decided that if the computed initial matric potential at any node was less than -15300 cm H_2O, the initial matric potential at that node would be set to -15300 cm H_2O. Thermocouple psychrometer measurements of matric potential of soil samples retrieved during installation of neutron probe-access holes at depths greater than 210 cm exceeded 65,000 cm. of water. The higher matric potentials used here should effect a slightly faster rate of solute movement. Initial pressure heads were determined simply by adding the position head, z, of the node to the computed initial matric potential, $\psi = \psi_m + z$.

Boundary conditions for the pressure-head variable, ψ, were defined to be no-flow type, $K(\psi_m)\nabla(\psi_m+z)\cdot\mathbf{n} = 0$, except at the bottom of the model and at the portion of the surface where the strip was located. On the bottom boundary of the model, the negative of the pressure head gradient is directed downwards and has magnitude 1 to simulate gravity drainage. At the strip, source the boundary condition is a Neumann type, $K(\psi_m)\nabla(\psi_m+z)\cdot\mathbf{n} = q$. During the first 75.5 days of the simulation, q=0.43 cm/day, after which the flux changed to q=0.

Boundary conditions for the concentration variable, c, were defined to be no-flux type at all nodes except where the strip source was located. It should be noted that the no-flux at the boundary means only that the diffusive and dispersive fluxes are zero. Tracer mass crossing the boundary along with convecting water is never put to zero even when a no-flux boundary condition is applied. During the first 11.5 days of simulation, a Dirichlet or prescribed concentration boundary condition was used to simulate the presence of dissolved bromide ion in the infiltrating water. To simulate the abrupt cut-off of dissolved bromide in the infiltrating water after 11.5 days, two alternative boundary conditions were tried. In the first simulation, the boundary condition at the strip after 11.5 days was changed to no-flux while in the second simulation, keeping every thing else the same, the boundary condition at the strip was changed to zero concentration. The results from these two simulations differed considerably.

For the cases where the initial pressure heads were determined from the measured water contents, the finite-difference mesh used for the PORFLO-3 simulations consisted of 87 nodes in the x-direction, 3 nodes in the y-direction, and 99 nodes in the z-direction. The 3 nodes in the y-direction are the minimum required to run the three-dimensional code. All nodes in the x-z planes located at the first and third y-nodes were assigned as no-flow boundary nodes to effects 2-0 flow in the middle plane. In addition to the two simulations mentioned, another simulation was performed in which the initial matric potential was assumed to be uniform at all nodes and equal to -150 cm of water. For this case, the number of nodes used in the x, y, and z directions was 87, 3, and 101, respectively. In all three simulations, the grid spacing in both the x and z directions was nonuniform; that is,

it is much finer close to the strip source and gradually becomes coarser towards the boundaries.

8.5. MATHEMATICAL MODEL DESCRIPTION

As mentioned previously, the mathematical model used in this study is the PORFLO-3, Version 1.2. The theory of PORFLO-3, Version 1.0, is described by Sagar and Runchal (1990). Three main differences exist between Version 1.0 and Version 1.2. These are: (1) Modifications were made to Version 1.0, so that data on medium properties can be read from files external to the main input file. This modification was made to accommodate data generated to represent medium properties when these are assumed to be represented as stochastic random fields, e.g., Ababou (1990). This feature was not used in the study reported here. (2) Version 1.0 does implement the flux (or Neuman) boundary condition but not a gradient boundary condition. Since for partially saturated porous media, hydraulic conductivity is a function of saturation, implementation of flux boundaries and gradient boundaries is not the same. In Version 1.2, the implementation of gradient boundary condition was added. This feature was used in setting the lower boundary condition in this study. (3) In Version 1.0, the finite difference formulation is based upon a pressure-based partial-differential equation. This was found to be provide unsatisfactory mass balance, especially when large time steps were taken in the presence of sharp fronts. To remedy this situation, the discretization was changed to consider a mixed, saturation-pressure based equation. In the mixed equation, the time derivative is kept as a function of moisture content while all the remaining terms are functions of pressure (Celia, 1990). As reported by Rockhold and Wustner (1991), this formulation of PORFLO-3 provides almost perfect mass balance.

Because of the rather large amount of input data to be processed, pre-processors were written for this specific problem. These pre-processors were used to read the data directly from the data bases described in Section 8.3.2 and write to a PORFLO-3 input file.

8.6. SIMULATION RESULTS

All simulations made of Experiment 2a were performed using free bench-marking time provided by the Computing and Communications Division at Los Alamos National Laboratory on their Cray Y/MP 2-64 running UNICOS. As shown in Table 8-1, four separate simulations of the experiment were performed. Two simulations (runs 2 and 7) were made with relatively wet, initial conditions by specifying the initial matric potential to be -150 cm of water at each node. Runs 2 and 7 differ only by the type of boundary condition for concentration applied to the surface strip after 11.5 days. For runs 5 and 6 the initial matric potential at each node was computed from the measured initial water content. As is the case for runs 2 and 7, runs 5 and 6 differ only in the type of boundary condition for concentration applied at the strip after 11.5 days. Preliminary analysis of runs 5 and 6 indicate that the computed initial conditions are inconsistent with the observed water

contents. For this reason, detailed analysis of the calculated bromide plumes from runs 5 and 6 will not be performed until this has been satisfactorily resolved. The results from runs 2 and 7 have not yet been analyzed. Detailed analyses of all four runs described here as well as the analysis of additional model runs which may need to be performed will be discussed fully in subsequent research reports.

Table 8-1. Trench Simulation Computer Runs

Strip Boundary Condition	Initial Condition	
	Initial ψ_m=-150 cm H_2O	Initial ψ_m Based on Measured θ
Neumann B.C.	Run 2	Run 5
Dirichlet B.C	Run 7	Run 6

8.7. SUMMARY AND CONCLUSIONS

A two-dimensional simulation of experiment 2a at the Las Cruces experiment was performed with the PORFLO-3, Version 1.2. To the extent possible, measured property data were used directly without any smoothing. For each measurement, a representative volume was defined by drawing right bisectors between measurement points. From a stochastic view point, this is equivalent to assuming 180 statistically independent material zones. These results will be compared with simulations assuming correlation lengths, which are greater than the size of the material zones and assess the effect of smoothing on the structure of the plume.

8.8. REFERENCES

Celia, M. A., E. T. Boulatas, and R. L. Zarba. 1990. A General Mass-Conservative Numerical Solution for the Unsaturated Flow Equation. *Water Resour. Res.* 26(7):1483-1496.

Hills, R. G., P. J. Wierenga, and M. R. Kirkland. 1990. Two-dimensional flow predictions for the Las Cruces Trench Experiment 2. Unpublished Manuscript. Las Cruces, New Mexico: New Mexico State University.

Rockhold M. L. and S. K. Wurstner. 1991. *Simulation of Unsaturated Flow and Solute Transport at the Las Cruces Trench Site Using the PORFLO-3 Computer Code.* PNL-7562. Richland, Washington: Pacific Northwest Laboratory.

Runchal, A. K. and B. Sagar. 1989. *PORFLO-3: A Mathematical Model for Fluid Flow, Heat and Mass Transport in Variably Saturated Geologic Media - Users Manual, Version 1.0.* WHC-EP-0041. Richland, Washington: Westinghouse Hanford Company.

Sagar, B. and A. K. Runchal. 1990. *PORFLO-3: A Mathematical Model for Fluid Flow, Heat and Mass Transport in Variably Saturated Geologic Media - Theory and Numerical Methods, Version 1.0.* WHC-EP-0042, Westinghouse Hanford Company, Richland, Washington.

Wierenga, P. J., A. F. Toorman, D. B. Hudson, J. Vinson, M. Nash, and R. G. Hills. 1989. *Soil Physical Properties of the Las Cruces Trench Site.* NUREG/CR-5441. Washington, D.C.: U.S. Nuclear Regulatory Commission.

9. SORPTION MODELING FOR HLW PERFORMANCE ASSESSMENT

by Roberto Pabalan and David Turner

Investigators: Roberto Pabalan (CNWRA), David Turner (CNWRA), James Prikryl (CNWRA), and Paul Bertetti (CNWRA)

9.1. INTRODUCTION

An evaluation of the effectiveness of geologic systems as barriers to radionuclide migration requires an understanding of the chemical and physical processes by which aqueous species are sorbed on geologic materials. These processes, which may include adsorption, ion exchange, or precipitation, are commonly represented collectively by empirical parameters, such as sorption coefficient (K_d) or retardation factor (R_f), in transport calculations supporting performance assessments of geologic repositories. However, there is active debate on the usefulness of these empirical parameters in quantitatively describing aqueous-solute/rock interactions for performance assessment calculations. It is recognized that transport models which use these parameters, particularly those that assume constant K_d's or R_f's, do not explicitly take into account many potentially important geochemical phenomena that occur during transport in natural systems (e.g., Kent et al., 1988; Siegel, 1989; Siegel et al., 1990), including aqueous complexation, precipitation/dissolution reactions, competitive sorption, changes in groundwater chemistry, and variability in substrate composition, as well as changes in temperature and pressure. Therefore, questions have been raised regarding the adequacy of transport calculations using K_d or R_f in performance assessment (e.g., Kelmers et al., 1987).

Although it is currently impractical and potentially unnecessary to conduct performance assessments using models for sorption phenomena based on fundamental physicochemical principles, it is important to have knowledge of specific sorption reactions that may take place in the geologic system of interest. Otherwise, the transport models used for repository predictions may have no physical basis and may be little more than computerized guesses (Kelmers et al., 1987). Some investigators believe that a conservative approach would be to determine a defensible lower limit for radionuclide retardation (e.g., Meijer, 1990). However, even such an approach would require some mechanistic basis for justifying the use of a specific K_d or R_f value as a lower limit, unless a value of $K_d=0$, or $R_f=1$, is assumed.

9.2. TECHNICAL OBJECTIVES

To support the Nuclear Regulatory Commission's (NRC) high-level waste (HLW) program, the Center for Nuclear Waste Regulatory Analyses (CNWRA) is conducting research activities under the Sorption Modeling for HLW Performance Assessment Research Project. The general objectives of this project are:

- To obtain a mechanistic understanding of the important radionuclide sorption processes and the physical and chemical parameters that affect sorption behavior in the Yucca Mountain, Nevada environment;

- To investigate the applicability of coupled-hydrogeochemical models which use simple representations of sorption phenomena to Yucca Mountain performance assessment; and

- To develop practical but scientifically defensible approaches to modeling sorption at Yucca Mountain, and the requisite databases to support such models.

The goal of the research project is to develop sufficient understanding of radionuclide transport issues so that timely prelicensing guidance can be provided to the DOE and a sound basis is available for evaluating the DOE license application. For the purpose of achieving the above objectives, the research project has been divided into three tasks, namely: Task 1 - Literature Review and Development of Approach; Task 2 - Coupled Hydrogeochemical Modeling - Application of Simplified Models to NRC Regulatory Needs; and Task 3 - Sorption Experiments. Only Task 1 was active during this report period. It consisted of literature review of experimental, theoretical, and modeling studies on sorption processes and evaluation of available coupled reaction-transport models. Results of the literature review conducted during this quarter are discussed below.

9.3. EXPERIMENTAL AND MODELING STUDIES OF URANIUM SORPTION

To develop a mechanistic understanding of important radionuclide sorption processes and the physical and chemical parameters that affect sorption behavior in the Yucca Mountain environment, a literature review of experimental and modeling studies of uranium sorption on geologic media was conducted. Uranium was selected as the initial focus of the literature review for several reasons. First, uranium comprises a large inventory in the high-level wastes which will be emplaced in the proposed repository. Second, uranium has a relatively complicated aqueous chemistry compared to radioelements such as ^{137}Cs and ^{90}Sr due to complexation reactions as well as hydrolysis leading to formation of polymeric species (Cotton and Wilkinson, 1980). Therefore, its sorption behavior is expected to be more complicated than those for ^{137}Cs and ^{90}Sr. Although the detailed aqueous chemistry of uranium is different from that of other actinides such as plutonium, americium, and neptunium, the latter radioelements exhibit similarly strong tendencies for hydrolysis and polynuclear ion formation as well as complex formation (Cotton and Wilkinson, 1980; Allard, 1982). Thus uranium is a good analog for understanding the sorption behavior of the other actinides. Third, uranium has a more extensive and better evaluated thermodynamic database for aqueous species compared to the other actinides. Such a database is prerequisite for a mechanistic understanding of sorption processes.

The literature review conducted during this quarter was focused toward evaluating experimental methods for studying sorption of uranium (and other actinides) on geologic media and the different approaches to modeling sorption. Based on the information derived from this

review, a work plan for conducting experimental studies on uranium sorption on geologic media was developed and submitted to NRC for review and approval. This work plan is briefly discussed in Section 9.3.4. The experiments described in the work plan are designed to facilitate understanding the fundamental controls on uranium sorption, i.e., how and why sorption values change as a function of the properties of the sorbing solid and the aqueous phase. Experimental and analytical techniques, as well as methods for data interpretation and modeling, developed in the study will be useful in extending the studies to other actinides and radioelements. The experiments to be conducted will also provide data that will be useful for validating hydrogeochemical transport codes (Task 2 of the Sorption Research Project), in interpreting and modeling results derived in the CNWRA's Geochemical Analog Research Project, and in evaluating data and modeling needs for the CNWRA's Performance Assessment Project.

9.3.1. Aqueous Chemistry of Uranium (6+)

Before the sorption behavior of uranium can be discussed, it is important to have an understanding of its chemistry in aqueous solutions. Several factors are important in controlling the aqueous speciation of uranium, namely: (1) Eh, (2) pH, (3) total concentration of uranium in solution (ΣU), (4) presence and concentration of complexing ligands, and (5) temperature (Langmuir, 1978; Lemire and Tremaine, 1980; Paquette and Lemire, 1981). In natural systems, Eh and pH constraints make likely U^{4+} and U^{6+} as the only important oxidation states of uranium. U^{5+} species are also known to have a stability field in reduced waters below pH 7 (Langmuir, 1978; Lemire and Tremaine, 1980), but they are prone to disproportionation (Allard, 1982). The relative stabilities of the U^{4+}, U^{5+}, and U^{6+} aqueous species at 25°C are shown on Figure 9-1 as a function of Eh and pH. The figure was calculated for ΣU equal to 10^{-6} M and for conditions where complexing ligands other than OH^- are absent (Langmuir, 1978).

Due to the very low solubility of uranium minerals as aqueous U^{4+} species under reducing conditions and the limited stability field of the U^{5+} species, almost all studies of uranium sorption have been limited to U^{6+} (Tripathi, 1984). For the same reasons and because the geochemical environment at Yucca Mountain is expected to be largely oxidizing, most of the discussion here on uranium aqueous chemistry will be limited to that of U^{6+}.

The principal chemistry of U^{6+} in solutions (and in solids) is that of the dioxo (uranyl) ion UO_2^{2+}. This is true as well for the other hexavalent actinides Np^{6+}, Pu^{6+}, and Am^{6+} (as NpO_2^{2+}, PuO_2^{2+} and AmO_2^{2+}, respectively) (Cotton and Wilkinson, 1980). The uranyl ion is remarkably stable in aqueous solution and can persist through a variety of chemical changes. In both crystalline compounds and in solution the O═U═O group is linear, with the U═O distance ranging from about 16-20 nm (Bombieri and De Paoli, 1985). The ion forms complexes with negative ions and neutral molecules. Crystallographic data show that four, five, or six ligand atoms can lie in the equatorial plane of the O═U═O group; the ligand atoms may or may not be entirely coplanar depending on the circumstances. Planar 5- and 6-coordination in the equatorial plane is most common, and planar 5-coordination best allows rationalization

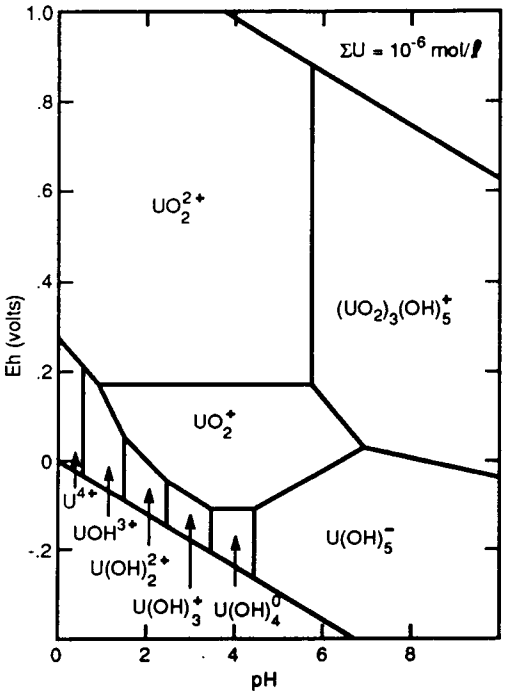

Figure 9-1. Eh-pH diagram showing the relative importance of U^{4+}, U^{5+} (as UO^{+}_{2}), and U^{6+} species at 25°C and ΣU = 10^{-6} M (from Langmuir, 1978)

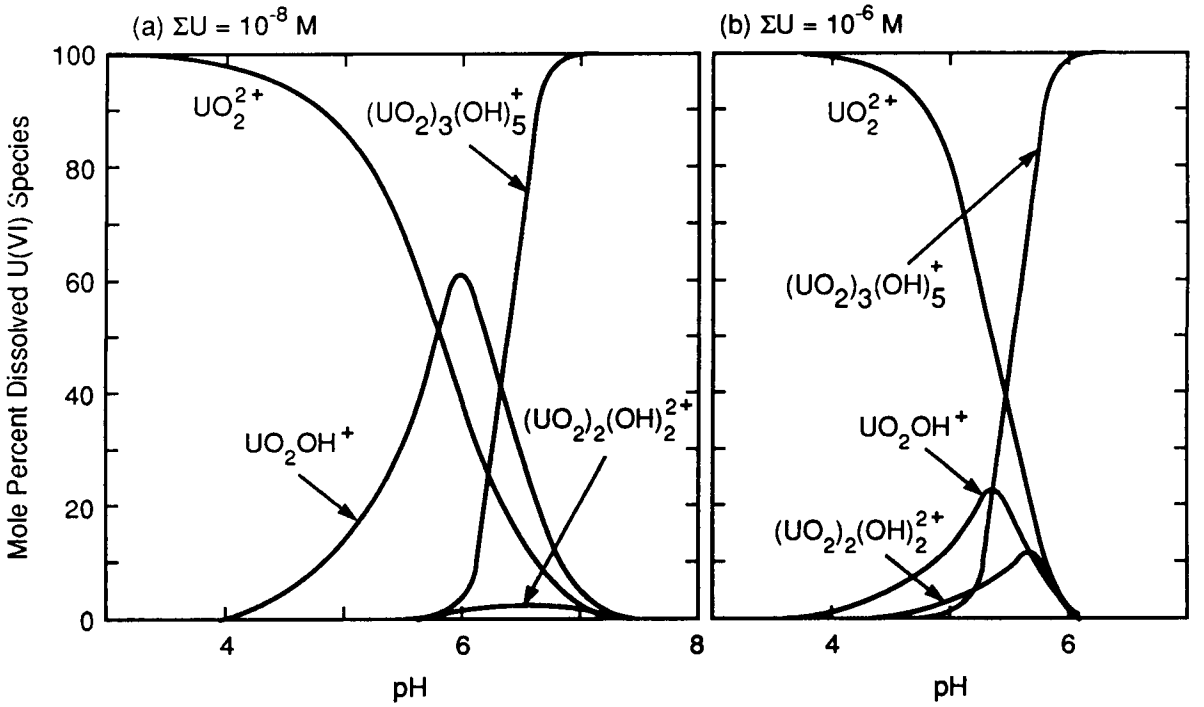

Figure 9-2. Distribution of uranyl hydroxy complexes in pure water at 25°C as a function of pH for: (a) ΣU = 10^{-8} M and (b) ΣU = 10^{-6} M (from Langmuir, 1978)

of a number of hydroxide and other structures, as well as the behavior of polynuclear uranyl ions in hydrolyzed solutions (Cotton and Wilkinson, 1980).

The effects of pH and ΣU on the aqueous speciation of U^{6+} are illustrated in Figure 9-2, which shows the distribution of uranyl hydroxy complexes at 25°C as a function of pH at ΣU = 10^{-8} [Figure 9-2(a)] and 10^{-6} M [Figure 9-2(b)]. The significant species are UO_2^{2+}, UO_2OH^+, $(UO_2)_2(OH)_2^{2+}$ and $(UO_2)_3(OH)_5^+$, based on the thermodynamic evaluation of Langmuir (1978). However, the more recent compilations of Lemire and Tremaine (1980) and Paquette and Lemire (1981) indicate that the species $(UO_2)_3(OH)_7^-$ may be more important than $(UO_2)_3(OH)_5^+$ in basic solutions. The relative importance of the different species varies both with ΣU (as shown in Figure 9-2) and with temperature. Eh-pH diagrams illustrating the relative stabilities of uranium species at various temperatures are given by Paquette and Lemire (1981).

At typical ligand concentrations in groundwater, the most important uranyl complexes are formed with carbonate, phosphate, and fluoride (Langmuir, 1978; Lemire and Tremaine, 1980; Paquette and Lemire, 1981). Under conditions relevant to Yucca Mountain groundwaters, which has bicarbonate as the predominant anion (Kerrisk, 1987), uranyl carbonate complexes may become important at 25°C. Figure 9-3 illustrates the relative stabilities of uranyl hydroxy and carbonate complexes at 25°C as a function of pH. The figure was calculated using a value of p_{CO_2} = 10^{-2} atm (Langmuir, 1978), which is a typical value for groundwaters, and ΣU = 10^{-8} M. Calculations by Langmuir (1978) indicate that carbonate complexes decrease in importance relative to the hydroxy complexes at higher temperatures, although this is not in agreement with the calculations by Paquette and Lemire (1981).

The calculated partial pressures of $CO_2(g)$ in equilibrium with compositions of saturated-zone groundwater from Yucca Mountain vary over a wide range [$10^{-3.8}$ to $10^{-0.8}$ atm (Kerrisk, 1987)]. The effect of p_{CO_2} on uranyl aqueous speciation at 25°C is illustrated in Figure 9-4, which was derived from MINTEQA2 calculations by Payne and Waite (1989). Shown by arrows are the typical values for J-13 waters (Kerrisk, 1987) and waters in equilibrium with atmospheric $CO_2(g)$.

Figure 9-5 compares the uranyl species distribution as a function of ΣU at two values of p_{CO_2}, and shows that the uranium species distribution is relatively independent of ΣU at high p_{CO_2}, but at $CO_2(g)$ partial pressures approaching atmospheric value, ΣU is important in determining U^{6+} speciation.

The dependence of uranium aqueous chemistry on various parameters discussed above has important implications to experimental and modeling studies of uranium sorption. For uranyl sorption experiments, the following parameters must be constrained or known: (a) Eh, (b) pH, (c) concentration of complexing ligands, (d) ΣU, and (e) temperature. Quantitative determination of the effects of these parameters on aqueous speciation requires the use of equilibrium models such as EQ3, PHREEQE, or MINTEQA2 and the requisite databases. An additional parameter that may be important is the concentration of competing cations present in

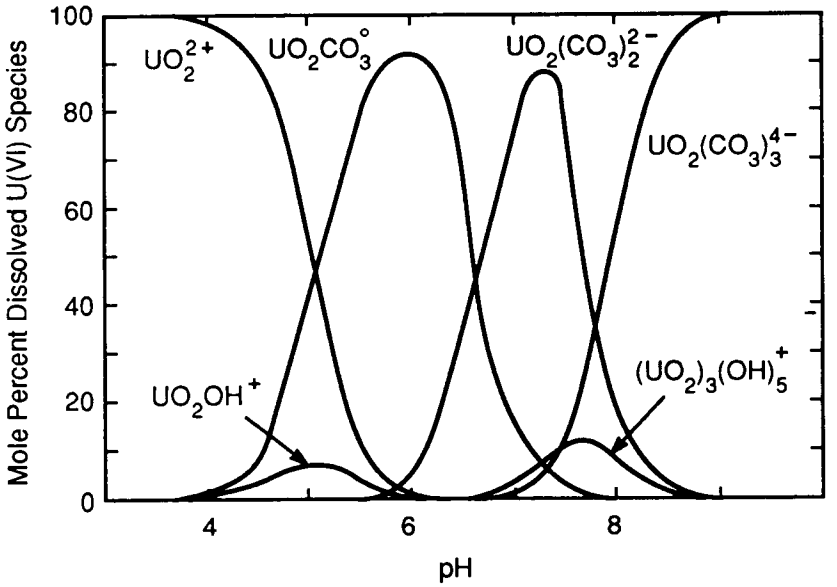

Figure 9-3. Distribution of uranyl hydroxy and carbonate complexes at 25°C as a function of pH for p_{CO2} = 10^{-2} atm (from Langmuir, 1978)

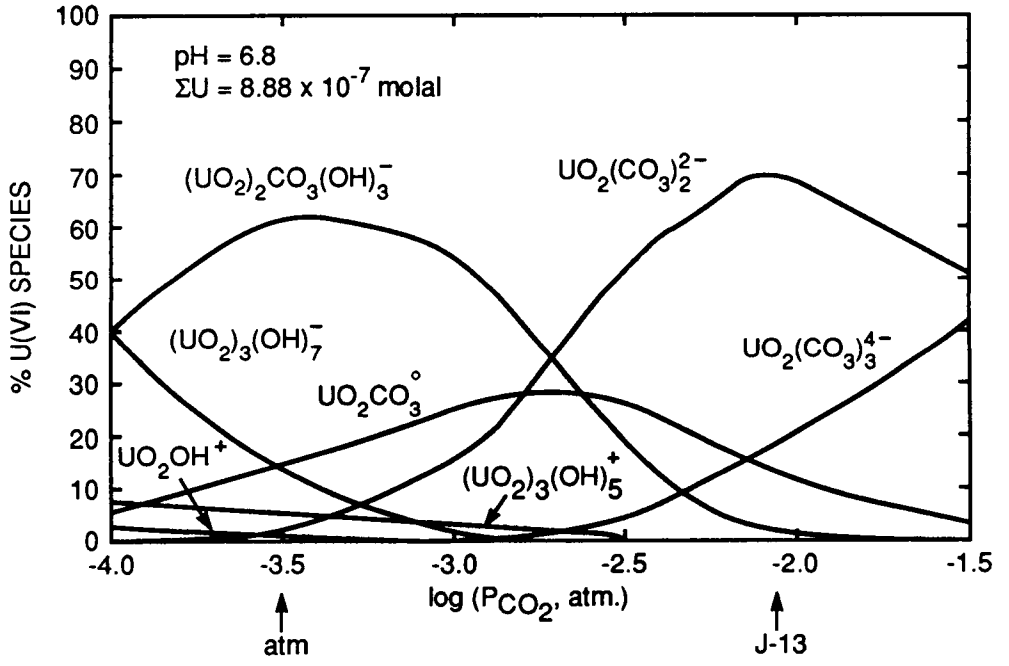

Figure 9-4. Results of MINTEQA2 calculations showing the dependence of U^{6+} aqueous speciation on CO_2(g) partial pressure (from Payne and Waite, 1989)

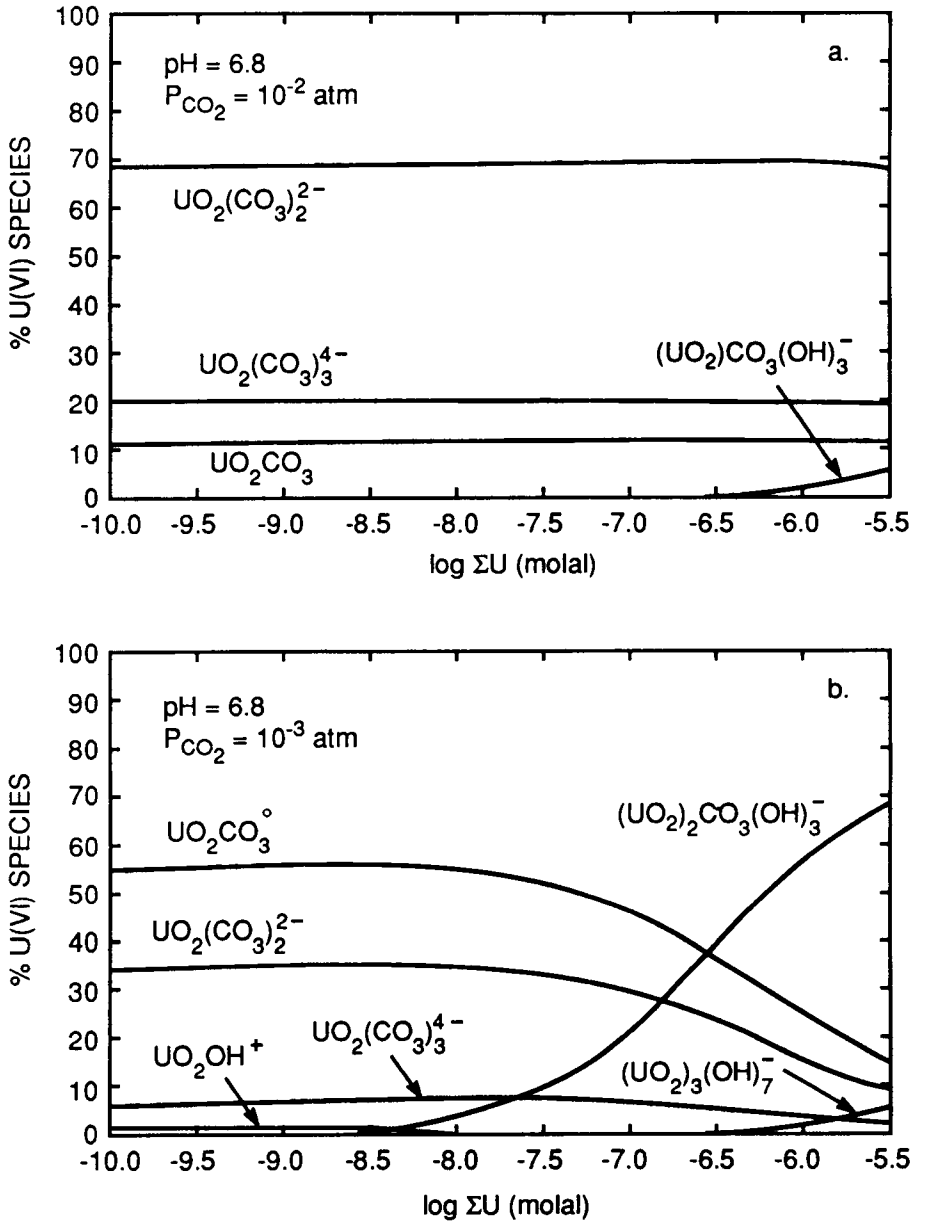

Figure 9-5. MINTEQA2 calculations (T=25°C, pH=6.8) showing the dependence of U^{6+} species distribution on ΣU for p_{CO2} equal to: a) 10^{-2} and b) 10^{-3} atm (from Payne and Waite, 1989)

groundwater, such as Na^+, K^+, Ca^{2+} and Mg^{2+}. Although some experiments indicated that competing cations at concentrations typical of groundwaters do not significantly affect uranyl sorption onto iron oxides and oxyhydroxides (Hsi and Langmuir, 1985), minerals which are strong ion exchangers (such as montmorillonite) have been found to exhibit different selectivities for uranium depending on the exchangeable cation initially present in the mineral (Tsunashima et al., 1981). Of course, the properties of the substrate also affect sorption processes. These properties include surface area, surface charge density, exchange capacity, iso-electric point (IEP) and pH of zero surface charge (PZC). The effects of various parameters on uranyl sorption are illustrated by examples of published experimental data discussed below.

9.3.2. Uranium Sorption Studies on Geologic Media

A literature review indicates that uranium sorption studies have been conducted on a variety of geologic media including iron oxides, hydroxides and oxyhydroxides (Starik et al., 1958; Hsi, 1981; Tripathi, 1984; Hsi and Langmuir, 1985), clays (Schmidt-Collerus, 1967; Tsunashima et al., 1981; Ames et al., 1983, Siegel et al., 1990), organic matter (Szalay, 1964; Schmidt-Collerus, 1967), Ti and Zr oxyhydroxides (Maya, 1982), amorphous silica (Schmidt-Collerus, 1967; Maya, 1982), and zeolites (Katayama et al., 1974; Doi et al., 1975; Ames et al., 1983; Ishihara et al., 1988; Vochten et al., 1990). These studies provide information on the important parameters that influence uranyl sorption. These parameters are listed below, and selected examples are given to illustrate the importance of each parameter in controlling the sorption of uranium.

Effect of pH. Perhaps the most striking feature seen from the available data is the strong pH dependence of uranium sorption. Experimental results on a variety of geologic media indicate a steep increase in uranium sorption within a narrow pH range. This behavior is similar to that of other hydrolyzable metal ions such as Pb^{2+}, Cu^{2+}, Co^{2+}, Zn^{2+}, and Cd^{2+} (Hayes and Leckie, 1986; Honeyman and Leckie, 1986; Yasunaga and Ikeda, 1986). Uranium sorption data are shown in the following figures for a variety of substrates including amorphous iron hydroxide and goethite (Figure 9-6) and zeolites (Figures 9-7, 9-8, and 9-9). The pH range at which the 'adsorption edge' for uranium occurs varies with the type and properties of the substrate, as well as the chemistry of the solution, but in general it occurs in the pH range of 2 to 6.

The increase in amount of sorbed uranium with pH has been interpreted to be due to the adsorption of uranyl hydroxy complexes (Tripathi, 1984; Hsi and Langmuir, 1985; Vochten et al., 1990). A comparison of Figure 9-2 and Figures 9-6 to 9-9 indicates that in the pH range where uranium is most strongly adsorbed, the predominant dissolved uranyl species are UO_2OH^+ and $(UO_2)_3(OH)_5^+$. Thus Hsi and Langmuir (1985) interpreted their sorption data on $Fe(OH)_3$(am) and goethite in terms of adsorption of UO_2OH^+ and $(UO_2)_3(OH)_5^+$ hydroxy complexes. On the other hand, Tripathi (1984) interpreted his own experimental data on goethite by invoking adsorption of a different complex, $UO_2(OH)_3^-$. The detailed experiments by Tripathi (1984) on goethite also demonstrated that the adsorption edge shifts to higher pH's with increasing ΣU and with increasing ionic strength.

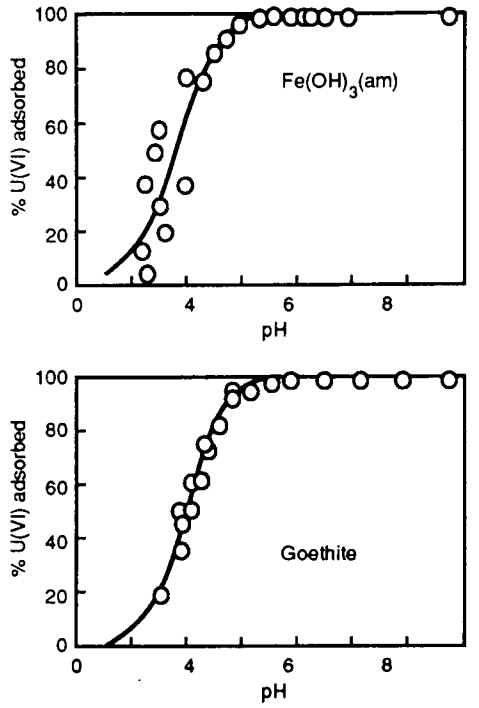

Figure 9-6. Uranium sorption at 25°C vs. pH at $\Sigma U = 10^{-5}$ M in 0.1 M $NaNO_3$. Symbols are experimental data and curves are calculated using a surface complexation model (from Hsi and Langmuir, 1985)

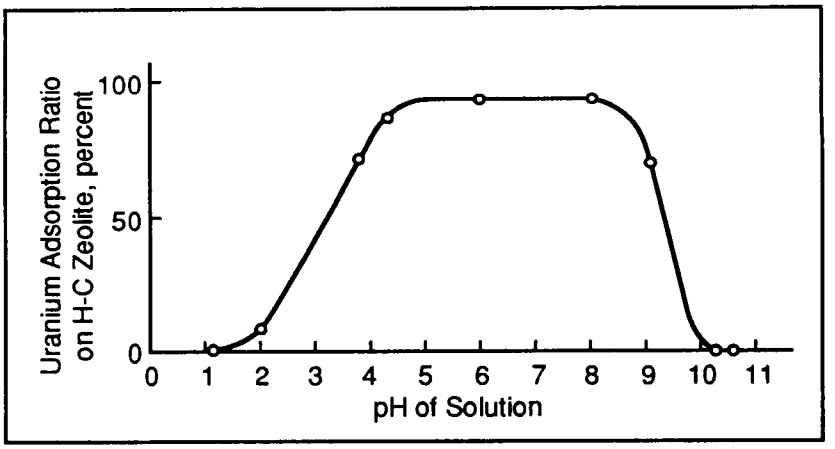

Figure 9-7. Relation between uranium sorption ratio on heulandite-clinoptilolite and solution pH (from Doi et al., 1975)

Effect of Complexing Ligands. Complexing ligands present in groundwater could potentially compete with mineral surfaces in reacting with the solute of interest and therefore decrease the amount of solute sorbed onto the mineral. The effect of carbonate complexation on the sorption behavior of uranium is shown by the data of Hsi and Langmuir (1985) in Figure 9-10. The figure illustrates that uranyl carbonate complexation inhibits uranyl adsorption especially in alkaline solutions. The amount of inhibition is directly proportional to the total dissolved carbonate content (Hsi and Langmuir, 1985). The decrease in uranyl sorption at high pH observed in Figures 9-7 and 9-8 is likely due to the formation of carbonate complexes, since $CO_2(g)$ was not purged from the experimental solutions.

Hsi and Langmuir (1985) interpreted their uranyl-carbonate data in terms of adsorption of the di- and tri-carbonate complexes, $UO_2(CO_3)_2^{2-}$ and $UO_2(CO_3)_3^{4-}$. They considered negligible the adsorption of the mixed hydroxy-carbonate complex, $(UO_2)_2CO_3(OH)_3^-$. In contrast, Tripathi (1984) states that based on his data, some of which are shown in Figure 9-11, almost complete removal of uranium is possible by adsorption on goethite from solutions where the mixed complex $(UO_2)_2CO_3(OH)_3^-$ is the predominant form of U^{6+}, although it is not possible to say whether or not the complex itself adsorbs. Figure 9-11 also shows that the adsorption edge shifts to higher pH with increasing ΣU, a behavior Tripathi also observed for the uranyl-hydroxy system. Note that the effect of varying ΣU on the desorption edge (located on the alkaline pH side of Figure 9-11) is smaller, compared to its effect on the adsorption edge.

A limited set of experiments was also conducted by Tripathi (1984) to evaluate the effects of complexation by fluoride (F^-) and phosphate (HPO_4^{2-}) on uranyl adsorption on goethite. His results for the fluoride-bearing systems indicate that in acidic solutions the formation of uranyl fluoro complexes causes a decrease in the adsorption of uranium. However, in solutions with $pH > 6.5$, the adsorption of uranium approaches that of the fluoride-free system, presumably because uranyl hydroxy complexes become the predominant species under these conditions (Langmuir, 1978). In acidic phosphate-bearing solutions, his results indicate a slight decrease in adsorption of uranium, although as a pH of 6.5 is approached, the difference between adsorption in phosphate-bearing and phosphate-free systems becomes negligible. In addition, under conditions where $UO_2(HPO_4)_2^{2-}$ is calculated to be the predominant uranyl species, almost complete (≈ 100 percent) removal of uranium is possible by adsorption on goethite (Tripathi, 1984).

Effect of ΣU. As discussed previously and shown in Figure 9-2, the relative importance of the different aqueous uranyl species varies with ΣU. Therefore, the adsorption behavior of uranium can be expected to vary also with ΣU. Unfortunately, most experimental studies on uranium sorption have not interpreted the results in terms of the effect of ΣU on uranyl speciation, or did not design the experiments so that other parameters (such as pH) remained constant. A majority of experiments as a function of ΣU were designed to determine distribution coefficients, K_d's. In general, these isotherm experiments were not buffered at a fixed pH, even though the equilibrium pH of aqueous solutions does vary with ΣU. For example, the pH of a 0.0001 g U/liter solution was measured by Rancon (1973) to be 7.6, while

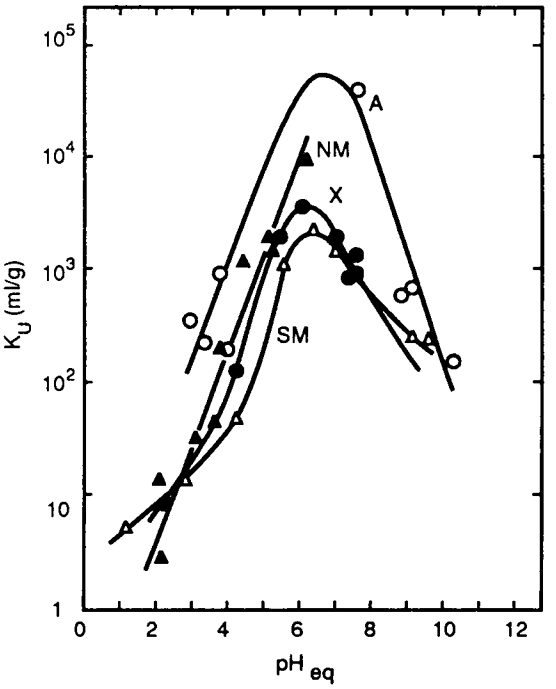

Figure 9-8. Variation of distribution coefficient (K_u) with equilibrium pH (from Ishihara et al., 1988). NM - natural mordenite, SM - synthetic mordenite, A - zeolite A, X - zeolite X.

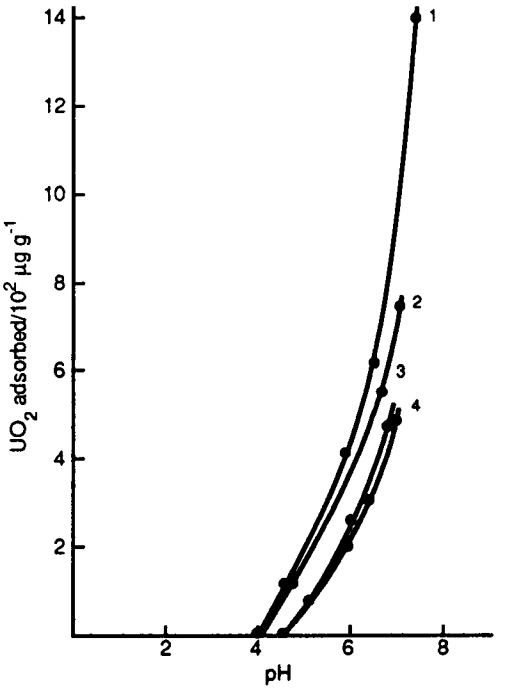

Figure 9-9. Uranium sorption at 25°C vs. pH for: (1) scolecite, (2) chabazite, (3) heulandite, and (4) stilbite (from Vochten et al., 1990)

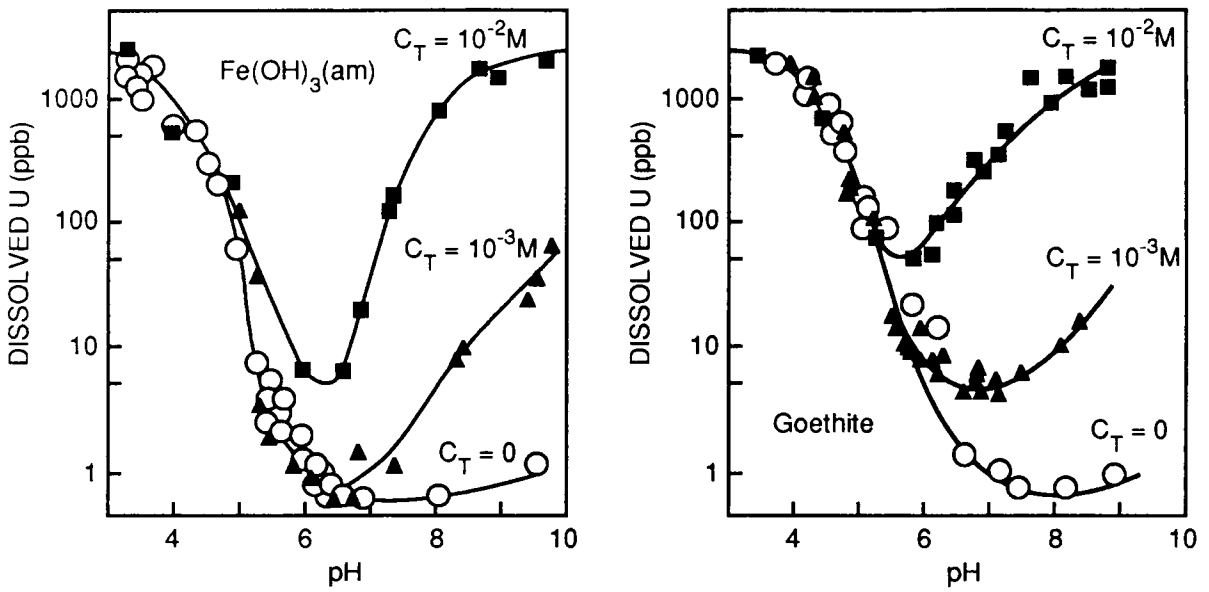

Figure 9-10. Effect of total carbonate concentration (C_T) on uranyl sorption vs pH at 25°C and $\Sigma U = 10^{-5}$ M in 0.1 $NaNO_3$ solutions (from Hsi and Langmuir, 1985)

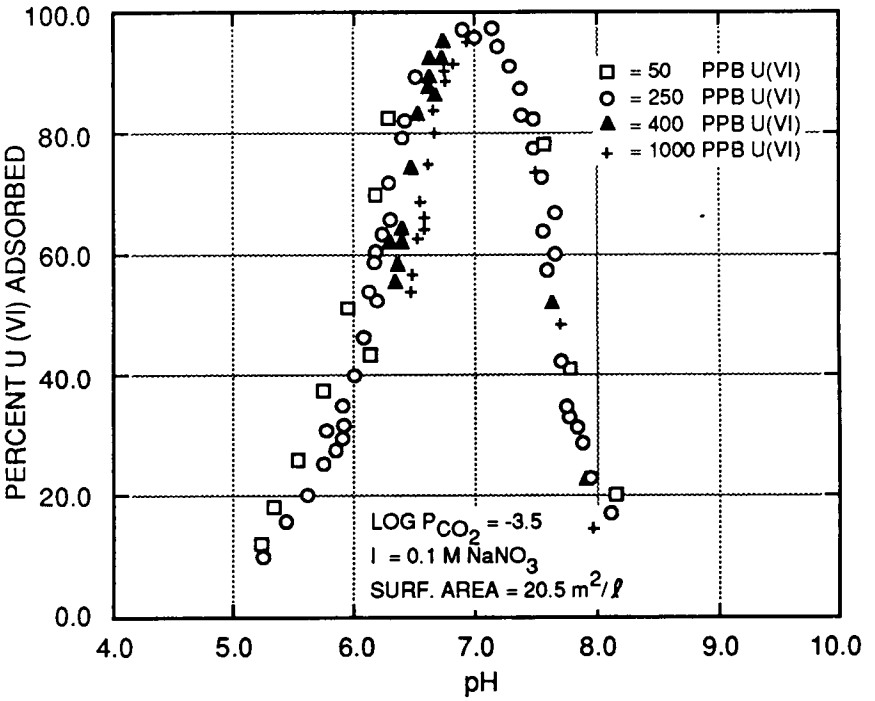

Figure 9-11. Effect of carbonate complexing on uranyl adsorption by goethite (from Tripathi, 1984)

a 1.0 g U/liter solution was measured to be 3.5. Because of the synergistic effects between ΣU, pH, p_{CO_2}, and uranyl speciation and sorption, the results of these isotherm experiments are difficult to interpret and the resulting K_d values are impossible to apply with confidence.

A few studies did constrain the pH while varying ΣU. An example is given in Figure 9-12, which shows uranium adsorption for the zeolite mineral scolecite as a function of total uranium concentration at a pH which was fixed at 7 using a NaH_2PO_4-Na_2HPO_4 buffer (Vochten et al., 1990). The dependence of sorption on pH for this mineral is shown in Figure 9-9. In these experiments, CO_2(g) was purged from the system by using a N_2(g) atmosphere. However, the authors did not offer any interpretation of these data.

Tripathi (1984) measured uranyl sorption on goethite at several values of ΣU and over a range of pH's, both in the presence and absence of carbonate complexing ligands. His results, some of which are shown in Figure 9-11, indicated that with increasing ΣU, the adsorption edge shifts to higher pH, whether or not carbonate is present in the system. Additional studies by Tripathi indicated that with increasing ionic strength, there is a slight but clear shift of the adsorption edge to higher pH's.

Effect of Competing Cations. Some experiments were conducted by Hsi and Langmuir (1985) to evaluate the effects of competing cations on uranyl sorption onto iron oxides in solutions containing 10^{-3} M Ca^{2+} or Mg^{2+}. Their results indicate that at these concentrations of Ca^{2+} and Mg^{2+}, which are typical values for groundwaters, uranyl sorption on iron oxides is not significantly affected. On the other hand, the experiments by Tsunashima et al. (1981) showed that the selectivity of montmorillonite for uranyl depends on the particular exchangeable cation initially present in the clay structure. Figure 9-13 shows their data for sorption involving the monovalent cations Na^+ and K^+, and the divalent cations Ca^{2+}, Mg^{2+}, and Ba^{2+}. Evidently, UO_2^{2+} species are strongly preferred to monovalent cations in montmorillonite, particularly at low concentrations of uranium, but the other divalent cations are preferred by the clay to UO_2^{2+} species. It is possible that where ion exchange is the predominant sorption mechanism[1], such as in the montmorillonite system, uranium sorption is affected by the presence of competing cations. Zeolites, which are strong ion exchangers, may potentially exhibit similar behavior with regard to uranium sorption, unless surface (as opposed to intracrystalline) adsorption is the predominant mechanism due to the large size of the uranyl species relative to the zeolite 'pores' (Vochten et al., 1990).

Effect of Temperature. Almost all experiments on uranium sorption have been conducted at or near 25°C. However, because of the strong dependence of the aqueous speciation of uranium on temperature (Langmuir, 1978; Lemire and Tremaine, 1980), its

---

[1]For the purposes of this discussion, an ion exchange reaction is defined as a specific type of sorption reaction where an aqueous ion replaces enough ions occupying exchange sites to result in no change in the surface or intracrystalline charge. An adsorption reaction is defined as any reaction between solute and surface site(s) without such constraint (Kent et al., 1988).

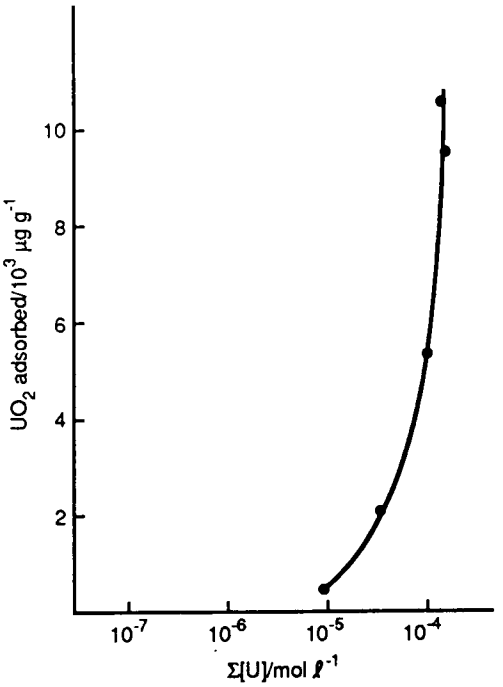

Figure 9-12. Uranyl adsorption at 25°C on scolecite vs. ΣU. The pH was constrained at 7 using a $NaH_2PO_4Na_2HPO_4$ buffer (from Vochten et al., 1990).

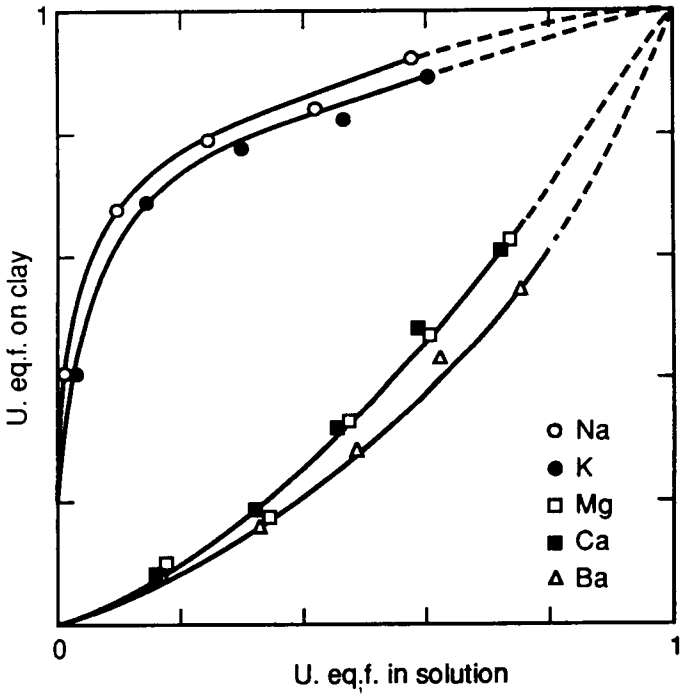

Figure 9-13. Uranyl adsorption on montmorillonite plotted in terms of equivalent fractions of uranium on clay vs. in solution (from Tsunashima et al., 1981). Total normality = 0.002 N.

sorption behavior can be expected to exhibit similarly strong dependence on temperature. This is indicated by the data of Ames et al. (1983) on uranium sorption on clays and other secondary minerals at temperatures of 5, 25, and 65°C. Unfortunately, their interpretation of the data was limited to fitting isotherm equations. A more mechanistic understanding of uranium sorption at various temperatures would require more extensive experiments and thorough evaluation of the thermodynamic properties of uranium species at the temperatures of interest.

Effect of Substrate Surface Area. The work by Tripathi (1984) appears to be the only one that closely studied the effect of substrate surface area on uranyl sorption. His results for uranyl sorption on goethite from carbonate-containing aqueous solutions are shown in Figure 9-14. The figure shows that the adsorption-desorption edges at higher surface areas enclose those at lower surface areas. In other words, with increasing surface area, the adsorption edge moves to a lower pH, while the desorption edge shifts to a higher pH. The behavior of the adsorption edge in carbonate-free systems is the same, i.e., it shifts to more acidic pH's with increasing surface area.

9.3.3. Sorption Models

Different models of varying complexity have been used in the literature to represent in mathematical form the sorption of uranium on geologic media. These include sorption isotherms (e.g., linear, Freundlich, Langmuir, Dubinin-Radushkevich isotherms) and surface complexation models. It is beyond the scope of this report to review these different models and therefore only brief discussions are included here. Details are given in references cited (e.g., Sposito, 1984; Kent et al., 1988).

Isotherm equations are generally used to fit experimental data on equilibrium concentrations of the solute in the solid and aqueous phases (e.g., Tsunashima et al., 1981; Ames et al., 1983). The use of sorption isotherms, however, has several limitations. First, sorption isotherms are valid only at low solute concentrations. Second, isotherm equations do not explicitly account for the effects of pH, redox conditions, ionic strength, complexation and competitive sorption. In addition, sorption mechanisms are either assumed or ignored when isotherm equations are used to represent experimental data. Thus, empirical fits to sorption data using isotherm equations are strictly valid only for the specific experimental conditions under which the data were determined. As discussed in the preceding sections, sorption of uranium on geologic media depends on a variety of physical and chemical parameters. This places severe constraints on the use of isotherms in modeling uranium sorption, particularly for systems with widely varying physicochemical conditions.

On the other hand, surface complexation models consider adsorption to take place at defined coordination sites, which can be acidic (positive), amphoteric (neutral), or basic (negative). It allows for adsorption of anions, cations, and neutral species, and explicitly accounts for the aqueous speciation of the solute. The model treats the adsorbent as one of the array of potential ligands that compete with one another for the solute; thus, adsorption reactions can be described quantitatively by mass action equations, which makes possible integration of

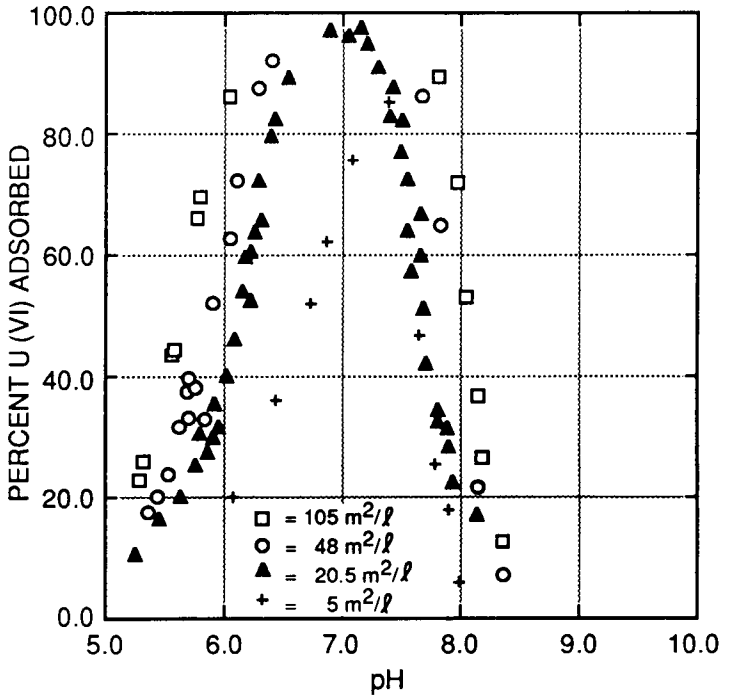

Figure 9-14. Effect of varying goethite surface area on uranyl sorption. $\Sigma U = 10^{-5.98}$ M; $p_{CO2} = 10^{-3.5}$ atm; I=0.1 M $NaNO_3$; surface area=5 to 105 m^2/l (from Tripathi, 1984)

sorption processes into geochemical equilibrium computer codes. The major disadvantage of surface complexation models is the large number of parameters required, and which must be determined for each rock type and solute of interest. However, applied judiciously, the surface complexation approach yields a set of parameters that are valid over a range of solution compositions and solute concentrations.

The surface complexation approach has been applied to modeling of uranyl sorption on iron oxides by Hsi and Langmuir (1985) and Tripathi (1984). Comparisons of experimental and calculated values derived by Hsi and Langmuir (1985) are shown in Figure 9-6. An example from Tripathi's work in carbonate-bearing systems is shown in Figure 9-15. In this example, the model calculations (shown by the solid curve) used the parameters derived for the carbonate-free systems, i.e., adsorption of uranyl carbonate complexes was not included.

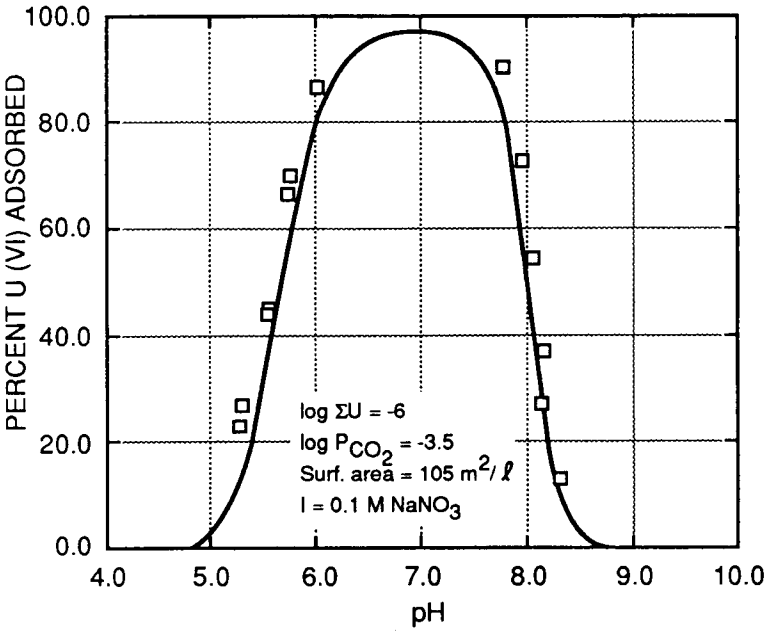

Figure 9-15. Experimental data on uranyl sorption on goethite compared with values calculated from surface complexation model (from Tripathi, 1984). The model used excluded adsorption of uranyl carbonate complexes.

9.3.4. Proposed Work Plan for Experimental Studies on Uranium Sorption on Geologic Media

Based on information derived from the literature review, a work plan to conduct uranium sorption experiments was developed and submitted to NRC for review and approval. The initial focus of the proposed study is uranyl sorption on zeolite minerals, particularly clinoptilolite. Some studies on Japanese uranium ore deposits in sedimentary rocks indicated the importance of sorbing phases like clinoptilolite in 'trapping' uranium (e.g., Doi et al., 1975). For example, the uranium in the Tsukiyoshi, Japan ore deposit occurs mainly as species sorbed on heulandite-clinoptilolite (Katayama et al., 1974). Because the presence of laterally-extensive zones of zeolitized tuff at Yucca Mountain might provide a significant contribution to the geologic barrier for radionuclide transport, it is important to have an understanding of the factors that control radionuclide sorption on zeolite minerals. However, the few studies that have looked at uranium sorption on clinoptilolite (Katayama et al., 1974; Doi et al., 1975; Ames et al., 1983) have been conducted under experimental conditions that are restricted in range or that are insufficiently constrained to provide adequate information on the sorption mechanisms.

The lack of uranium sorption data on well-characterized clinoptilolite specimens under well-constrained experimental conditions makes the role of sorption on clinoptilolite in retarding uranium migration difficult to assess. The recent work by Vochten et al. (1990) on zeolites including heulandite, which is isostructural with clinoptilolite (Gottardi and Galli, 1985), appears to be the first sorption study on zeolites to correlate observed sorption behavior with aqueous speciation of uranium. The proposed experiments will be designed to understand the effects on uranyl sorption of various parameters, including: (1) sorption kinetics and reversibility; (2) pH; (3) ΣU; (4) carbonate complexation; (5) competing cations; (6) rock/water ratio and surface-area/water ratio; and (7) dynamic conditions (column experiments). The results of the experiments will be analyzed in conjunction with speciation modeling using geochemical codes such as EQ3/6, PHREEQE, or MINTEQA2. Sorption data will also be modeled using various approaches, including surface complexation. These will aid in understanding the sorption mechanism(s) involved and in extrapolating the results to geochemical conditions pertinent to the Yucca Mountain environment.

The use of single minerals in studying the sorption behavior of uranium allows detailed investigations on the effects of other physical and chemical parameters. However, it is recognized that the rocks at Yucca Mountain are heterogeneous mixtures of various minerals; ultimately, it is the sorption properties of these rocks that need to be understood. Although attempts have been made to estimate whole rock sorption by proportionally summing the values measured separately in the same solution for each mineral in the rock, this simple sorption additivity approach has been shown to have limited validity (Honeyman, 1984; Altmann, 1984). In addition, this approach has not been applied to tuffaceous rocks typical of Yucca Mountain. Thus, included in the workplan are experiments using artificial mixtures of zeolites with other minerals. These experiments will use minerals for which sorption data are available, such as goethite, hematite, and montmorillonite. The application of sorption additivity or other methods to predict rock sorption properties will be investigated.

9.4. COUPLED HYDROGEOCHEMICAL MODELING

Numerical codes that couple geochemical and transport models (hydrogeochemical models) have seen increasing use as tools for gaining insight into retardation processes and predicting the nature and extent of contaminant transport. Development of such comprehensive codes is being actively pursued by a number of research groups (LANL, LBL, PNL, SNL, EPRI) using a variety of approaches. An evaluation of existing codes should consider accuracy, efficiency, flexibility, and computational requirements among other characteristics in an attempt to find the best balance between model completeness and applicability.

9.4.1. Selection Criteria

The criteria used to select a code for investigating sorption processes are similar to those used for selecting any computer program for a desired purpose. These include program flexibility, computational efficiency and accuracy, ease of input and output,

computational requirements and run costs, and database requirements and availability. These will be discussed in turn below.

In order to evaluate sorption processes involved in the retardation of contaminant transport, a code needs to be flexible in terms of the sorption models (K_d, Empirical Isotherms, Ion Exchange, Surface Complexation, etc.) available to the modeler. Solute transport codes (TRACR3D, NEFTRAN II) frequently neglect sorption processes, and deal with sorption using only a retardation factor (R_f). Coupled hydrogeochemical codes ideally offer a more complete selection, and will be able to incorporate a wide variety of data types as they become available. In addition, in order to use numerical modeling as a predictive tool, a code should include sorption models valid for a given approach to solute transport (e.g., the conservative K_d approach of Meijer, 1990).

Because the system of interest is perhaps poorly understood, the hydrogeochemical model should not be designed with only one system in mind. Ideally, a variety of boundary and initial conditions should be available, and the model should be able to describe a variety of physical systems (homogeneous/heterogeneous, steady-state/transient, isotropic/anisotropic, isothermal/ nonisothermal, etc.) as more complete information becomes available. Flexibility is also important in order to perform sensitivity analyses of the system to various parameters (Siegel, 1989).

The efficiency of a given hydrogeochemical model is not only important for investigating the problem at hand, but it will also determine the ability of the program to be adapted to more complete (and complex) conceptual models. This efficiency in turn depends on both the approach taken toward coupling and the primary dependent variables (PDVs) that are chosen to represent the problem of interest (Kirkner and Reeves, 1988; Reeves and Kirkner, 1988; Yeh and Tripathi, 1989). Essentially two approaches have been used to couple geochemical equilibria and transport models. Direct (one-step) coupling (Rubin and James, 1973; Valocchi et al., 1981) involves insertion of the nonlinear, algebraic equations describing equilibrium geochemistry into the transport partial differential equations. This results in a set of nonlinear partial differential equations (PDE) that are solved simultaneously for geochemistry and transport for a given set of PDVs. For the second method, geochemistry and mass transport equations are posed independently of one another, and solved sequentially rather than simultaneously. This two-step approach has been used successfully in several studies (Cederberg et al., 1985; Walsh et al., 1982). While one-step coupling is a more exact solution to the problem, the coefficient matrix must be reformulated for each iteration, leading to extensive computer calculation time and memory requirements (Cederberg, 1985). Alternatively, two-step coupling requires the solution of only one set of equations in sequence, and uses computer resources much more effectively. Calculations (Cederberg, 1985; Yeh and Tripathi, 1989) indicate that a two-step coupling approach is more than 30 percent faster than direct coupling for a given problem. In addition, Yeh and Tripathi (1989) show that only a two-step approach will be able to model larger two- and three-dimensional problems, given likely limits on computer computation and memory storage in the foreseeable future. Numerical techniques employed in matrix formulation and solution, and iteration will also have an effect on run time,

and therefore, run costs. Several studies (Yeh, 1985; Reeves and Kirkner, 1988; Yeh and Tripathi, 1989; Siegel, 1989) have evaluated a variety of iterative techniques (successive overrelaxation, Gauss-Seidel, Picard iteration, etc.) and identified convergence problems. On a mainframe computer, run costs can amount to many thousands of dollars for a single 10,000-year simulation on a scale similar to Yucca Mountain (Siegel, 1989).

Thermodynamic data is of critical importance in modeling any geochemical system. A given hydrogeochemical code should use an established, current database that has been tested for accuracy and internal consistency, and is broad enough to include a relatively complete set of species, minerals, and complexes that are likely to be encountered in the geologic environment of interest (Kincaid et al., 1984; Krupka et al., 1988). In addition, the necessary data for modeling important processes (sorption, precipitation/dissolution, ion exchange, activity, etc.) should be available. The database should be able to incorporate both updated information and additional data as needed for a given system. A readily available, public domain database will have additional advantages of being tested through application to a wide variety of problem applications, and a general interest in keeping the database current. Finally, the complete database should be readily accessible to the program in order to adapt the model to a variety of systems.

Although the degree of "user-friendliness" is unlikely to affect the accuracy or efficiency of a program, it should be considered in code selection (Siegel, 1989). Complicated or awkward formatting of input decks can make application of the model difficult, and limit its usefulness as a tool to study a wide variety of systems or perform sensitivity analyses. Rigid input can also inhibit modification or correction of the input, perhaps leading to false starts and inaccurate data entry. Because these codes deal with potentially large numbers of chemical species and long time-intervals and distances, post-processing of the data is also important as an aid in interpreting the output from the hydrogeochemical model.

9.4.2. Codes Considered

Subtask 1.1 is not intended to be an exhaustive analysis of reactive transport codes. Many codes (Rubin and James, 1973; Valocchi et al., 1981; Walsh et al., 1982) are unnamed and were developed for a particular problem. Several elaborate codes that currently exist require extensive supercomputer time (DYNAMIX, Liu and Narasimhan, 1989a,b; Barry, 1990), and are not considered in this discussion. In addition, future modeling will likely include stochastic methods and parallel processing (Barry, 1990), developments which are not considered here. Table 9-1 is a list of models considered to date under Subtask 1.1. Information about the code characteristics and the techniques used was largely collected from user's manuals and key references listed in the table, and additional information is available in Morrey et al. (1986), Siegel (1989) and Mangold and Tsang (1991). Two of the codes (NEFTRAN II and TRACR3D) are solute transport codes that do not explicitly account for the geochemistry of the water/rock system. The remainder of the codes are hydrogeochemical models. All codes are written in FORTRAN. With the exception of CHMTRNS, all of the codes are isothermal, equilibrium models, and do not currently incorporate reaction kinetics. It is also important to note that

hydrogeochemical modeling is a dynamic area of research, and future developments may result in new, more powerful codes, or extensive modification to the existing models.

The TRANQL code was developed at Stanford University, and has been used to model multicomponent transport of Cd, Co, Br, and Cl (Cederberg, 1985; Cederberg et al., 1985). The code is based on the transport code ISOQUAD (Pinder, 1976) and MICROQL (Westall, 1979), a scaled-down version of the MINEQL code. TRANQL has been evaluated by Siegel (1989). The model is currently designed for one-dimensional simulation employing a mainframe computer system. The current system is able to model ion exchange and surface complexation sorption processes, but cannot handle precipitation/dissolution reactions. Pre- and post-processing routines have been developed to facilitate data entry and interpretation (Grover and Greyberg, 1987). The code is currently limited to a maximum of two mobile components and one sorbing substrate. Siegel (1989) concluded that code flexibility is limited by its database, and to simulate the transport of a single solute a distance of 5 km over 10,000 years would amount to $10,000 to $40,000 in run time costs.

The FASTCHEM system (Hostetler and Erikson, 1989; Hostetler et al., 1989) was developed by Pacific Northwest Laboratory (PNL) for the Electric Power Research Institute (EPRI), and is based on the SATURN transport code and the MINTEQ geochemical code (Morrey et al., 1986). The program is modular in design, and incorporates a networked PC workstation for constructing input files to an online mainframe computer for transport and geochemical calculations. Post-processing of the output is performed on the mainframe for subsequent downloading and graphic display at the workstation. The code uses a modified version of the MINTEQA2 data base and is valid for the temperature range 25° to 100° C (Criscenti et al., 1989; Krupka et al., 1988). A Markov hydrological model is used to simulate solute movement through advection, diffusion, and hydrodynamic dispersion (Kincaid, 1988). This method involves discretizing a streamtube into a number of arbitrarily shaped bins. The total concentration of each solute in each bin is then expressed as an entry in a state vector, and the Markov transition matrix is used to predict the evolution of the state vector through time. Two-step coupling of geochemistry and transport is used for efficient computation. Only longitudinal dispersion is modeled, and a series of parallel, one-dimensional, noninteracting streamtubes is used to model two- and three-dimensional systems. FASTCHEM is able to model saturated/ unsaturated systems, heterogeneities, anisotropy and transient conditions. Geochemical processes include speciation, complexation, oxidation/reduction, and several different adsorption models (K_d, empiricial isotherms, ion exchange, surface complexation). Activity relationships are modeled using the Davies or the extended Debye-Huckel equations. The code is proprietary, and the licensing fee is currently set at $50,000.

The Coupled Transport Model (CTM) code (Morrey and Hostetler, 1985; Erikson et al., 1990) is currently in development at PNL for the Low-Level Waste Management Division of the NRC, and incorporates many of the same methods and approaches as the proprietary FASTCHEM code. The database is the same as the FASTCHEM code, with further modifications to include the compilations of Wagman et al. (1982) and the uranium data of Tripathi (1984). The current version of the code has only been set up for one-dimensional

Table 9-1. HYDROGEOCHEMICAL AND SOLUTE TRANSPORT COMPUTER MODELS

	TRANQL	FASTCHEM	CTM	CHEMTRN	CHMTRNS	NEFTRAN II	TRACR3D
Reference(s)	Cederberg (1985)	Hostetler et al. (1989)	Erikson et al. (1990)	Miller and Benson (1983)	Noorishad et al. (1987)	Olague et al. (1991)	Travis (1984)
Affiliation	Stanford	EPRI	PNL	LBL	LBL	SNL	LANL
Proprietary	No	Yes	No	No	No	No	No
Speciation	Yes	Yes	Yes	Yes	Yes	No	n.a.
Complexation	Yes	Yes	Yes	Yes	Yes	n.a.	n.a.
Precipitation/ Dissolution	No	Yes	Yes	Yes	Yes	No	No
Sorption Options	SC, IE	SC, IE, Constant K_d, K_d isotherm	SC, IE, Constant K_d, K_d isotherm	SC, IE, K_d	SC, IE	R_f	R_f
Number sorbing species/run	2	40 Max.	>1	>1	>1	Limited by CPU Memory	Limited by CPU Memory
Sorption Options/run	1	>1	>1	>1	>1	1	2
Isothermal/ Nonisothermal	Isothermal	Isothermal	Isothermal	Isothermal	Isothermal/ Nonisothermal	Isothermal	Isothermal

Abbreviations: **n.a.** - not applicable; **EPRI** - Electric Power Research Institute; **PNL** - Pacific Northwest Laboratories; **LBL** - Lawrence Berkeley Laboratory; **SNL** - Sandia National Laboratory; **LANL** - Los Alamos National Laboratory; **SC** - Surface Complexation; **IE** - Ion Exchange; **R_f** - retardation factor; **Davies** - Davies equation; **D-H** - Debye-Huckel; **T** - transverse dispersion; **L** - longitudinal dispersion; **FEM** - finite element method; **FDM** - finite difference method; **ADE** - advection-dispersion equation

Table 9-1. HYDROGEOCHEMICAL AND SOLUTE TRANSPORT COMPUTER MODELS (Cont'd)

	TRANQL	FASTCHEM	CTM	CHEMTRN	CHMTRNS	NEFTRAN II	TRACR3D
Activity Coefficients	No	Yes-Davies Extended D-H	Yes-Davies Extended D-H	Yes-Davies	Yes-Davies	n.a.	n.a.
Kinetics	No	No	No	No	Yes	No	n.a.
Current Geochemical Database	MICROQL [Simplified MINEQL]	ECHEM/EICM Krupka et al.(1988)	Mod.MINTEQ (Krupka et al., 1988); Tripathi(1984)	WATEQ2; Benson and Teague (1980)	WATEQ2; PHREEQE; Rimstidt and Barnes (1980) Benson and Teague(1980)	n.a.	n.a.
Dimensions	1,2	Parallel 1-D stream-tubes	Parallel 1-D stream-tubes	Parallel 1-D stream-tubes	Parallel 1-D stream tubes	Pseudo 3-D	1,2,3
Velocity	Constant	Variable	Variable	Can vary systematically	Can vary systematically	Distributed Velocity	Variable
Dispersion	T,L	L	L	L	L	L	T,L
Homogeneous/ Heterogeneous	Homogeneous	Heterogeneous	Heterogeneous	Homogeneous	Homogeneous	Heterogeneous	Heterogeneous
Coupling Steps	Two-Step	Two-Step	Two-Step	One-Step	One-Step	n.a.	Two-Step (pseudo)
Numerical Procedure	Falerkin FEM-Determ. ADE	FEM-Determ. ADE	FEM-Determ. ADE	Backward Diff. FDM-Determ. ADE	Backward Diff. FDM-Determ. ADE	Analytical; Distributed Velocity Method	Implicit FDM

Abbreviations: **n.a.** - not applicable; **EPRI** - Electric Power Research Institute; **PNL** - Pacific Northwest Laboratories; **LBL** - Lawrence Berkeley Laboratory; **SNL** - Sandia National Laboratory; **LANL** - Los Alamos National Laboratory; **SC** - Surface Complexation; **IE** - Ion Exchange; $\mathbf{R_f}$ - retardation factor; **Davies** - Davies equation; **D-H** - Debye-Huckel; **T** - transverse dispersion; **L** - longitudinal dispersion; **FEM** - finite element method; **FDM** - finite difference method; **ADE** - advection-dispersion equation

Table 9-1. HYDROGEOCHEMICAL AND SOLUTE TRANSPORT COMPUTER MODELS (Cont'd)

	TRANQL	FASTCHEM	CTM	CHEMTRN	CHMTRNS	NEFTRAN II	TRACR3D
Efficient for Multiple Runs	No	Yes	Yes	No	No	Yes	No
Current Computer Requirements	VAX Mainframe IBM 3081	IBM PC Input to IBM Mainfram	IBM PC (Model 70)	7600 CDC	7600 CDC CRAY	VAX Mainframe	CRAY at LANL
Graphics Postprocessing	No	Yes	Yes	No	No	No	Yes
Preprocessor	Yes	Yes	Yes	Formatted Batch	Formatted Batch	No	No

Abbreviations: **n.a.** - not applicable; **EPRI** - Electric Power Research Institute; **PNL** - Pacific Northwest Laboratories; **LBL** - Lawrence Berkeley Laboratory; **SNL** - Sandia National Laboratory; **LANL** - Los Alamos National Laboratory; **SC** - Surface Complexation; **IE** - Ion Exchange; **R_f** - retardation factor; **Davies** - Davies equation; **D-H** - Debye-Huckel; **T** - transverse dispersion; **L** - longitudinal dispersion; **FEM** - finite element method; **FDM** - finite difference method; **ADE** - advection-dispersion equation

simulations. While the CTM code is currently designed to run on an IBM PS/2 Model 70, future developments for modeling 2- and 3-dimensional systems may require mainframe capabilities. Pre- and post-processing are available for data input and output through an interactive system. Output is designed to take advantage of several graphics software packages currently available for the PS/2 system (SURFER and GRAFIX).

The CHEMTRN code was developed at Lawrence Berkeley Laboratory (LBL), and has been applied to nuclear waste isolation and contaminant transport (Miller and Benson, 1983). The code uses the one-step direct coupling method, and is therefore more cumbersome than the two-step codes discussed above. CHEMTRN is an equilibrium code, and is similar to FASTCHEM/CTM in that it employs a one-dimensional streamtube to model fluid flow. Due to the one-step coupling, however, storage limitations will become a problem in extending the model to multiple dimensions. The code is able to model ion exchange, surface complexation, and precipitation/dissolution reactions as retardation mechanisms. The model is limited to saturated flow through a homogeneous porous medium at constant temperature. In applications to date, the model has not employed an extensive, established thermodynamic database. It does appear that data can be included from a variety of sources, but a database would have to be developed and modified for extensive use of this code.

The CHMTRNS code was also developed at LBL (Noorishad et al., 1987), and represents a version of CHEMTRN that has been modified to include reaction kinetics, carbon isotope fractionation, and nonisothermal behavior. Multiple sorption models can be used in a given run. Formatted batch input is used for defining the problem and inputting the initial and boundary conditions. Each input deck consists of a minimum of twenty "cards," each card consisting of from one to seven parameters. Although the elaborate input makes the code flexible enough for application to a variety of systems and situations, many of the parameters must be defined by the user, leading to complex data input. In addition, much of the thermodynamic, kinetic and sorption data must be entered each time the model is run, limiting the ability of the code to perform multiple runs for sensitivity analysis. No pre- or post-processing of the data is currently available to help in data entry or interpretation. It is assumed that data entry for CHEMTRN is similar.

NEFTRAN II (Olague et al., 1991) and TRACR3D (Travis, 1984) are solute transport codes and do not explicitly consider the geochemical equilibria involved in contaminant migration. As such, they are not suitable for examining specific sorption processes. However, because the bulk of the calculation time involved in modeling reactive solute transport is spent calculating the geochemistry, solute transport codes are much quicker. They can therefore be adapted to model three-dimensional transport, radionuclide decay, and fractured media transport without overextending computer resources. In addition, they can be more finely discretized and the physical aspect of solute transport can be examined in more detail.

9.4.3. Code Selection

On the basis of this evaluation, the CTM code has been chosen for further investigation. Although it is perhaps not as powerful as other available codes (CHMTRNS, DYNAMIX), it offers a number of features which make it an attractive alternative. It is similar to FASTCHEM in its construction, while avoiding the licensing costs of FASTCHEM ($50,000). The two-step coupling approach is employed by the CTM model, allowing the code to solve for reactive solute transport more efficiently than the one-step coupling approach used in CHEMTRN and CHMTRNS. Computer costs are minimal because the code has been adapted to the IBM PS/2 Model 70 personal computer system. Also, since the Markov hydrological approach only requires a velocity flow field, it is not, in theory, specific to any particular transport code. This flexibility offers the possibility for adapting the CTM model to more sophisticated transport models in the future. The thermodynamic database is based on the widely available MINTEQ geochemical code, which has been modified (Krupka et al., 1988) and extended to include the uranium data of Tripathi (1984). In addition, several sorption mechanisms are available for evaluating sorption processes involved in a variety of systems. The interactive pre-processing system will simplify modification of the conceptual model and allow for flexible application of the model. Post-processing has been used to adapt the code to SURFER and GRAFIX graphics software (C. Hostetler, personal communication), permitting a variety of data display methods. Although the code has been developed only for equilibrium geochemistry, kinetic data is currently limited or nonexistent for many of the species that are of interest in radionuclide migration, and under certain conditions.

The CTM code is being developed for the NRC (Erikson et al., 1990) and a preliminary version will be made available to CNWRA for initial adaptation and modeling studies. Because the code is in development, documentation is currently limited, although a release to the International Groundwater Modeling Center is anticipated in the fall of 1991 (C. Hostetler, personal communication).

9.5. REFERENCES

Allard, B. 1982. Solubilities of actinides in neutral or basic solutions. In: Edelstein, N. M. (ed.), *Actinides in Perspective*. Pergamon Press, 553-580.

Altmann, S. A. 1984. *Copper Binding in Heterogeneous, Multicomponent Aqueous Systems: Mathematical and Experimental Modeling*. Ph.D. Dissertation, Civil Engineering Department, Stanford University, Stanford, CA, 188 p.

Ames, L. L. Jr., J. E. McGarrah, and B. A. Walker. 1983. Sorption of trace constituents from aqueous solutions onto secondary minerals. I. Uranium, *Clays and Clay Minerals*. 31, 321-334.

Barry, D. A. 1990. Supercomputers and their use in modeling subsurface solute transport. *Rev. Geophys. 28:* 277-295.

Benson, L. V. and L. S. Teague. 1980. *A Tabulation of Thermodynamic Data for Reactions Involving 58 Elements Common to Radioactive Waste Package Systems.* Lawrence Berkeley Laboratory, LBL-11448.

Bombieri, G. and G. De Paoli. 1985. Structural aspects of actinide coordination chemistry, In: Freeman, A. J. and Keller, C. (eds.), *Handbook on the Physics and Chemistry of the Actinides.* North-Holland Physics Pub., Amsterdam, p. 75-142.

Cederberg, G. A. 1985. *TRANQL: A Ground-Water Mass-Transport and Equilibrium Chemistry Model for Multicomponent Systems.* Unpub. Ph.D. Dissertation, Stanford Univ., 117 p.

Cederberg, G. A., R. L. Street, and J. O. Leckie. 1985. A groundwater mass transport and equilibrium chemistry model for multicomponent systems. *Water Resourc. Res. 21:* 1095-1104.

Cotton, F. A. and G. Wilkinson. 1980. *Advanced Inorganic Chemistry.* John Wiley, New York.

Criscenti, L. J., M. L. Kemner, R. L. Erikson, C. J. Hostetler, J. R. Morrey, and J. S. Fruchter. 1989. *The FASTCHEM™ Workstation for Integrating Pre- and Postprocessing Functions.* Electric Power Research Institute, EPRI-EA-5871.

Doi, K., S. Hirono, and Y. Sakamaki. 1975. Uranium mineralization by ground water in sedimentary rocks, Japan, *Econ. Geol.* 70, 628-646.

Erikson, R. L., C. J. Hostetler, and M. L. Kemner. 1990. *Mobilization and Transport of Uranium at Uranium Mill Tailings Disposal Sites.* Pacific Northwest Laboratory, NUREG/CR-5169 and PNL-7154.

Gottardi, G. and E. Galli. 1985. *Natural Zeolites* Springer-Verlag, New York, 409 p.

Grover, D. A. and D. Freyberg. 1987. *User's Guide to TRANQL: A Ground-Water Mass Transport and Equilibrium Chemistry Model for Multicomponent Systems.* Letter Report to the Nuclear Regulatory Commission, Stanford Univ.

Hayes, K. F. and J. O. Leckie. 1986. Mechanism of lead ion adsorption at the goethite-water interface, In: Davis, J. A. and Hayes, K. F. (eds.), *Geochemical Processes at Mineral Surfaces.* ACS Symposium Series, v. 323, American Chemical Society, Washington, D.C., 114-141.

Honeyman, B. E. 1984. Cation and anion adsorption at the oxide/solution interface in systems containing binary mixtures of adsorbents: an investigation of the concept

of additivity, Ph.D. Dissertation, Civil Engineering Department, Stanford University, Stanford, CA, 383 p.

Honeyman, B. D. and J. O. Leckie. 1986. Macroscopic partitioning coefficients for metal ion adsorption, In: Davis, J. A. and Hayes, K. F. (eds.). *Geochemical Processes at Mineral Surfaces*. ACS Symposium Series, v. 323, American Chemical Society, Washington, D.C., 162-190.

Hostetler, C. J. and R. L. Erikson. 1989. *FASTCHEM™ Package, Vol. 5: User's Guide to the EICM Coupled Geohydrochemical Transport Code.* Electric Power Research Institute, EPRI-EA-5870-CCM, V5.

Hostetler, C. J., R. L. Erikson, J. S. Fruchter, and C. T. Kincaid. 1989. *FASTCHEM™ Package, Vol. 1: Overview and Application to a Chemical Transport Problem.* Electric Power Research Institute, EPRI-EA-5870, V1.

Hsi, C. D. 1981. Sorption of uranium (VI) by iron oxides, Ph.D. Dissertation, Colorado School of Mines, Golden, Colorado, 154 p.

Hsi, C.- K. D. and D. Langmuir. 1985. Adsorption of uranyl onto ferric oxyhydroxides: Application of the surface complexation site-binding model, *Geochim. Cosmochim. Acta*. 49, 1931-1941.

Ishihara, Y, M. Hitoshi, and A. Kenichi. 1988. Adsorption of uranium on zeolites. *Research Report of Laboratory of Nuclear Science Tohoku Univ.* 21: 71-77.

Katayama, N., K. Kubo, and S. Hirono. 1974. Genesis of uranium deposits of the Tono Mine, Japan, IAEA-SM-183/11.

Kelmers, A. D., R. E. Meyer, J. G. Blencoe, and G. K. Jacobs. 1987. Radionuclide sorption methodologies for performance assessment of high-level nuclear waste repositories: A perspective gained from an NRC workshop. *Nuclear Safety*. 28, 515-522.

Kent, D. B., V. S. Tripathi, N. B. Ball, J. O. Leckie, and M. D. Siegel. 1988. *Surface-Complexation Modeling of Radionuclide Adsorption in Subsurface Environments*. NUREG/CR-4807, U.S. Nuclear Regulatory Commission, Washington, D.C.

Kerrisk, J. F. 1987. *Groundwater Chemistry at Yucca Mountain, Nevada and Vicinity*. LANL LA-10929, Los Alamos National Laboratory, Los Alamos, New Mexico.

Kincaid, C. T. 1988. *FASTCHEM™ Package, Vol. 3: User's Guide to the ETUBE Pathline and Streamtube Database Code.* Electric Power Research Institute, EPRI-EA-5870-CCM, V3.

Kincaid, C. T., J. R. Morrey, and J. E. Rogers. 1984. *Geohydrochemical Models for Solute Migration, Vol. 1: Process Description and Computer Code Selection.* Electric Power Research Institute, EPRI-EA-3417.

Kirkner, D. J. and H. Reeves. 1988. Multicomponent mass transport with homogeneous and heterogeneous chemical reactions: Effect of the chemistry on the choice of numerical algorithm. 1. Theory. *Water Resourc. Res. 24:* 1719-1729.

Krupka, K. M., R. L. Erikson, S. V. Mattigod, J. A. Schramke, C. E. Cowan, L. E. Eary, J. R. Morrey, R. L. Schmidt, and J. M. Zachara. 1988. *Thermochemical Data Used by the FASTCHEM™ Package.* Electric Power Research Institute, EPRI-EA-5872.

Langmuir, D. 1978. Uranium solution-mineral equilibria at low temperatures with application to sedimentary ore deposits. *Geochim. Cosmochim. Acta.* 42, 547-569.

Lemire, R. J. and P. R. Tremaine. 1980. Uranium and plutonium equilibria in aqueous solutions to 200°C. *J. Chem. Eng. Data.* 25, 361-370.

Liu, C. W. and T. N. Narasimhan. 1989a. Redox-controlled multiple-species reactive chemical transport. 1. Model development. *Water Resourc. Res. 25:* 869-882.

Liu, C. W. and T. N. Narasimhan. 1989b. Redox-controlled multiple-species reactive chemical transport. 2. Verification and application. *Water Resourc. Res. 25:* 883-910.

Mangold, T . C. and C. Tsang. 1991. A summary of subsurface hydrological and hydrochemical models. *Rev. Geophys. 29:* 51-79.

Maya, L. 1982. Sorbed uranium (VI) species on hydrous titania zirconia and silica gel. *Radiochim. Acta.* 31, 147-151.

Meijer, A. 1990. Radionuclide sorption data base - experiments and integration of relevant sorption models. In: Radionuclide Adsorption Workshop, Sept. 11-12, Los Alamos, NM.

Miller, C. W. and L. V. Benson. 1983. Simulation of solute transport in a chemically reactive heterogeneous system: Model development and application. *Water Resourc. Res. 19:* 381-391.

Morrey, J. R. and C. J. Hostetler. 1985. Coupled geochemical and solute transport code development, G. K. Jacobs and S. K. Whatley (eds.). *Proceedings of the Conference on the Application of Geochemical Models to High-Level Nuclear*

Waste Repository Assessment, Oak Ridge Tennessee, October 2-5, 1984. NUREG/CP-0062 and ORNL/TM-9585: 90-92.

Morrey, J. R., C. R. Kincaid, and C. J. Hostetler. 1986. *Geohydrochemical Models for Solute Migration, Vol. 3: Evaluation of Selected Computer Codes.* Electric Power Research Institute, EPRI-EA-3417.

Noorishad, J. N., C. L. Carnahan, and L. V. Benson. 1987. *A Report on the Development of the Non-Equilibrium Reactive Transport Code CHMTRNS.* Lawrence Berkeley Laboratory, LBL-22361.

Olague, N. E., D. E. Longsine, J. E. Campbell, and C. D. Leigh. 1991. *User's Manual for the NEFTRAN II Computer Code.* Sandia National Laboratory, NUREG/CR-5618 and SAND90-2089.

Paquette, J. and R. J. Lemire. 1981. A description of the chemistry of aqueous solutions of uranium and plutonium to 200°C using potential-pH diagrams. *Nuclear Sci. Eng.* 79, 26-48.

Payne, T. E. and T. D. Waite. 1989. Modelling of radionuclide sorption processes in the weathered zone in the vicinity of the Koongara ore body, In: Duerden, P. (ed.), *Alligator Rivers Analog Project Progress Report Sept. 1 - Nov. 30, 1989.* Australian Nuclear Science and Technology Organization.

Pinder, G. F. 1976. *Galerkin Finite Element Models for Aquifer Simulation.* Unpub. report, Princeton Univ.

Rancon, D. 1973. The behavior of underground environments of uranium and thorium discharged by the nuclear industry, In: *Environmental Behavior of Radionuclides Released in the Nuclear Industry.* IAEA-SM-172/55, International Atomic Energy Commission, Vienna, Austria, 333-346.

Reeves, H. and D. J. Kirkner. 1988. Multicomponent mass transport with homogeneous and heterogeneous chemical reactions: Effect of the chemistry on the choice of numerical algorithm. 2. Numerical results. *Water Resourc. Res. 24:* 1730-1739.

Rimstidt, J. D. and H. L. Barnes. 1980. The kinetics of silica-water reactions. *Geochim. Cosmochim. Acta 44*: 1683-1699.

Rubin, J. and R. V. James. 1973. Dispersion-affected transport of reacting solutes in saturated porous media: Galerkin method applied to equilibrium-controlled exchange in unidirectional steady water flow. *Water Resourc. Res. 9:* 1332-1356.

Schmidt-Collerus, J. J. 1967. Research in uranium geochemistry: Investigation of the relationship between organic matter and uranium deposits - I. Denver Research Inst. (USAEC Contract No. AT(05-1)-933).

Siegel, M. D. (ed.) 1989. Progress in Development of a Methodology for Geochemical Sensitivity Analysis for Performance Assessment. Volume 2. Speciation, Sorption, and Transport in Fractured Media, NUREG/CR5085 V.2.

Siegel, M. D., J. O. Leckie, S. W. Park, S. L. Phillips, and T. Sewards. 1990. *Studies of Radionuclide Sorption by Clays in the Culebra Dolomite at the Waste Isolation Pilot Plant Site, Southeastern New Mexico.* SAND89-2387, Sandia National Laboratories, Albuquerque, NM.

Sposito, G. 1984. *The Surface Chemistry of Soils.* Oxford Univ. Press, New York.

Starik, I. Ye., F. Ye. Starik, and A. N. Apollonova. 1958. Adsorption of traces of uranium on iron hydroxide and its desorption by the carbonate method. *Zh. Neorgan. Khimii* 3, 1.

Szalay, A. 1964. Cation exchange properties of humic acids and their importance in the geochemical enrichment of UO_2^+ and other cations. *Geochim. Cosmochim. Acta.* 28, 1605-1614.

Travis, B. J. 1984. *TRACR3D: A Model of Flow and Transport in Porous/Fractured Media.* Los Alamos National Laboratory, LA-9667-MS.

Tripathi, V. S. 1984. Uranium transport modeling: geochemical data and submodels, Ph.D. Dissertation, Applied Earth Sciences Department, Stanford University, Stanford, CA, 297 p.

Tsunashima, A., G. W. Brindley, and M. Bastovanov. 1981. Adsorption of uranium from solutions by montmorillonite; compositions and properties of uranyl montmorillonites. *Clays and Clay Minerals.* 29, 10-16.

Valocchi, A. J., R. L. Street, and P. V. Roberts. 1981. Transport of ion-exchanging solutes in groundwater: Chromatographic theory and field simulation. *Water Resourc. Res. 17:* 1517-1527.

Vochten, R. F. C., L. van Haverbeke, and F. Goovaerts. 1990. External surface adsorption of uranyl-hydroxo complexes on zeolite particles in relation to the double-layer potential. *J. Chem. Soc. Farad. Trans.* 86, 4095-4099.

Wagman, D. D., W. H. Evans, V. B. Parker, R. H. Shumm, I. Halow, S. M. Bailey, K. L. Churney, and R. L. Nuttall. 1982. *The NBS Tables of Chemical Thermodynamic Properties. Selected Values for Inorganic and C1 and C2 Organic Substances in SI Units. Vol II Supplement.* American Chemical Society.

Walsh, M. P., L. W. Lake, and R. S. Schechter. 1982. A description of chemical precipitation mechanisms and their role information damage during stimulation by hydrofluoric acid. *J. Pet. Technol. 34:* 2097-2112.

Westall, J. 1979. *MICROQL: I. A Chemical Equilibrium Program in BASIC.* EAWAG, Swiss Federal Institute of Technology.

Yasunaga, T. and T. Ikeda. 1986. Adsorption-desorption kinetics at the metal-oxide-solution interface studied by relaxation methods, In: Davis, J. A. and Hayes, K. F. (eds.). *Geochemical Processes at Mineral Surfaces.* ACS Symposium Series, v. 323, American Chemical Society, Washington, D.C., 230-253.

Yeh, G. T. 1985. Comparison of successive iteration and direct methods to solve finite element equations of aquifer contaminant transport. *Water Resourc. Res. 21:* 272-280.

Yeh, G.T. and V. S. Tripathi. 1989. A critical evaluation of recent developments in hydrogeochemical transport models of reactive multichemical components. *Water Resourc. Res. 25:* 93-108.